Rechargeable Aluminum Batteries:

Critical evaluation of the influence of current collector, binder and anode material components

Zur Erlangung des akademischen Grades eines

DOKTORS DER NATURWISSENSCHAFTEN

(Dr. rer. nat.)

von der KIT-Fakultät für Chemie und Biowissenschaften des Karlsruher Instituts für Technologie (KIT)

genehmigte

DISSERTATION

von

M. Sc. Eugen Zemlyanushin

aus

Zelinograd, Kasachstan

Referent: Prof. Dr. rer. nat. Helmut Ehrenberg

Korreferent: Prof. Dr. rer. nat. Sonia Dsoke

Tag der mündlichen Prüfung: 09.05.2025

Selbstständigkeitserklärung

Hiermit versichere ich, dass ich die vorliegende Arbeit selbstständig verfasst habe, dass ich keine anderen als die angegebenen Quellen und Hilfsmittel benutzt habe, dass ich die wörtlich oder inhaltlich übernommenen Stellen als solche gekennzeichnet habe und, dass ich die Satzung des KIT zur Sicherung guter wissenschaftlicher Praxis in der jeweils gültigen Fassung beachtet habe.

Karlsruhe, den 25.03.2025	
Ort, Datum	Eugen Zemlyanushin

Acknowledgement

My journey at the Institute for Applied Materials-Energy Storage Systems (IAM-ESS) started as a bachelor's student on the 15th of April 2019. In these nearly six years I was allowed to increase my knowledge of lithium, sodium and aluminum batteries. Now, this long and hard trip is ending, but I wouldn`t have reached this final destination without so many support of dozens of people. Some of them deserve to be mentioned explicitly in my thesis.

First of all, I would like to thank my doctoral thesis supervisor, Prof. Dr. Helmut Ehrenberg, who helped me to improve my work through his comments, corrections and evaluations. But I think his greatest contribution was to calm me down in critical situations, otherwise, I would have gotten into a lot and big troubles.

From the very first day, Prof. Dr. Sonia Dsoke supported me with my work as a student assistant, during my advanced internship, which resulted in my very first publication. Sonia's greatest impact on my development as a scientist was to make me feel self-confident regarding my research and the obtained results. My gratitude for her contribution can be hardly expressed in words, because it will remain forever.

どうもありがとうございます Prof. Dr. Tetsuya Tsuda for the amazing time in Japan and excellent scientific support. At this point, I would like to express my gratitude to your students Rina Miyajima (宮島 里奈), Yudai Kojima (児島 雄大) and Yichen Fu, too. They helped me in case of technical issues and language barriers, which made my stay so much easier. I hope to see you all again as soon as possible to demonstrate how great I can handle your wonderful farewell present.

Огромное спасибо Dr. Angelina Sarapulova who always had an idea of how to solve any kind of problem. Moreover, there is barely any device she is not able to operate or evaluate their data. That`s just impressive and I am glad to have had the opportunity to work with such a strong and smart female scientist.

Merci beaucoup Dipl.-Ing. Vanessa Trouillet and Dr. Christian Njel for teaching and supporting me by measuring, plotting and evaluating XPS data.

Vielen Dank Dr. Kristina Pfeifer and Dr. Björn Schwarz for all your suggestions and advices during the last years. It was always a lot of fun to grab a drink or just to have a discussion with you.

谢谢 Dr. Jiali Peng, Dr. Chengping Li and Prof. Dr. Qiang Fu for a great time and for teaching me very important words and sentences in Chinese.

I would like to thank Dipl.-Geol. Julian Hansen and his wife Dr. Anna-Lena Hansen. Julian was able to solve every technical problem and it was an honour to help him do this or just build random stuff for the lab.

I sincerely appreciate the work of my students, Annika Lykka Müller and Kevin Xia. Both of them did a great job and helped me a lot with their effort.

Moreover, I want to mention Prof. Dr. Noha Sabi, Dr. Rafael Córdoba Rojano, Dr. Philipp Neidinger, Dr. Patrick Treffehn, Dr. Marina Bauer, Dr. Valeriu Mereacre, Liuda Mereacre, Heinz-Robert Goebel, Luis Martin Sanchez Neudeck and Almut Krise for their contribution to finalize my Ph.D. thesis.

Dr. Gabriele Glasser-Wuttke, Rolf Huber, Peter Gatzweiler and Norbert Sättele built the foundation for my academic career. Without their influence, I would never have studied chemistry.

Furthermore, I would like to thank my family. Without their financial and mental support, I would have given up at a very early stage. Therefore, thank you Viktor, Elena, Viktoria, Rafaelo, Leonardo and Carolina.

In the end, I want to highlight Dr. Xinyue Li's influence and contribution. I had the best time of my life with this incredible person and she is why I finished this thesis.

Abbreviations

°C	Degree Celsius
α	Alpha
β	Beta
γ	Gamma
λ	Lambda
Å	Angstrom
AA	Acetic acid
AC	Amorphous carbon
AF	Aluminum fluoride
ACF	Aluminum chlorofluoride
Al-C	Aluminum-Graphite
AlGa	Aluminum-Gallium
Ar/Ar^+	Argon/ionized argon
BE	Binding energy
BIBSC	Broad ion beam slope cutting
CB	Carbon Black
CC	Current collector
CE	Coulombic efficiency or counter electrode
CF	Carbon fiber
COF	Covalent-organic framework
CP	Carbon paper
CV	Cyclic voltammetry
DESs	Deep eutectic solvents

DHC	Dehydrochlorination
DHF	Dehydrofluorination
e^-	Electron
ECHA	European chemicals agency
EDS/EDX	Energy-dispersive X-ray spectroscopy
et al.	*Et alli* / *et aliae* / *et alia*
EMImCl	1-Ethyl-3-methylimidazolium chloride
Eq.	Equation
EXAFS	Extended X-ray absorption fine structure
Fig.	Figure
FT-IR	Fourier-transform infrared spectroscopy
GC	Glassy carbon
GCPL	Galvanostatic cycling with potential limitation
GF	Glass fiber
GICs	Graphite intercalation compounds
GO	Graphene oxide
IA	Inconel alloy
ICP-OES	Inductively coupled plasma optical emission spectroscopy
IL	Ionic liquid
ITO	Indium tin oxide
LIBs	Lithium-Ion Batteries
LSV	Linear sweep voltammetry
MIBs	Metal-Ion Batteries
MOF	Metal-organic framework

Na-Alg	Sodium-Alginate
NEXAFS	Near edge X-ray absorption fine structure
NG	Natural graphite
NMI	*N*-Methyl imidazole
NMP	*N*-Methyl-2-pyrrolidon
NMR	Nuclear magnetic resonance
OCV	Open circuit voltage
PFAS	Per- and polyfluoroalkyl substances
PG	Pyrolytic graphite
PI	Polyimide
PVdC	Polyvinylidene chloride
PVdF	Polyvinylidene fluoride
PS	Polysulfone
PSE	Polystyrene
PTFE	Polytetrafluoroethylene
PVP	Polyvinylpyrrolidone
QSRE	Quasi stable reference electrode
R^+	Cations
RABs	Rechargeable Aluminum-Batteries
RE	Reference electrode
RGOCPD	Reduced graphene oxide dried under supercritical conditions
RT	Room temperature
RTILs	Room-temperature ionic liquids
SEI	Solid-electrolyte interphase

SEM	Scanning electron microscopy
SHE	Standard hydrogen electrode
ss	Steady-state or solid solution
SS	Stainless steel
SWCNTs	Single-walled carbon nanotubes
TiN@Cu	Magnetron sputtered titanium nitride on copper foil
TiN@SS	Magnetron sputtered titanium nitride on stainless steel foil
UV-VIS	Ultraviolet-visible spectroscopy
XPS	X-ray photoelectron spectroscopy
XRD	X-ray diffraction

Figures

Tables

Appendix: Figures

Appendix: Tables

Abstract

The development of Rechareagble Aluminum-Batteries (RABs) is of great interest due to the low cost of highly abundant aluminum (Al) resources and increased safety compared to Lithium-Ion Batteries (LIBs). However, the need for a Lewis acidic ionic liquid (IL) electrolyte based on aluminum chloride ($AlCl_3$) and 1-ethyl-3-methylimidazolium chloride (EMImCl) is required to obtain reversible Al electroplating and electrostripping. Formed tetrachloroaluminate ($AlCl_4^-$) and heptachlorodialuminate ($Al_2Cl_7^-$) anions cause corrosion on metallic cell parts and the degradation and side-reactions with organic compounds. Such reactions can have a huge impact on the sensitive electrochemical process. So far, not much effort has been made to investigate and evaluate the influence of parasitic side-reactions.

This thesis critically focuses, among other things, on the impact and influence of the reactions of the $AlCl_3$:EMImCl IL electrolyte, in the molar ratio 1.5:1, with a molybdenum (Mo) current collector (CC) (**Chapter 4**). Molybdenum is typically considered stable with negligible redox activity in $AlCl_3$:EMImCl electrolytes. However, if Mo-foil or powder is immersed in the initially colourless/yellowish IL, the electrolyte turns red, indicating Mo dissolution. Magnetometry confirms the presence of Mo species with localized unpaired electrons in the reacted red liquid, not found in pure metallic Mo. Ultraviolet-visible (UV-VIS) spectroscopy reveals Mo^{3+} and Mo^{4+} species formation. X-ray photoelectron spectroscopy (XPS) indicates three oxidation states of Mo^{x+} (x=4,5,6) on the Al negative electrode. With Mo's instability, cyclic voltammetry (CV) and galvanostatic cycling with potential limitation (GCPL) show increasing redox activity over cycles with a discharge capacity of ~136 $mAh{\cdot}g^{-1}$ at 20 $mA{\cdot}g^{-1}$ in the potential window of 0.3-2.2 V *vs.* Al after 100 cycles. In addition, a possible reaction mechanism between the Mo CC and IL electrolyte is postulated. All obtained results conclude that every Mo source should be avoided for further investigations of RABs.

Commonly used polyvinylidene fluoride (PVdF) binder material is reported to react in contact with Lewis acidic $AlCl_3$:EMImCl ionic liquid electrolytes. So far, it is not mentioned in the literature what kind of product PVdF forms, how the ionic liquid electrolyte changes and the implication of such reactions on electrochemical performance is missing. In addition, with potential European Chemical Agency (ECHA) restrictions on per- and polyfluoroalkyl substances (PFAS) by 2025, polyvinylidene chloride (PVdC) is being explored as an alternative binder. **Chapter 5** deals with the dehydrofluorination (DHF) and dehydrochlorination (DHC) of PVdF and PVdC binder materials, in contact with the $AlCl_3$:EMImCl (1.5:1) IL electrolyte. Both, PVdF and PVdC, transform into amorphous carbon (AC), which is confirmed by Raman

spectroscopy. The degradation mechanism of PVdF/PVdC for forming sp^2 carbon-carbon double bonds is explained to be similar to the Friedel Crafts alkylation and acylation. Moreover, the formation mechanism of AC and obtained sp carbon-carbon triple bonds (polyyne) is described. Furthermore, *via* ^{19}F-NMR (nuclear magnetic resonance) spectroscopy, it is shown that the reaction time between the soaked polymers and the ionic liquid has a significant influence on the newly formed aluminum chlorofluoride (ACF), like tetrafluoroaluminate (AlF_4^-), complexes. Electrochemical tests of Graphite-based electrodes at 20 $mA \cdot g^{-1}$ and a potential window of 0.3-2.2 V *vs.* Al indicate increasing specific capacity of PVdF (initially ~45 $mAh \cdot g^{-1}$ and ~70 $mAh \cdot g^{-1}$ after 80 cycles) compared to PVdC (initially ~45 $mAh \cdot g^{-1}$ and ~50 $mAh \cdot g^{-1}$ after 80 cycles) with a continuous number of cycles. Formed AC can prevent Graphite's disintegration and enhance the electrode's conductivity. Furthermore, besides the intercalating $AlCl_4^-$ species, newly formed AlF_4^- can run a co-intercalation and lead to increasing specific capacity. All described results confirm that the reaction between PVdF/PVdC and the IL electrolyte is beneficial for Graphite-based RABs.

The Al negative electrode suffers from the harsh IL electrolyte environment too. Long-term cycle tests result in the formation of cracks and pits followed by pulverization, dendrite growth and inactive Al. One attempt to overcome all these problems can be the formation of an Al-alloy with self-healing ability. Therefore, different molarities (0.1 M, 0.2 M, 0.3 M and 0.5 M) of gallium chloride ($GaCl_3$) have been added to the electrolyte to generate *in-situ* an Aluminum-Gallium (AlGa) alloy negative electrode (**Chapter 6**). Electrochemical measurements confirm the reversible alloying and dealloying of AlGa during charge/discharge, respectively. The newly formed Ga-rich surface leads to an initial surface-controlled Al nucleation, which turns into a diffusion-controlled process. GCPL measurements of Al-Graphite cells at 20 $mA \cdot g^{-1}$, in the potential window 0.3-2.2 V *vs.* Al, indicate a higher initial specific capacity of ~61 $mAh \cdot g^{-1}$ to ~73 $mAh \cdot g^{-1}$ with increasing $GaCl_3$ amount of 0.1 M - 0.5 M, respectively. Rate tests at 20, 50, 100, **200**, **500**, **1000**, 20 and 10 $mA \cdot g^{-1}$ show increased stability at **higher** current densities with $GaCl_3$ additive. Scanning electron microscopy (SEM) images show less surface damage with $GaCl_3$ additive electrolytes. Synchrotron X-ray diffraction (XRD) measurements indicate a decreased structural order of the Graphite during charging. This phenomenon seems to be influenced mostly by surface-controlled processes, that can improve the rate capability of the Ga-containing samples. The obtained results prove that the *in-situ* generated AlGa alloy surface of the negative electrode is more resistant to the harsh Lewis acidic environment.

Zusammenfassung

Die Entwicklung von wiederaufladbaren Aluminium-Batterien (RABs) ist von großem Interesse aufgrund der geringen Kosten der reichlich vorhandenen Aluminium (Al) Ressourcen und der erhöhten Sicherheit im Vergleich zu Lithium-Ionen-Batterien (LIBs). Allerdings ist eine Lewis saure ionische Flüssigkeit (IL) als Elektrolyt, bestehend aus Aluminiumchlorid ($AlCl_3$) und 1-Ethyl-3-methylimidazoliumchlorid (EMImCl) erforderlich um reversibles Abscheiden und Auflösen von Al zu erzielen. Gebildete Tetrachloroaluminat-($AlCl_4^-$) und Heptachlorodialuminat- ($Al_2Cl_7^-$) Anionen verursachen Korrosionen an metallischen Zellbauteilen sowie Degradierung und Nebenreaktionen mit organischen Verbindungen. Solche Reaktionen können einen großen Einfluss auf den empfindlichen elektrochemischen Prozess haben. Bisher wurden nur wenig unternommen, um den Einfluss parasitärer Nebenreaktionen zu untersuchen und zu bewerten.

Diese Dissertation ist unter anderem kritisch fokussiert auf die Auswirkungen und den Einfluss der Reaktionen des $AlCl_3$:EMImCl IL-Elektrolyten im molaren Verhältnis 1,5:1 mit dem Molybdän (Mo) Stromableiter (CC) (**Kapitel 4**). Molybdän wird als stabil mit vernachlässigbarer Redoxaktivität in $AlCl_3$:EMImCl-Elektrolyten angesehen. Wenn jedoch Mo-Folie oder Pulver in das anfangs farblose/gelbliche IL eingetaucht wird, färbt sich der Elektrolyt rot, was auf eine Mo Auflösung deutet. Magnetometrie bestätigt das Vorhandensein von Mo-Spezies mit lokalisierten ungepaarten Elektronen in der reagierten roten Flüssigkeit, die im reinen metallischen Mo nicht vorhanden sind. Spektroskopische Messungen im ultravioletten-sichtbaren (UV-VIS) Bereich zeigen die Bildung von Mo^{3+} und Mo^{4+} Kationen. Durch Röntgenphotoelektronenspektroskopie (XPS) konnten drei Oxidationszustände von Mo^{x+} (x=4,5,6) auf der Al negativen Elektrode ermittelt werden. Mit der Instabilität von Mo zeigen die Cyclovoltammetrie (CV) und das galvanostatische Zyklieren mit Potenzialbegrenzung (GCPL) eine mit steigender Zyklenzahl zunehmende Redoxaktivität mit einer Entladekapazität von ~136 $mAh \cdot g^{-1}$ bei 20 $mA \cdot g^{-1}$ im Potenzialfenster von 0,3-2,2 V *vs.* Al nach 100 Zyklen. Zudem ist ein möglicher Reaktionsmechanismus zwischen dem Mo CC und dem IL postuliert. Alle Ergebnisse lassen darauf schließen, dass jede Mo Quelle für weitere Untersuchungen von RABs vermieden werden sollte.

Das häufig verwendete Polyvinylidenfluorid (PVdF) Bindemittel reagiert Berichten zufolge im Kontakt mit Lewis sauren $AlCl_3$:EMImCl basierten ionischen Flüssigkeiten. Bisher wird in der Literatur nicht erwähnt, welches Produkt PVdF bildet, wie sich die ionische Flüssigkeit verändert und welche Auswirkungen solche Reaktionen auf die elektrochemische Leistung

haben. Angesichts möglicher Beschränkungen der Europäischen Chemikalienagentur (ECHA) für per- und polyfluorierte Alkylsubstanzen (PFAS) im Jahr 2025, wird Polyvinylidenchlorid (PVdC) als alternatives Bindemittel untersucht. **Kapitel 5** handelt von der Dehydrofluorierung (DHF) und Dehydrochlorierung (DHC) von PVdF und PVdC Bindematerialien im Kontakt mit dem $AlCl_3$:EMImCl (1.5:1) IL-Elektrolyten. PVdF und PVdC wandeln sich beide in amorphen Kohlenstoff (AC) um, wie es durch Raman Spektroskopie bestätigt wurde. Der Mechanismus von PVdF/PVdC zur Bildung von sp^2 Kohlenstoff-Kohlenstoff-Doppelbindungen wird ähnlich der Friedel Crafts Alkylierung und Acylierung erklärt. Zudem wird der Bildungsmechanismus von AC und die erhaltenen sp Kohlenstoff-Kohlenstoff-Dreifachbindungen (Polyyne) beschrieben. Weiterhin wird mittels ^{19}F-NMR (Kernspinresonanzspektroskopie) gezeigt, dass die Reaktionszeit zwischen den Polymeren und der IL einen signifikanten Einfluss auf die neu gebildeten Aluminiumchlorfluorid (ACF)-Komplexe, wie Tetrafluoroaluminat (AlF_4^-), hat. Elektrochemische Tests von Graphit-basierten Elektroden bei 20 $mA{\cdot}g^{-1}$ und einem Potentialfenster von 0,3-2,2 V *vs.* Al zeigen eine zunehmende spezifische Kapazität von PVdF (anfangs ~45 $mAh{\cdot}g^{-1}$ und ~70 $mAh{\cdot}g^{-1}$ nach 80 Zyklen) im Vergleich zu PVdC (anfangs ~45 $mAh{\cdot}g^{-1}$ und ~50 $mAh{\cdot}g^{-1}$ nach 80 Zyklen) mit steigender Zyklenzahl. Gebildeter AC kann die Zersetzung von Graphit verhindern und die Leitfähigkeit der Elektrode verbessern. Zusätzlich können neben der interkalierenden $AlCl_4^-$ Spezies neu gebildetes AlF_4^- eine Ko-Interkalation durchführen und zu einer steigenden spezifischen Kapazität führen. Erhaltene Ergebnisse bestätigen, dass die Reaktion zwischen PVdF/PVdC und der IL vorteilhaft für Graphit-basierte RABs ist.

Die negative Al Elektrode leidet auch unter der harschen IL Umgebung. Langzeittests führen zur Bildung von Rissen und Löchern, gefolgt von Pulverisierung, Dendritenwachstum und inaktiven Al. Ein Ansatz um alle genannten Probleme zu überwinden ist die Bildung einer Aluminium-Gallium (AlGa) Legierung mit der Fähigkeit sich selbst du regenerieren. Deshalb wurden verschiedene Molaritäten (0,1 M, 0,2 M, 0,3 M und 0,5 M) von Galliumchlorid ($GaCl_3$) der IL zugesetzt, um *in-situ* eine AlGa negative Elektrode zu erzeugen (**Kapitel 6**). Elektrochemische Messungen bestätigen das reversible Legieren/Entlegieren von AlGa während des Ladens/Entladens. Die neu gebildete Ga-reiche Oberfläche führt zu einer anfänglichen oberflächenkontrollierten Al Keimbildung, die sich in einen diffusionskontrollierten Prozess umwandelt. GCPL-Messungen von Al-Graphit-Zellen bei 20 $mA{\cdot}g^{-1}$ im Potentialfenster von 0,3-2,2 V *vs.* Al zeigen eine höhere anfängliche spezifische Kapazität von ~61 $mAh{\cdot}g^{-1}$ bis ~73 $mAh{\cdot}g^{-1}$ mit zunehmender $GaCl_3$-Menge von 0,1 M - 0,5 M. Ratentests bei 20, 50, 100, **200**, **500**, **1000**, 20 und 10 $mA{\cdot}g^{-1}$ zeigen eine erhöhte Stabilität bei

höheren Stromdichten mit $GaCl_3$ Additiv. Rasterelektronenmikroskopie (SEM) Aufnahmen zeigen weniger Oberflächenschäden mit $GaCl_3$-Zusatz. Synchrotron Röntgenbeugungsmessungen (XRD) weisen auf eine verringerte strukturelle Ordnung des Graphits während des Ladens hin. Dieses Phänomen scheint hauptsächlich durch oberflächenkontrollierte Prozesse beeinflusst zu werden, die die Ratenfähigkeit der Ga-haltigen Proben verbessern können. Die erhaltenen Ergebnisse bestätigen, dass die *in-situ* erzeugte AlGa Legierungsoberfläche der negativen Elektrode widerstandsfähiger gegen die harsche Lewis saure Umgebung ist.

Content

1. Introduction

1.1 Motivation and Aim of this Thesis

The heavy reliance on fossil fuels has increased the effects of global climate change because of the anthropogenic release of carbon dioxide (CO_2) [1]. To combat these climate challenges and reduce their impact on mankind, the use of renewable energy sources, such as geothermal- [2], water- [3], wind- [4] and solar energy [5] become a main focus. However, to use and handle these green energy sources requires the development of innovative and alternative energy storage systems. Rechargeable batteries offer a practical option for storing electrical power. Currently, Lithium-Ion Batteries (LIBs) are the most powerful and effective rechargeable batteries. LIBs are crucial in everyone's daily lives, powering everything from portable electronics to electric vehicles (**Fig. 1 A**). The dependence on electric devices continues to increase, therefore, the demand for alternative and more advanced energy storage is enormous. Due to the huge demand, there is the risk of raw materials supply and the need for alternative battery chemistries with more available materials is necessary to be developed. Meanwhile, there is a tendency towards the investigation of multivalent systems used as negative electrode material like aluminum (Al), which can provide three electrons per ion exchanged (**Fig. 1 B**).

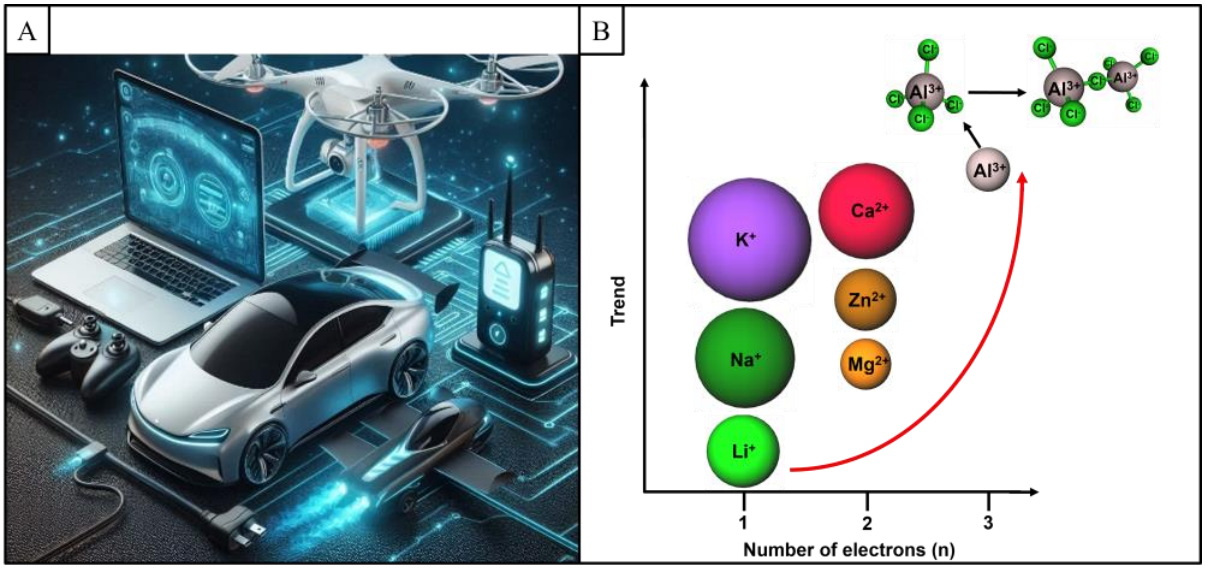

Figure 1 (A) Typical daily life objects operated with Lithium-Ion Batteries (LIBs). (B) Research trend towards multivalent ion batteries. DeepAI has been used to generate Figure 1 A.

Aluminum is the most abundant metal and after oxygen (O) and silicon (Si) the 3rd most abundant element in the earth's crust [6]. Compared to monovalent lithium (Li), sodium (Na), potassium (K) and divalent magnesium (Mg), zinc (Zn) and calcium (Ca) counterparts, Al has

the highest theoretical volumetric capacity of 8046 $mAh \cdot cm^{-3}$, which is about four times more than Li with 2062 $mAh \cdot cm^{-3}$ [7]. Although the theoretical gravimetric capacity of 2981 $mAh \cdot g^{-1}$ is lower than that of Li (3861 $mAh \cdot g^{-1}$) [8], it is still superior to other metals. A direct comparison regarding the gravimetric- and volumetric capacity, standard hydrogen electrode potential (V *vs.* SHE) and cation radius of all metals is given in **Table 1**.

Table 1 Comparison between aluminum (Al), calcium (Ca), zinc (Zn), magnesium (Mg), potassium (K), sodium (Na) and lithium (Li) regarding their theoretical gravimetric- and volumetric capacity, standard hydrogen potential and cation radius.

Element	**Gravimetric capacity ($mAh \cdot g^{-1}$)**	**Volumetric capacity ($mAh \cdot cm^{-3}$)**	**Standard Hydrogen Potential (V *vs.* SHE)**	**Cation radius (Å)**
Al [7–9]	2981	8046	-1.66	0.54
Ca [8,9]	1340	2061	-2.87	1.00
Zn [8,9]	820	5857	-0.76	0.74
Mg [8,9]	2205	3868	-2.37	0.72
K [8,9]	685	609	-2.93	1.38
Na [8,9]	1166	1050	-2.71	1.02
Li [7–9]	3861	2062	-3.04	0.76

Due to these exceptional properties, the large-scale development of Rechargeable Aluminum-Batteries (RABs) combined with appropriate positive electrode materials and electrolytes, offers the potential for high energy density storage systems. However, RABs are operated with highly corrosive Lewis acidic ionic liquid (IL) electrolytes made of aluminum chloride ($AlCl_3$) and 1-ethyl-3-methylimidazolium chloride (EMImCl), which react with metallic parts and lead to the degradation of organic compounds inside the cells. So far, such galvanic corrosion, degradation and side-reactions are not well-investigated and their influence on the electrochemical process is unknown. For the development of RABs, it is urgent to understand the cell's insides to avoid or control material degradations, which can have a high impact on the sensitive electrochemical process. For instance, newly formed redox active species can lead to additional specific capacities, not related to the studied positive electrode material or due to the generation of dendrites and inactive Al, the cell lifetime can be strongly decreased [10].

In this doctoral thesis, the following three challenging components used in non-aqueous $AlCl_3$-based RABs are examined:

The IL electrolyte forms the following two complexes; Tetrachloroaluminate ($AlCl_4^-$) as the Lewis base, which is the intercalating species into the positive electrode host material and heptachlorodialuminate ($Al_2Cl_7^-$) as the corresponding Lewis acidic species. The latter is

responsible for corroding the metallic cell parts like the cell body and the current collector (CC). Meanwhile, it is well known that metals like stainless steel (SS) [11] or aluminum [12] cannot be used as cell parts or CC, respectively, due to their low anodic stability [13]. Molybdenum (Mo) is considered to be a stable metal in contact with Lewis acidic IL electrolytes. However, in the literature, controversial and contradictory results are reported about the stability of Mo in comparison with other metallic CC`s. Furthermore, investigations on the Mo stability were made with little effort. One goal of this thesis (**Chapter 4**) is to understand **how Mo interacts with the IL electrolyte** and thus to get an idea of **how redox reactions take place in the electrochemical process**. In addition, attempts are made to **test a non-metallic titanium nitride (TiN) CC sputtered on SS and copper (Cu) substrate** (called TiN@SS and TiN@Cu), to **avoid expensive metals with high intrinsic densities** as CC material in RABs.

Moreover, most of the published research articles dealing with RABs, describe the use of polyvinylidene fluoride (PVdF) as binder material. However, it is well known that pure white PVdF powder turns black in contact with the IL electrolyte [14], which is an indication of possible side-reactions taking place. Nevertheless, it is still used without knowing the influence on cell performance. To date, no attempts have been made to figure out what kind of reactions occur between PVdF and the IL electrolyte. One part of this doctoral thesis is to understand **how the binder and the electrolyte react** with each other, **which products are formed** and **how this instability influences the stability and electrochemical charge/discharge processes** of Aluminum-Graphite (Al-C)-based RABs. Additionally, **polyvinylidene chloride (PVdC) is investigated as an alternative binder material** because the European Chemicals Agency (ECHA) potentially restricts the use of per- and polyfluoroalkyl-based chemicals (PFAS) by 2025 [15]. Moreover, having a chloride- instead of fluoride-based binder would theoretically lead to a **non-mix of halides in the electrolyte**. A detailed introduction, presentation and discussion of the achieved results are given in **Chapter 5**.

The main reasons for the use of Lewis acidic IL electrolytes are to obtain reversible electroplating and the removal of the naturally formed aluminum(III)-oxide (Al_2O_3) layer on the Al negative electrode surface. The Al_2O_3 film needs to be corroded to obtain an active Al, which requires a harsh IL electrolyte environment. However, without a protective film, the Al-foil suffers from dendrite formation, pitting corrosion, formation of inactive “dead” Al and pulverization [10,16]. **The presence of a second metal such as gallium (Ga) in an Aluminum-Gallium (AlGa) alloy, could enable the removal of the oxide layer and prevent pitting corrosion and lead to a stable negative electrode for RABs. Moreover, the initiation of Al**

growth could no longer be limited to defects on the Al surface. Instead, Al should grow over the amorphous boundaries everywhere, which reduces the possibility of dendrite growth and formation of inactive Al. This thesis aims to avoid all the mentioned problems by **developing and investigating a new kind of AlGa negative electrode**. To obtain an AlGa alloy, two different attempts are considered: **(I) By mixing metallic Al and metallic Ga (*ex-situ* method)** and **by adding different molarities of gallium chloride ($GaCl_3$) powder into the IL electrolyte (*in-situ* method).** The explicit reasons, desired effects, syntheses and obtained results of prepared AlGa alloys are described in **Chapter 6.**

The investigations of the Mo CC, PVdF/PVdC binder materials and the formation of a more resistant AlGa negative electrode in $AlCl_3$:EMImCl (1.5:1)-based ionic liquid electrolyte should help to get more insights into RABs, clarify controversial statements- and close current informational gaps in the literature. By this, a contribution to the further development of RABs is given.

2. Definitions, Challenges and Battery Insides

2.1 Introduction

This chapter gives a general introduction to the history, components and working principle of Rechargeable Aluminum-Batteries (RABs). A deeper insight into the function of the aluminum (Al) negative electrode, current collector (CC) and binder materials will be shown in **Chapter 4**, **Chapter 5** and **Chapter 6**, respectively. Furthermore, in **2.2 Foreword: Definitions** some nomenclatures of commonly used terms are defined to maintain their accuracy. In addition, in **2.3 Preface: Research challenges** some main issues of investigating and developing RABs are briefly mentioned.

2.2 Foreword: Definitions

First of all, it is important to distinguish between a "battery" and a "cell". The term "battery" is often used to refer to the basic electrochemical unit, which is an electrochemical cell. An electrochemical cell generates electrical energy through a chemical reaction known as a redox (reduction and oxidation) reaction. This reaction occurs in a system comprising an anode and a cathode, without being in direct contact and enveloped by an electrolyte. In contrast, a battery is a collection of electrochemical cells connected in either parallel or series configuration. Throughout this doctoral thesis, the term "battery" will refer specifically to a rechargeable electrochemical cell.

Secondly, the terms "cathode" and "anode" need to be defined. In electrochemical literature, the "cathode" is the electrode where the reduction reaction occurs, while on the "anode" the oxidation reaction takes place. However, this is only true during discharge. During charging, these reactions are reversed. Therefore, in this thesis, "cathode" and "anode" will always refer to the positive- and negative electrode, respectively, regardless of whether the cell is charging or discharging.

Thirdly, it is important to mention that an Aluminum-Graphite (Al-C) battery based on tetrachloroaluminate ($AlCl_4^-$) intercalation, is not a "rocking-chair" battery like Lithium-Ion Batteries (LIBs) (see **Chapter 2.5**) and should not be referred to as an Aluminum-Ion Battery (AIB).

2.3 Preface: Research Challenges

The biggest challenge working with RABs is the Lewis acidic aluminum(III)-chloride ($AlCl_3$):1-ethyl-3-methylimidazolium chloride (EMImCl) ionic liquid electrolyte. Chloroaluminate-based ionic liquids are extremely oxophilic thus forming adducts with C-O functionalities and reacting irreversibly with moisture and oxygen to form hydrochloric acid (HCl) and Al-oxochlorides like $AlOCl_2^-$ [17]. Since the reaction between $AlCl_3$ and EMImCl is exothermic, mixing both salts very slowly and under stirring is urgent [18]. Otherwise, thermal degradation can occur and change the molar ratio of the electrolyte. Furthermore, it is necessary to buy high-purity chemicals. $AlCl_3$ often contains iron(III)-chloride ($FeCl_3$) which can form tetrachloroferrate ($FeCl_4^-$) and run redox reactions inside the cell. A prepared ionic liquid electrolyte should always be colourless and not yellow/orange. If the electrolyte is yellow/orange, it indicates the presence of $FeCl_4^-$ [19] or side-products of other impurities like unreacted starting materials (*N*-Methyl imidazole; NMI) or residual solvents of $AlCl_3$ and EMImCl due to thermal decompositions [20]. Another electrolyte-related problem is the high Lewis acidity, which can corrode several kinds of metal, like stainless steel (SS) [11]. Usually, devices for running measurements (Raman, FT-IR, *etc*.) and sample holders, like coin cells for *operando* or *post-mortem* measurements are made of SS. Therefore, many measurements are difficult to handle to get results without external influence of side-reactions or even to get permission to use certain devices. The risk of damaging expensive machines is too high and the owner or provider prefers to reject proposals. Last but not least, the greatest issues of the current development of RABs are the many contradictions in the literature. Reported results on active materials, the influence of the aluminum(III)-oxide (Al_2O_3) layer, binder materials and metallic current collectors suffer from misinterpretations and make further research difficult. More research challenges have been redacted in a review paper with the title "**Navigating the Challenges of Rechargeable Aluminum Battery Research: Materials Instabilities, Technical Hurdles, and Future Directions"** [21]**.**

2.3.1 Aluminum negative electrode (Anode)

The primary negative electrode material in RABs is typically a simple Al-foil, where the reversible electrodeposition of $Al_2Cl_7^-$ occurs. The performance of the aluminum anode strongly depends on the metal's purity, microstructure, alloying elements and surface modifications [22]. In 2022, Wang *et al.* [23] studied the stability of the negative electrode in $AlCl_3$:EMImCl (1.5:1) ionic liquid electrolyte through galvanostatic cycling of a symmetric Al-Al cell. Their results showed a large initial overpotential, attributed to the presence of an

Al_2O_3-passivating layer. Initial exposure to the acidic ionic liquid partially removed this layer chemically and during cycling, the film was consistently removed, reducing the overpotential. Scanning electron microscopy (SEM) images of the Al surface revealed that it was initially smooth after one cycle, but after only 10 cycles, the surface appeared cracked with large pits, indicating the formation of inactive Al in combination with loss due to dissolution. More details about the Al negative electrode are given in **Chapter 6**, which are extracted from a **"Roadmap on multivalent batteries"** and **"Navigating the Challenges of Rechargeable Aluminum Battery Research: Material Instabilities, Technical Hurdles, and Future Directions**" publications with the contribution of E. Zemlyanushin [21,24].

2.3.2 Positive electrode (Cathode)

The primary concern for cathode materials in RABs is their chemical stability in chloroaluminate ionic liquid electrolytes. Unlike LIBs, where the cathodes' chemical stability in the electrolyte is not the major issue. The chemical stability of cathodes for RABs can be easily overlooked since many have already been studied in LIBs. However, due to their complex nature, chloroaluminate ILs differ significantly from LIB electrolytes. For instance, vanadium(V)-oxide (V_2O_5), a cathode material currently under extensive investigation for RABs, has been shown by Wen *et al.* [25] to react with both, Lewis acidic (molar ratio 2:1) and Lewis neutral (molar ratio 1:1) electrolytes, as demonstrated by the following reaction **Equation 1** and **2**:

$$\text{Lewis acidic: } V_2O_5 + 2Al_2Cl_7^- \rightarrow 2VOCl_3 + 2AlCl_4^- + Al_2O_3 \quad (1)$$

$$\text{Lewis neutral: } V_2O_5 + 2AlCl_4^- \rightarrow VO_2Cl + AlCl_3VO_3^- \quad (2)$$

These studies highlight the necessity of validating the chemical stability of cathode materials in chloroaluminate IL electrolytes before examining their electrochemical properties. To avoid such unwanted side-reactions, Graphite can be used as a host material in RABs. Graphite is widely used in electrochemical energy storage applications due to its layered structure, which allows for the insertion and removal of charged ionic species during battery charge and discharge. In RABs, $AlCl_4^-$ anions from the electrolyte intercalate into the Graphite interlayers. Most studies conclude that $AlCl_4^-$ intercalates as a tetrahedron or doubly-stacked tetrahedra,

rather than in a planar configuration [26–28]. In **Chapter 2.5**, a detailed working mechanism of Aluminum-Graphite (Al-C) batteries is demonstrated.

2.3.3 Binder

The binder is supposed to connect all electrode components, provide good contact with the current collector and should be inert against all the other cell components. A volume change may happen to the electrode during the charge/discharge process due to intercalation or phase changes. The binder must be resistant to mechanical stress to stabilize the structure of the active materials [29]. The binder supports the coherence between active material particles, conductive additives and the current collector and its inherent conductive properties, thus affecting the electrode conductivity. In the slurry preparation process, the binder solvents like *N*- Methyl- 2- pyrrolidone (NMP), dimethyl sulfoxide (DMSO), water (H_2O) or isopropyl alcohol (C_3H_7OH) must first wet the active material/conductive additive powder. A mechanical treatment (stirring/ultrasonicate) breaks apart aggregates and agglomerates of particles. The binder should possess good dispersing properties with the solvent to stabilize particles against accumulation and precipitation. While electrode binders do not directly contribute to the cell's capacity, they are crucial for the positive electrode's performance. Key requirements for an effective electrode binder include chemical- and electrochemical inertness towards the electrolyte to prevent side-reactions, mechanical robustness to maintain structural integrity during repeated cycling and strong adhesion to the current collector. In RABs, polyvinylidene fluoride (PVdF) is commonly used as an electrode binder due to its processability, solubility and (electro)chemical stability in non-aqueous solvents. However, some studies have reported that PVdF reacts with Lewis acidic chloroaluminate ionic liquid electrolytes, based on visual observations [14] and galvanostatic cycling tests [30–33]. In contrast, polymers such as polytetrafluoroethylene (PTFE), polysulfone (PS), polyimide (PI) and polystyrene (PSE) are (electro)chemically inert in $AlCl_3$-based electrolytes. More detailed information and research results are given in **Chapter 5**, which are extracted from the publication of Zemlyanushin *et al* [34].

2.3.4 Current collector (CC)

The current collector (CC) is usually a thin metallic foil, which carries the active material. It should provide high electronic conductivity and non-reactivity towards other cell components and low-cost, -weight and -intrinsic density [35–37]. For LIBs the current collectors are copper (Cu) (for the negative-) and Al (for the positive electrode). However, both metals cannot be used as CC due to their low anodic stability in Lewis acidic ionic liquid electrolytes. Therefore,

alternatives such as molybdenum (Mo), tungsten (W) and carbon paper (CP) are applied. Further information, observed results and discussions are listed in **Chapter 4**, which are extracted from the **"Roadmap on multivalent batteries"** publication with the contribution of E. Zemlyanushin [24] and the publication of Zemlyanushin *et al* [38].

2.3.5 Separator

The separator is a microporous membrane that physically separates the positive electrode and negative electrode to prevent short circuits while simultaneously allowing ions to pass between the electrodes. The most common separator for RABs is a glass fiber (GF) with different pore sizes. Celgard separator, used in LIBs [39], cannot be used since the diffusion of $AlCl_4^-$ and $Al_2Cl_7^-$ does not occur. Besides the porosity, the thickness of separators influences the battery performance. Thin separators have lower resistance and increase the energy- and power density of the battery while decreasing the possible use volume of the ionic liquid electrolyte. On the other hand, thicker (or several) separators provide a higher electrolyte volume, but the high resistance may negatively affect the flow of the active anion species.

2.3.6 Conductive carbon additive

The conductive additive is an electrode component that ensures good electric contact between active material particles to enhance the electronic flow [40]. Carbon black (CB) is a commonly used additive owing to its highly conductive and readily dispersible merits. Carbon black covers the surface of the active material particles in an exemplary network and thus provides a pathway for the flowing electrons [41].

2.3.7 Reference Electrode (RE) and Quasi Stable Reference Electrode (QSRE)

A reference electrode (RE) has a well-known potential value and is designed to achieve ideal non-polarizable behaviour, meaning its potential remains constant even with the passage of a small current [42]. The electrode and electrolyte solution potentials are equal, indicating thermodynamic equilibrium. Creating and stabilizing well-defined reference electrodes for $AlCl_3$-based RABs is challenging because their potential can differ due to changes of the surface condition, which may be affected by reactions with electrolytes, dissolution in the electrolyte, or polarization [43]. In **Chapter 6**, formed AlGa alloys are used as quasi stable reference electrode (QSRE). QSRE`s are assumed to maintain a stable potential during electrochemical measurements. Nevertheless, QSRE`s potential needs to be calibrated against a reliable internal reference electrode or redox system. For instance, ferrocene/ferrocenium (Fc^0/Fc^+) can be used

as an internal standard [44], however, a calibration is impossible due to the harsh Lewis acidic environment.

2.4 Electrolytes for Rechargeable Aluminum-Batteries (RABs)

2.4.1 Introduction

The electrolyte in an electrochemical cell provides pathways for ionic transport, completing the electrical circuit and playing a crucial role in controlling the overall chemical reactions within the battery. Currently, the limitations of available electrolytes hinder further improvements of RABs for real-world applications. Commonly used ionic liquid electrolytes are hygroscopic and highly corrosive [45], therefore, developing new electrolytes that meet performance, safety and sustainability demands is essential for future energy storage systems [46]. Non-aqueous electrolytes become a suitable candidate for application in secondary batteries because of their thermodynamic stability in a wider range of potentials and reversible electroplating/electrostripping ability compared to water-based electrolytes [47]. At this point, it is worth mentioning that all the further listed electrolytes are non-aqueous systems. The use of aqueous electrolyte systems is not discussed in this doctoral thesis.

2.4.2 Requirements for Electrolyte Design

In RABs, the electrolyte must support reversible Al electroplating and electrostripping during charge/discharge, respectively. Since aluminum electroplating occurs from aluminum-containing species ($Al_2Cl_7^-$) within the electrolyte, the volume of electrolyte used and the availability of electroactive species effectively limits the capacity [48]. Therefore, selecting a suitable electrolyte for RABs requires the consideration of the following factors:

(I) Wide electrochemical stability window: A wide potential window prevents the degradation and decomposition of the electrolyte, ensuring long-term cycling stability [49]. Moreover, if the electrolyte can reach a high potential, the range of suitable positive electrode materials increases too.

(II) Conductivity and viscosity: High ionic conductivity and low viscosity accelerate ion transport and influence the rate capability of RABs [50]. New electrolytes should have an ionic conductivity of around 10^{-2} $S \cdot cm^{-1}$ to be competitive with LIBs [51]. Interestingly, in the case of $AlCl_3$:BMImCl (1-butyl-3-methylimidazolium chloride) ionic liquid electrolyte, the conductivity decreases with the rising $AlCl_3$ molar ratio [52].

(III) Inertness against other cell components: Electrolytes should not react with any parts of the cell, including the cathode, anode, binder or cell housing. Moreover, electrolytes that can be safely handled in an ambient atmosphere are needed to simplify production and reduce costs for large-scale manufacturing.

2.4.3 Room-Temperature Ionic Liquids (RTILs)

Room-temperature ionic liquids (RTILs) are defined as organic salts made up of weakly coordinated complex ions that exist in the liquid state at room temperature (RT) [53,54]. Thermal stability, non-flammability, low volatility and negligible vapour pressures, make RTILs ideal liquids to be used as solvents [55,56], catalysts [55,56] and electrolytes [57]. Ionic liquid electrolytes for RABs are usually Lewis acidic melts made of aluminum chloride ($AlCl_3$) and organic halogen salts in the form R^+X^-. The common organic cations (R^+) are: Alkylammonium, alkylphosphonium, *N*-alkylpyridinium and *N*,*N*`-dialkylimidazolium (**Fig. 2 A-D**); while the counter anions are halogens (X^-) like chloride (Cl^-), bromide (Br^-), fluoride (F^-) or organic anions [55,58,59]. Nowadays, $AlCl_3$, 1-ethyl-3-methylimidazolium chloride (EMImCl) and 1-butyl-3-methylimidazolium chloride (BMImCl) dominate as IL components for RABs, due to higher specific capacities and relatively dense and crystalline Al deposition, like it is demonstrated by Tsuda *et al* [60].

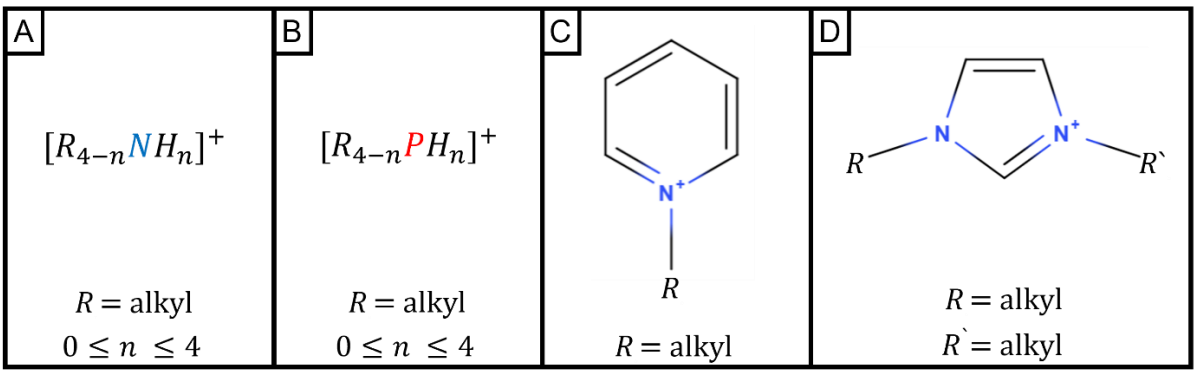

Figure 2 Common organic cations of IL electrolytes. (A) Alkylammonium, (B) alkylphosphonium, (C) *N*-alkylpyridinium and (D) *N*,*N*`-dialkylimidazolium.

The Lewis acidity of chloroaluminate ionic liquids refers to the molar ratio *x* of $AlCl_3$ to the EMImCl, which determines its corresponding speciation, physical- and electrochemical properties. In Lewis acidic compositions ($1 < x \leq 2$), aluminum exists primarily in the form of $AlCl_4^-$, which is the intercalating species and $Al_2Cl_7^-$ (**Eq. 6**), which is considered a Lewis acid due to its ability to accept electron pairs and run the electroplating of Al. On the other hand, it was possible to show *via* Raman investigations that with a mole ration $x > 1.90$ (**Eq. 7**) up to

the solubility limit of $x = 2$ (**Eq. 8**), the amount of $AlCl_4^-$ and $Al_2Cl_7^-$ decrease rapidly, due to larger complex anions like $Al_3Cl_{10}^-$ and $Al_4Cl_{13}^-$ appearing [61]. Al^{3+} ions are strongly tetrahedrally coordinated by the Cl^-- ions in the molten salt system due to the high charge density. Hence, the formation of $AlCl_4^-$ and $Al_2Cl_7^-$ in the electrolyte bulk is preferred over the "naked" Al^{3+} ions. Research has shown, that Cl^-, which serves as electron-pair donors and $AlCl_4^-$ co-exist in the $AlCl_3$:EMImCl ionic liquid when the ratio is $x < 1$ (**Eq. 3**) of $AlCl_3$ [62]. Under these conditions, the electrolyte is basic and thus not suitable for RABs anymore. An equimolar mixture, $x = 1$ (**Eq. 4**), contains mostly $AlCl_4^-$ anions, although small amounts of Cl^- and $Al_2Cl_7^-$ are always present due to the auto solvolysis (**Eq. 5**) reaction [63,64].

$$xAlCl_3 + EMImCl \rightarrow xAlCl_4^- + EMIm^+ + (1-x)Cl^- \quad (x < 1) \qquad (3)$$

$$xAlCl_3 + EMImCl \rightarrow xAlCl_4^- + EMIm^+ \quad (x = 1) \qquad (4)$$

$$2AlCl_4^- + 2EMIm^+ \rightleftharpoons Al_2Cl_7^- + Cl^- + 2EMIm^+ \ (auto\ solvolysis) \qquad (5)$$

$$xAlCl_3 + EMImCl \rightarrow (x-1)Al_2Cl_7^- + (2-x)AlCl_4^- + EMIm^+ \ (x > 1) \qquad (6)$$

$$AlCl_3 + Al_2Cl_7^- + EMIm^+ \rightleftharpoons Al_3Cl_{10}^- + EMIm^+ \ (1.9 < x \leq 2) \qquad (7)$$

$$AlCl_3 + Al_3Cl_{10}^- + EMIm^+ \rightleftharpoons Al_4Cl_{13}^- + EMIm^+ \ (1.9 < x \leq 2) \qquad (8)$$

Since the reduction of $AlCl_4^-$ takes place at a lower electrode potential than the organic cations of the ionic liquid, it is not possible to run electroplating of Al with Lewis basic and neutral ionic liquids as the electrolyte decomposes before electroplating can occur. Therefore, the use of IL electrolytes in RABs is limited to Lewis acidic melts containing $Al_2Cl_7^-$ anions [65].

2.4.4 Deep Eutectic Solvents (DESs)

The sensitivity to moisture, elevated costs and high corrosivity of IL electrolytes are a few reasons for the investigation and preparation of more inert and low-cost alternative electrolyte systems, such as deep eutectic solvents (DESs) [66,67]. DESs are made of mixtures of Lewis- or Brønsted acid/base couples. A Typical DESs contains Lewis acidic metal salts like $AlCl_3$ and a hydrogen bond donor or Lewis basic ligands, such as urea or acetamide [68]. DESs have a lower melting or "eutectic" point than their components and similar physical properties like ILs, such as low vapor pressures, a wide liquidus range and non-flammability, making them suitable for battery applications. The formation of cationic chloroaluminate species in the Urea-$AlCl_3$,

Urea-$AlCl_2^+$ and $(Urea)_2$-$AlCl_2^+$ (**Fig. 3 A-C**) system occurs *via* the coordination of aluminum with oxygen atoms of urea ligands.

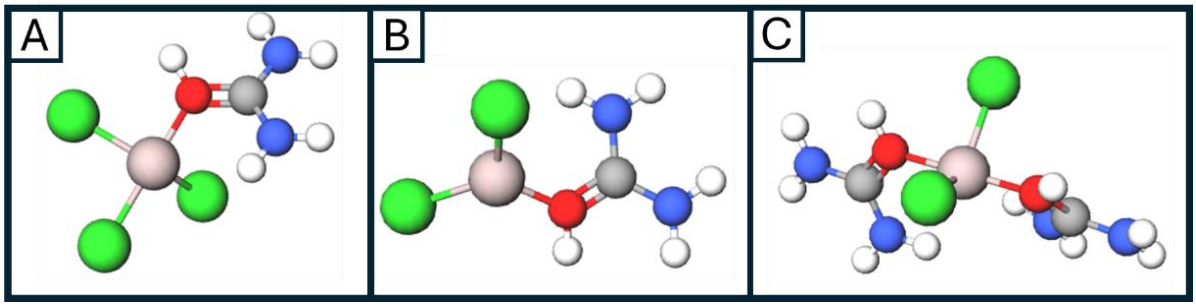

Figure 3 Structures of Urea-$AlCl_3$ (A), Urea-$AlCl_2^+$ (B) and $(Urea)_2$-$AlCl_2^+$ (C). The colours represent the following atoms: Beige (carbon-C), blue (nitrogen-N), green (chloride-Cl), grey (aluminum-Al), red (oxygen-O) and white (hydrogen-H). The molecules are drawn with MolView.

Aluminum electrodeposition in deep eutectic solvents occurs from both, anionic $Al_2Cl_7^-$ species and cationic species, such as $AlCl_2(urea)_n^+$ (**Fig. 3 B** and **C**) within the electrolyte [69,70]. In direct comparison between $AlCl_3$:EMImCl, $AlCl_3$:Urea and $AlCl_3$:Acetamide, all with the molar ratio of 1.5:1, in an Aluminum-Graphite cell show capacities of ~111 $mAh{\cdot}g^{-1}$, ~91 $mAh{\cdot}g^{-1}$ and 70 $mAh{\cdot}g^{-1}$, respectively, after 100 cycles at 50 $mA{\cdot}g^{-1}$. Also rate capability test at 50, 100, 200, 1000, 2000 and 50 $mA{\cdot}g^{-1}$ confirms the higher capacity and stability of the ILs. The better electrochemical performance of ILs is due to much lower viscosity and higher conductivity compared to the DESs [71].

2.4.5 Inorganic Molten Salts

Chloroaluminate-based inorganic molten salts became liquids at increased temperatures and were used for Al production through electroplating and as electrolytes for batteries [72]. The melting point of eutectic mixtures depends on the composition and molar ratio. For instance, a binary $AlCl_3$:NaCl (sodium chloride) and $AlCl_3$:KCl (potassium chloride) have a melting temperature of about 108°C and 128°C, respectively [73]. To obtain a more practical use for RABs, the melting points have been reduced below 100°C by utilizing a ternary $AlCl_3$:NaCl:KCl (61:26:13) molten salt system [74]. An Aluminum-Graphite battery cycled at ~120°C with the $AlCl_3$-NaCl-KCl molten salt electrolytes delivers a high capacity of 128 $mAh{\cdot}g^{-1}$ at 100 $mA{\cdot}g^{-1}$, outstanding cyclability and rate capability with still 63 $mAh{\cdot}g^{-1}$ at 8000 $mA{\cdot}g^{-1}$ [75]. Although $AlCl_3$:EMImCl IL electrolytes cannot compete with the great results of inorganic molten salts, the need for relatively high operating temperature is a huge drawback.

2.5 Working principle of Aluminum-Graphite (Al-C) Batteries

Research on RABs has primarily involved non-aqueous electrolytes, with reversible electroplating of heptachlorodialuminate ($Al_2Cl_7^-$) at the negative electrode and intercalation/deintercalation of tetrachloroaluminate ($AlCl_4^-$) anions at the positive electrode (**Fig. 4**). Such systems are called Al Dual-Ion Batteries (ADIBs), as the redox reactions at the electrodes involve two separate ionic species.

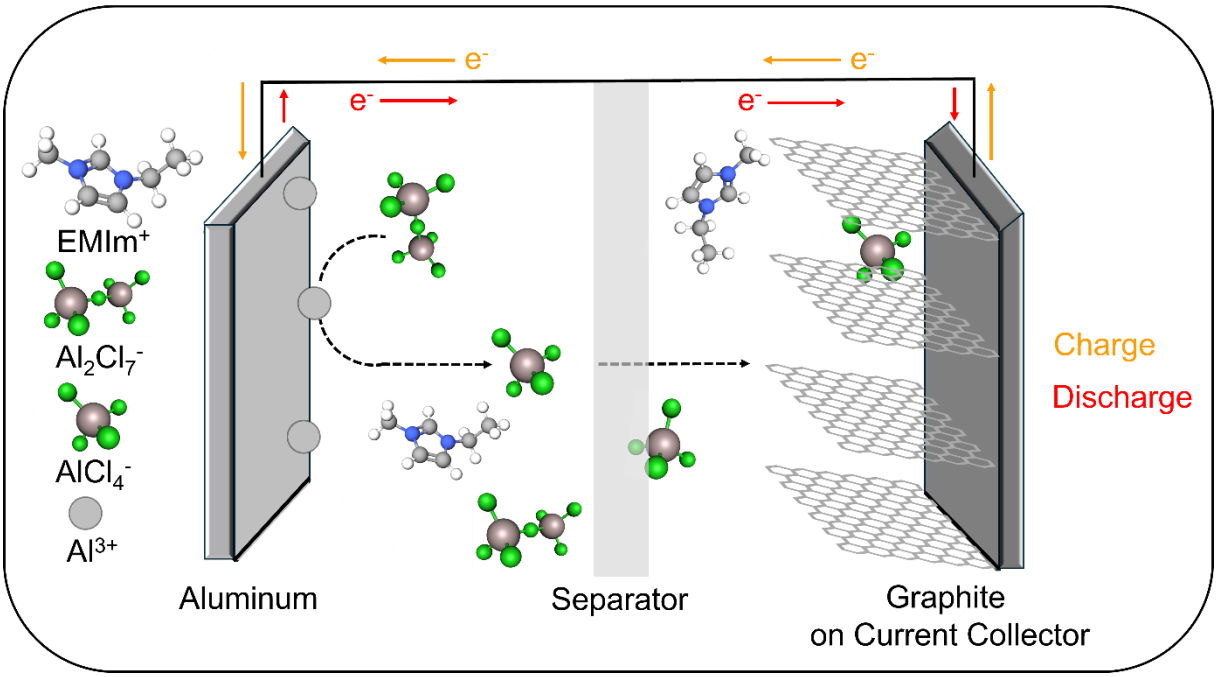

Figure 4 Schematic illustration of an Aluminum-Graphite (Al-C) battery based on a Lewis acidic $AlCl_3$:EMImCl ionic liquid electrolyte during charging.

The mechanism of an Al-C battery is fundamentally different from typical "rocking-chair" Lithium-Ion Batteries (LIBs) [13], which involve the shuttling of a single ionic species (Li^+) between the positive and negative electrodes. In LIBs, the concentration of ions within the electrolyte remains constant regardless of the state of charge. In the case of ADIBs, the concentration of chloroaluminate ions in the electrolyte decreases during charging and is mostly restored during discharge [13]. However, the intercalation of single-charged $AlCl_4^-$ anions limits the specific capacities of Al-C batteries to the theoretical capacity of the Graphite positive electrode of 240 $mAh \cdot g^{-1}$ [76]. Achieving high theoretical capacities of aluminum requires the intercalation of Al^{3+} ions. Unfortunately, the use of Al^{3+} ions is not possible due to the following reasons. The intercalation process of Al^{3+} is much more sluggish than lithium's or sodium's. With a size of 53.5 pm [7-9,77] are Al-cations significantly smaller than Li-ions (76 pm) [7-9,78] and

Na-ions (102 pm) [8,9,79]. The high valence state counteracts the advantage of the small ion radii. The high charge density of Al^{3+} results in numerous interactions inside the host lattice of cathode materials. This major impediment during diffusion leads to poor and slow kinetics and even worse, it can lead to irreversible changes/damages inside the host lattice of the cathode. Instead of pure Al^{3+} cations, Al-Cl complexes are formed and participate in the intercalation process. The reversible intercalation and deintercalation of $AlCl_4^-$ anions are reported to occur in graphitic carbon materials (**Eq. 9** and **10**) such as Graphite and Graphene but also in metal-organic framework (MOF)-derivatives and in a covalent-organic framework (COF) [80-81].

$$\text{Anode: } 4Al_2Cl_7^- + 3e^- \rightleftharpoons Al + 7AlCl_4^- \quad (9)$$

$$\text{Cathode: } C_n + AlCl_4^- \rightleftharpoons C_n[AlCl_4] + e^- \quad (10)$$

The size of $AlCl_4^-$ anions is ~ 5.28 Å [82] and, therefore, larger than the interlayer space of Graphite with 3.34 Å [83]. This means that the Graphite expands by 50 – 60 % during intercalation. In porous electrodes of Graphite powder, the volume expansion is 650 % when fully charged at 50 C [84]. The swelling of the cathode also deforms the separator. Therefore, the effective diffusion of ions through the separator increases during discharging and decreases while charging [84,85]. Furthermore, in contrast to commercial LIBs, the separator used in RABs is remarkably thicker, which requires a higher amount of electrolyte. This factor decreases the energy density concerning the mass of the whole cell and may lead to poor cycling performance. Until now, Graphite is still the best-known cathode material for Al batteries. $AlCl_4^-$ generates electron holes in bonding π-bands during insertion into Graphite materials, forming at the same time acceptor-type Graphite intercalation compounds (GICs). During the first cycles, the structure of the Graphite layers gets restructured to facilitate the subsequent intercalation. This structural change results in an increment of both, the specific capacity and the cell voltage. However, the rate capability is still poor due to the rate-determining nature of the intercalation process [77]. Several approaches have been proposed to increase the capacity of Graphite/Graphene cathodes, regarding their crystallinity and structural defects. For instance, the group of Dai *et al.* [78] tested Graphite flakes at specific currents of 66 $mA \cdot g^{-1}$ and 660 $mA \cdot g^{-1}$. They obtained a capacity of 110 $mAh \cdot g^{-1}$ at a lower current and 60 $mAh \cdot g^{-1}$ at a higher current, even after 6000 cycles with a coulombic efficiency (CE) of about 99.5 %. Those results indicate how important a high crystallinity and low defect density of Graphite materials are for high-

performance RABs. Similar results are shown by Chen *et al.* [79] with annealed graphene oxide (GO) aerogel. It was possible to show by Raman spectroscopy that $AlCl_4^-$ anions do not intercalate into the defect sites of the material. A second theory, which is not based on the defect-free mechanism, is developed by Lu *et al.* [86] The idea is based on nanovoids, which can attract and store more $AlCl_4^-$ ions and lead to an improved cathode capacity. This assumption could be proven with Graphene foam with nanoribbons, which were etched by ionized argon (Ar^+) plasma to obtain the highest possible porosity. The prepared foam shows a capacity of ~123 $mAh \cdot g^{-1}$ at a specific current of 5 $A \cdot g^{-1}$ and a CE > 98% after 10000 cycles. Even at a higher specific current (8 $A \cdot g^{-1}$), a capacity of 111 $mAh \cdot g^{-1}$ could be measured. Liu *et al.* [87] disclosed that the chloroaluminate anion intercalation in graphitic materials depends on the size in the *a*, *b* plane and *c* direction. This leads to the fact that by decreasing the vertical dimension (*c* direction) size, the kinetics of the $AlCl_4^-$ intercalation and deintercalation are more facilitated. Moreover, by increasing the size of horizontal dimensions (*a*, *b* planes), the structure can be stabilized during the charge and discharge process. To sum up, the fast-charging capabilities and long cycling lifetime of Al-C batteries, with modified graphitic positive electrode materials, make them promising candidates for future energy storage devices.

3. Materials, Experimental and Characterization methods

3.1 Materials

3.1.1 Chemicals and Foils

Cobalt(II)-acetate tetrahydrate ($C_4H_6CoO_4$ x $4H_2O$), ≥99 %, Fluka Analytical; Hexadecyltrimethylammonium bromide, CTAB, ($C_{19}H_{42}BrN$), ≥ 97 %, Merck; absolute Ethanol (C_2H_5OH), 100 %, VWR Chemicals; Potassium permanganate ($KMnO_4$), ≥ 99.0 %, Sigma-Aldrich; Polyethylene glycol ($H(OCH_2CH_2)_nOH$), Mn. 400, Sigma-Aldrich; Polyvinylidene chloride ($(-CH_2CCl_2-)_n$, PVdC), GoodFellow; Polyvinylidene fluoride ($(-CH_2CF_2-)_n$, PVdF) Solvay; *N*-Methyl-2-pyrrolidone (C_5H_9NO, NMP), 99.5%, Sigma-Aldrich; Dimethyl sulfoxide (C_2H_6OS, DMSO), ≥ 99.5%, VWR Chemicals; Hydrochloric acid 32%, Alpha chemicals; Acetone-D_6 (CD_3COCD_3), 99.9%, Sigma-Aldrich; Graphite (C), Mechano-Cap®1P1, H.C. Carbon; Carbon Black (C65), TIMCAL C-NERGY™; Copper sulfate pentahydrate ($CuSO_4$ x $5H_2O$), ≥99.0%, Nacalai Tesque Inc.; Aluminum chloride ($AlCl_3$), 99.999%, Thermo Scientific; Gallium chloride ($GaCl_3$), 99.99+%, Thermo Scientific; Metallic Gallium (Ga), 99.999%, Alfa Aesar: 1-Ethyl-3-methylimidazolium chloride ($C_6H_{11}N_2Cl$, EMImCl), 97% Thermo Scientific; Urea (CH_4N_2O), ≥ 98%, Sigma-Aldrich; *ortho*-(1,2)-Difluorobenzene (*o*-$C_6H_4F_2$), 99%, Apollo Scientific, Aluminum foil (Al), 99.0%, 0.025 mm thickness, GoodFellow; Molybdenum (Mo)-foil, 99.9%, 0.025 mm thickness, GoodFellow; Tungsten (W)-foil, 99.96%, 0.025 mm, GoodFellow; Molybdenum (Mo)-powder, 99.95%, 4-8 µm, Sigma-Aldrich; Carbon paper E15 (CP), 140 µm, QuinTech.

All chemicals, carbon paper, Mo-powder and metallic foils (Al, Mo and W) have been used as received without any further purification. All air and moisture-sensitive materials as well as dried electrodes, were stored inside an Argon (Ar) filled Glovebox (MBraun, oxygen (O_2) and H_2O < 0.5 ppm). Preparation of $AlCl_3$/EMImCl (1.5:1) and $GaCl_3$-based electrolytes, the assembling/reassembling of Swagelok-type or coin cells and washing of electrodes or binder sample powders have been always done under an inert Ar atmosphere. The used water (H_2O) has been always deionized laboratory water.

3.2 Experimental: Syntheses and Electrode preparation

3.2.1 Synthesis of Cobalt(II,III)-oxide

For the synthesis of 1.00 g pure cobalt(II,III)-oxide (Co_3O_4) cathode material, a typical hydrothermal method has been used. 1.03 g cobalt acetate tetrahydrate ($Co(CH_3COO)_2$ x $4H_2O$,

4.15 mmol) was dissolved in a 250 ml beaker with 60 ml deionized water. 80 mg hexadecyltrimethylammonium bromide (CTAB, $(CH_3(CH_2)_{15}(N(CH_3)_3$, 0.22 mmol) were added to the solution as a surfactant. Afterwards, 0.25 mg urea ($CO(NH_2)_2$, 4.14 mmol) were added to the solution. The clear pink solution was transferred into a Teflon-lined stainless-steel autoclave (100 ml capacity, PARR INSTRUMENT COMPANY) and sealed. Then, the hydrothermal synthesis was carried out in a drying and heating oven (BINDER) at 160 °C for 20 hours. After the heating process, the reaction vessel was allowed to cool down to room temperature. A pink solid was obtained, which was separated *via* filtration from the solution and was then washed several times, first with deionized water, followed by absolute ethanol. The solid intermediate product was stored overnight at 60 °C in an oven for drying. Finally, the dry solid was transferred into a porcelain crucible and it was heated in an ambient atmosphere at 500 °C for 4 hours in a muffle oven. The obtained product was a black powder, which was characterized *via* XRD (**Fig. S1** and **Table S1**) as a pure cubic Co_3O_4 (**Fig. S2**) compound.

3.2.2 Ball mill

The grinding of the Co_3O_4 has been done with a Fritsch Pulverisette 7 using ZrO_2 jars and milling balls. The ball milling was done for 16 hours at 500 rpm (revolutions per minute) under argon atmosphere. After every 10 minutes of grinding, the ball milling was stopped for 5 min to avoid too high temperatures and structural destruction or decomposition.

3.2.3 Magnetron sputtering of Titanium nitride on Stainless steel and Copper

The SS and Cu substrates had a temperature of 200°C and a bias voltage of -60 V during the production of the TiN layer by reactive dc-magnetron sputtering of Ti (6 kW, 400 x 100 cm) in an Ar/N_2 (nitrogen) plasma Ar/N_2=200:56 sccm (standard cubic centimeter per minute) and sputter pressure of 0.4 Pa, in a Hauzer HTC 625 coating facility. Before sputtering, both substrates were polished and cleaned in an ultrasonic bath of acetone for 15 min and by plasma etching in pure Ar at 0.7 Pa and -800 V. After reaching the temperature of 200°C, the residual gas pressure inside the sputter chamber was $6 \cdot 10^{-4}$ Pa. During the TiN deposition, the SS/Cu substrate was fixed on a rotating holder between the Ti target and sputtered for 10 hours.

3.2.4 Electrode preparation with Co_3O_4 and Mo as cathode material

The electrodes were prepared by mixing 80 w(%) (400.0 mg) cubic Co_3O_4 material, 10 w(%) (50.0 mg) C65 carbon additive and 10 wt(%) (500 0 mg) polyvinylidene fluoride (PVdF) binder (10 w(%)) dissolved in dimethyl sulfoxide (DMSO), in a DAC 150.1 FVZ SPEEDMIXER™ by HAUSCHILD. For slurry preparation, Co_3O_4 powder and C65 carbon were mixed and

ground in a mortar with a pestle. The powders were dry mixed in the SpeedMixer at 1000 rpm for two minutes. Afterwards, two drops of DMSO were added and mixed with the powder at 2500 rpm for two minutes. The addition of DMSO was repeated three times until a homogeneous paste was obtained. Next, the slurry was sonicated for five minutes to achieve good homogeneity and less agglomeration. Then, PVdF binder solution was added and speed-mixed at 800 rpm for ten minutes. The obtained suspension was coated with the doctor-blade technique on molybdenum (Mo; 99.9% purity, 0.025 mm thickness, GoodFellow) foil using a ZUA200 doctor blade from ZEHNTNER (on a Coatmaster 510 Film Applicator from ERICHSEN with automatic feed), with a wet thickness of 100 µm. The coated Mo-foil was dried under ambient conditions overnight. After that, the electrodes were dried in an oven at 60 °C for 6 h. Finally, the electrodes were punched out into 12 mm diameter discs (1.131 cm^2) and dried in a glass oven (Büchi glass oven B-585) in a vacuum at 120 °C for 12 h and then they were transferred into a Glovebox. The average mass of Co_3O_4 material on the electrodes was 0.73±0.09 $mg \cdot cm^{-2}$. The same procedure has been done to prepare electrodes with Mo-powder (99.95% purity, 4 to 8 µm particle size, Sigma-Aldrich). For these electrodes, tungsten (W; 99.96% purity, 0.025 mm thickness, GoodFellow) was used as the current collector instead of a Mo-foil. The adhesion between both metals was weak and the electrodes needed to be handled carefully. The average mass of the Mo-powder on the electrodes was 1.29±0.16 $mg \cdot cm^{-2}$.

3.2.5 Electrode preparation with PVdF/PVdC Binder- and Graphite active material

For the preparation of the PVdF-based electrodes, 90 w(%) Graphite (400 mg, 33.30 mmol, 67.96 eq.), 3 w(%) C65 conductive carbon (13.30 mg, 1.11 mmol, 2.27 eq.) and 7 w(%) of the 10 w(%) PVdF binder (311.10 mg, 0.49 mmol, 1.00 eq.), dissolved in *N*-Methyl-2-pyrrolidone (NMP) were used. In the case of the PVdC-based electrodes, 90 w(%) Graphite (400 mg, 33.30 mmol, 104.06 eq.), 3 w(%) C65 conductive carbon (13.3 mg, 1.11 mmol, 3.47 eq.) and 7 w(%) of the 10 w(%) PVdC binder (311.10 mg, 0.32 mmol, 1.00 eq.), dissolved in *N*-Methyl-2-pyrrolidone (NMP) were used. It is important to pay attention to the fact that the calculation of the amount of substance, in mole, and the corresponding equivalent are based on the real amount of pure binder material (31.10 mg) and not the 10% mixed solution. In addition, the calculation is based on the mono unit of the PVdF; M = 64.03 $g \cdot mol^{-1}$ and PVdC; M = 96.94 $g \cdot mol^{-1}$ of the polymer chain. For the preparation of the PVdF binder solution, 1.00 g of PVdF (15.62 mmol, 1.00 eq.) was added slowly under stirring to 10 ml NMP (103.90 mmol, 6.65 eq.). In the case of the preparation of the PVdC solution, 1.00 g PVdC (10.32 mmol,

1.00 eq.) was added slowly under stirring to 10 ml NMP (103.90 mmol, 10.07 eq.). Both, binder solutions were allowed to stir for 12 h before use. To prepare a slurry, Graphite, and C65 conductive carbon were mixed and ground in a mortar for ten minutes before the powders were further dry mixed for two minutes at 1000 rpm (revolutions per minute) by using a speedmixer (DAC 150.1 FVZ SPEEDMIXER^{TM} from Hauschild). Afterwards, 170 µl of DMSO were added as a wetting agent to obtain a thick paste and mixed again for two minutes at 1000 rpm. Further, 2 more drops of DMSO were added and mixed at 2500 rpm for two minutes. The last step was repeated until the slurry became a thick paste. As a next step, the mixture was sonicated for ten minutes and mixed at 2500 rpm for ten minutes to get a homogenous distribution of the components. Then, the corresponding binder solution was added and mixed at 800 rpm for an additional ten minutes. The obtained slurry was coated *via* the Doctor Blade technique on carbon paper with a wet thickness of 200 µm. The coated carbon paper was dried under ambient conditions inside a fume hood for 12 h. After that, the coating was dried in a Binder oven at 65 °C for 8 h. Then, electrodes were punched out to 12 mm diameter discs with a GN-CP20 punching machine from the Gelon group and dried in a Büchi B-585 glass oven under vacuum at 110 °C for 12 h. Finally, the electrodes were transferred into a Glovebox. The average mass loading for PVdF electrodes is 5.22±0.43 mg·cm^{-2} and for PVdC 5.63±0.48 mg·cm^{-2}.

3.2.6 Aluminum-Gallium (AlGa) alloy negative electrode preparation *via Ex-situ* method

The fabrication of the semisolid binary Aluminum-Gallium (Al_yGa_x) (mass ratio: y=10, 20, 30, 40 and x=90, 80, 70, 60, respectively) composites was done by mixing the corresponding amount of metallic Ga and Al-foil. At room temperature (RT), both metals of each mass ratio were continuously stirred, until no individual Ga or Al pieces were visible. Afterwards, the cement-like compounds were additional stirred for a further 15 min. For the preparation of round Al_yGa_x electrodes (1.131 cm^2), each ratio was heated to 50°C and poured into a 12 mm in diameter round PFA body shape. Next, all alloys were allowed to solidify at 0°C in a refrigerator for 12 hours.

3.3 Experimental: Preparation of Electrolytes

3.3.1 $AlCl_3$:EMImCl (1.5:1) ionic liquid Electrolyte preparation

The electrolyte for electrochemical measurements was prepared inside a Glovebox, filled with inert Argon (Ar) gas and a water and oxygen level of <0.1 ppm, respectively. The Lewis acidic ionic liquid electrolyte consists of 1-ethyl-3-methylimidazolium chloride (EMImCl) and

aluminum chloride ($AlCl_3$) in the molar ratio of 1:1.5. The ionic liquid was prepared by slow addition of 4.00 g $AlCl_3$ (30 mmol) to 3.09 g EMImCl (21.07 mmol) while stirring. It was necessary to combine both components slowly by adding only a small amount of $AlCl_3$ because the formation of the ionic liquid is an exothermic reaction. After the complete addition, the liquid was stirred for a further 24 hours. The resulting electrolyte was colourless/yellowish.

3.3.2 Preparation of $AlCl_3$/Urea (1.07:1) Electrolyte

Before use, urea was dried in a Büchi glass oven under vacuum at 100 °C for 6 h and then transferred into the Glovebox. For preparation, 0.82 g $AlCl_3$ (6.12 mmol, 1.07 eq.) and 0.346 g urea (5.76 mmol, 1.00 eq.) were mixed under stirring. After finishing the addition of both salts, the mixture was heated for 2 h at 60 °C. After, the clear, slightly Lewis acidic electrolyte was allowed to stir at room temperature for 12 h.

3.3.3 Preparation of 0.1 M, 0.2 M, 0.3 M and 0.5 M $GaCl_3$ containing electrolytes

The electrolytes for electrochemical measurements were prepared inside a Glovebox, filled with inert Argon (Ar) gas and a water and oxygen level of <0.1 ppm, respectively. The Lewis acidic ionic liquid electrolyte consists of 1-ethyl-3-methylimidazolium chloride (EMImCl) and aluminum chloride ($AlCl_3$) in the molar ratio of 1:1.5. The ionic liquid was prepared by slow addition of 4.00 g $AlCl_3$ (30 mmol) to 3.09 g EMImCl (21.07 mmol) while stirring. For the preparation of pure $GaCl_3$:EMImCl ionic liquid electrolyte, 2.64 g $GaCl_3$ (14.99 mmol) and 1.46 g EMImCl (9.96 mmol), were added slowly, under stirring, together. For the preparation of 0.1 M, 0.2 M, 0.3 M and 0.5 M $GaCl_3$-containing electrolytes, the following amounts of $GaCl_3$ were added, under stirring, into 1 ml fresh prepared $AlCl_3$:EMImCl (1.5:1) ionic liquid electrolyte: 0.1 M = 17.61 mg; 0.2 M = 35.22 mg; 0.3 M = 52.82 mg; and 0.5 M = 88.04 mg of $GaCl_3$. It was necessary to combine all components slowly, while stirring, by adding only a small amount of $AlCl_3$/$GaCl_3$ to EMImCl because the formation of the ionic liquids is an exothermic reaction. After the complete addition, the liquids were stirred for a further 12 hours.

3.4 Experimental: Cell assembly and Electrochemical characterizations

3.4.1 Cell assembly of PFA Swagelok cell-type

The PFA Swagelok cells, whose pistons are made of Mo (later W, see **Chapter 4**), were arranged in a two-electrode configuration for electrochemical measurements. The aluminum (Al; 99.0% purity, 0.025 mm thickness, GoodFellow) anode is used as both, a reference- and counter electrode (CE). The cathode electrode discs were punched out with a manual punching

machine GN-CP20 from GELON GROUP. The pure aluminum anode electrode discs (12 mm in diameter) and separator (13 mm in diameter) were punched out with a TURNUS bracket hollow. Each cell part of the Swagelok cell was dried overnight at 120 °C in a drying and heating oven from BINDER and inserted afterwards into an Ar-filled Glovebox from MBRAUN with an oxygen (O_2) and water (H_2O) level less than 0.5 ppm to assemble the cells. A 12 mm diameter coated working electrode was placed in the cell followed by a 13 mm diameter vacuum dried inside a Büchi glass oven B-584 glass-fiber separator (GF/D from WHATMAN®). Then 200 µl of EMImCl-$AlCl_3$ (1:1.5) ionic liquid was added and covered with a second separator and the same amount of electrolyte was added. The counter/reference aluminum electrode was placed on top of the second separator. All electrochemical measurements (GCPL with a specific current of 20 $mA \cdot g^{-1}$ and CV with a scan rate of 0.5 $mV \cdot s^{-1}$ in the potential window 0.3 V- 2.2 V *vs.* Al) were carried out using a VMP3 multichannel potentiostat/galvanostat from BIO-LOGIC SCIENCE INSTRUMENTS (France), equipped with the EC-Lab® software. A schematic illustration of an assembled PFA Swagelok cell is shown in **Figure 5**.

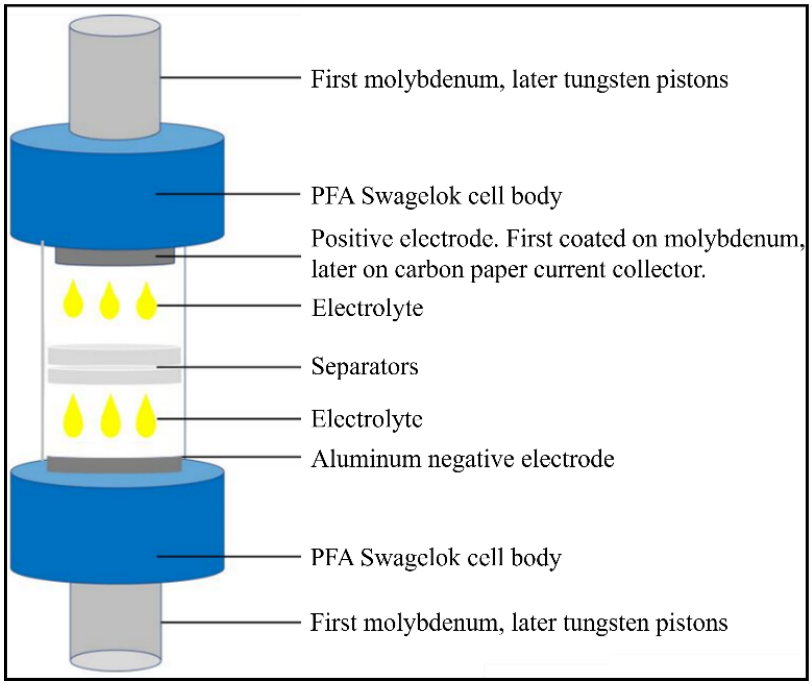

Figure 5 Schematic illustration of an assembled Swagelok cell with different current collector materials and corresponding Lewis acidic ionic liquid electrolyte.

3.4.2 Cell preparation and assembly for Synchrotron measurements

All electrochemical measurements have been done with a two-electrode configuration using a Swagelok-type cell, whereby the rods are made of tungsten (W) to avoid any side-reactions with the Lewis acidic electrolytes [38] or alloying with $GaCl_3$/Ga metal. To assemble the cell, first, a 12 mm in diameter Al-foil (1.131 cm^2, punched out with a Turnus bracket hollow) was placed on one piston screwed to the PFA Swagelok Tube Fitting, PFA-820-3. On top of the Al-foil, a 13 mm in diameter glass-fiber separator (Whatman, GF/A) was placed. The separator was punched using a GN-CP20 punching machine from the Gelon group. This separator was soaked with 200 µl of ionic liquid electrolyte before a second separator was placed into the cell-body part. An additional amount of 100 µl of electrolyte was added to wet the second separator. Finally, the Graphite electrode (or second Al-foil for assembling symmetrical cells) was inserted before the Swagelok cell was closed. All electrochemical tests were carried out using a VMP3 multichannel potentiostat/galvanostat from BIO-LOGIC SCIENCE INSTRUMENTS (France), equipped with the EC-Lab®, software version V11.43. Furthermore, all test cells were placed in a climate chamber at a constant temperature of 25±1 °C. Galvanostatic charge/discharge cycling with potential limitation (GCPL) experiments were performed in a potential window of 0.3 – 2.3 V *vs.* Al with a specific current of 20 $mA \cdot g^{-1}$. The rate tests have been performed at the following currents: 20, 50, 100, 200, 500, 1000, 20 and 10 $mA \cdot g^{-1}$, respectively, whereby the mass is referred to the amount of Graphite. Cyclic voltammetry (CV) was performed with a scan rate of 0.1 $mV \cdot s^{-1}$ from 0.3 – 2.3 V *vs.* Al. To investigate the dependency of different scan rates on the surface- or diffusion-controlled nucleation, 5, 10, 20 and 30 $mV \cdot s^{-1}$ have been applied. The assembled Al-Graphite cells' average open-circuit voltage (OCV) was recorded for 70-72 hours. Sample preparation for the *ex-situ* extended X-ray absorption fine structure (EXAFS) was done as follows: As standard and calibration materials, pure Al-foil, metallic Ga and $GaCl_3$ powders have been used without any pretreatments or purification steps. To obtain AlGa alloy samples, Al-Graphite Swagelok cells with pure $GaCl_3$:EMImCl (1.5:1) and the additive of 0.1 M, 0.2 M, 0.3 M and 0.5 M $GaCl_3$ in the $AlCl_3$:EMImCl (1.5:1) ionic liquid electrolyte, were assembled. By chronoamperometry, each cell was held for 2 hours at a constant potential of 0.3 V *vs.* Al (electrostripping/dealloying) and 2.2 V *vs.* Al (electroplating/alloying). Afterwards, the cells were reassembled inside a Glovebox and the AlGa and Graphite samples were washed with 1,2-Dichlorobenzene and dried at room temperature (25°C) under vacuum for 12 hours. The EXAFS measurements of all samples were conducted in a 2025-type coin cell with a 5 mm diameter Kapton window. All EXAFS spectra were analyzed and processed utilizing the

Demeter software package [88] and electrochemical data evaluation was done with OriginPro 2023 from OrginLab.

3.5 Characterization techniques

3.5.1 Extended X-Ray Absorption Fine Structure (EXAFS) Spectroscopy

EXAFS measurements in fluorescence mode were performed at the Ga K-edge on the CLÆSS beamline at ALBA CELLS synchrotron (Barcelona, Spain). Multi-shell Fourier approach was applied for EXAFS data analysis. Background subtraction, normalization, energy alignment and extraction of $\chi(k)$ oscillatory functions were performed in Athena program of the Demeter package [88]. Further analysis in Artemis program included the calculation of theoretical amplitudes and phases by the FEFF6 code [89] and shells fitting in the R-range from 1.4 to 5.0 Å of the Fourier-transformed data k^2-weighted $\chi(k)$ applying Δk Hanning window from 3 to 7 $Å^{-1}$ with the width of the window slope $\Delta k = 1$ $Å^{-1}$. The fitting parameters were the first shell Me-Me interatomic distance (R_{Me-Me}), Debye-Waller factor (σ^2) and zero energy shift (ΔE_0). The passive electron reduction factor S_0^2 was set equal to 0.7 according to the analysis of reference data. As a crystal model the cubic structure Fm-3m of Al metal was chosen (ICSD 18839).

3.5.2 Fourier-Transform Infrared (FT-IR)

FT-IR active vibration modes were measured with a Bruker Tensor 27 FTIR spectrometer. Data evaluation was done with Origin2023 from ORIGINLAB.

3.5.3 Inductively Coupled Plasma – Optical Emission Spectroscopy (ICP-OES)

ICP-OES was performed by an OPTIMA 4300DV (Perkin-Elmer) with an Echelle polychromator and a solid-state detector (custom, two-dimensional CCD array). Before the ICP-OES measurement, all samples were dissolved in *aqua regia* (hydrochloric acid: nitric acid in the ratio 3:1, respectively).

3.5.4 Hydrogen and Carbon Nuclear Magnetic Resonance (^{1}H- and ^{13}C-NMR)

^{1}H-and ^{13}C-NMR spectra have been recorded with a Bruker Avance 400 spectrometer with an applied frequency of 400 MHz. As a solvent, d6-acetone ($(CD_3)_2CO$; 99.9 atom% D, Sigma-Aldrich) has been used. Data evaluation was done with MestReNova from Mestrelab Research, software version 14.1.2-25024.

3.5.5 Magnetometry

Direct current (DC) magnetometry data has been measured with a Physical Property Measurement System (PPMS) DynaCool from Quantum Design equipped with a Vibrating Sample Magnetometry (VSM) option. The magnetic moment was measured from 2 to 160 K at a magnetic field of 5 kOe with an average signal acquisition time per measuring point of 10 seconds for all samples. Liquids were measured in a custom-made sample container based on magnetically clean drinking straws (QDS-8000-001 from Quantum Desing). To prepare 100 mg of the red-coloured electrolyte consisting out of (partially) dissolved Mo and $AlCl_3$:EMImCl, 7.165 mg Mo metal were immersed for 72 hours in 92.836 mg clean electrolyte. 100.3(1) mg of such red-coloured electrolyte with immersed Mo was measured and the raw magnetic moment (emu) was normalized to 100 mg (that would contain 7.165 mg Mo) and to a magnetic field of one Oe. Further, 156.2 mg of the pure electrolyte (without Mo) were measured and the raw magnetic moment was normalized to 92.835 mg and to a magnetic field of one Oe. The magnetic contribution stemming exclusively from the 7.165 mg of immersed Mo (blue symbols in **Fig. 6**) has been obtained by subtracting the signal from the pure electrolyte (orange symbols in **Fig. 6**) from the signal of the electrolyte with the immersed Mo (red symbols in **Fig. 6**). For comparison, Mo metal powder (38.5 mg) and Mo-foil (31 mg) were measured within polypropylene sample capsules (QDS-4096-388 from Quantum Design) and the measured raw data magnetic moment have been normalized to 7.165 mg and to a magnetic field of one Oe.

3.5.6 Raman spectroscopy

Raman active modes were measured by a Raman spectrometer (LabRam, Evolution HR, HORIBA Jobin Yvon) with 633 nm laser excitation wavelength in a range from 100 to 4000 cm^{-1}. Data evaluation was done with Origin2023 from ORIGINLAB.

3.5.7 Scanning Electron Microscopy (SEM) and Energy-Dispersive X-ray Spectroscopy (EDS)

SEM investigations were conducted by a thermal field emission scanning electron microscope (FESEM, Carl Zeiss SMT AG) at an acceleration voltage of 5 kV. The samples were fixed on a steel sample holder by using adhesive tape. Cross-section SEM images were taken with a Zeiss Supra 55 device by using a broad ion beam slope cutting (BIBSC) technique to produce smooth surfaces. Surface and morphology examinations conducted in Japan, were done at room temperature by SEM (JSM-6510A, JEOL Ltd.) Distributions and homogeneity of

elements were investigated by EDX spectroscopy (JED-2300, JEOL Ltd.) with an accelerating voltage of 15 kV.

3.5.8 X-ray Photoemission Spectroscopy (XPS)

XPS measurements were performed using a K-Alpha XPS spectrometer from Thermo Fisher Scientific (East Grinstead). The samples were irradiated with monochromatic Al-Kα X-rays with a spot size of about 400 µm. The photoelectrons were detected with a hemispherical 180 dual-focus analyzer with 128 channel detectors. To prevent any localized charge buildup, the Kα charge compensation system was employed during analysis, using electrons of 8 eV energy and low-energy argon ions. The samples were fixed on a steel sample holder by using Cu-based adhesion tape. For data evaluation, Avantage 5.9925 Surface Chemical Analysis software from Thermo Fischer Scientific was used.

3.5.9 X-ray Diffraction (XRD)

XRD diffractogram of the Co_3O_4 compound is recorded in glass no. 50 capillary from Hilgenberg at room temperature using an X-ray powder diffractometer from STOE STADI P. The device operates with Mo Kα_1 radiation (λ=0.7039 Å). All diffraction pattern are analyzed by full-pattern Rietveld refinement, using the software package FullProf [90] and plotted with Origin2023 from ORIGINLAB. The structure of Graphite positive electrode samples was determined by X-ray diffraction using synchrotron radiation with the wavelength λ = 0.4132 Å at the MSPD Beamline at ALBA in Barcelona, Spain. The diffraction data are analyzed by Le Bail fitting using the FullProf software package [90]. Alloying and TiN sputtered samples are recorded with a Rigaku Ultima IV diffractometer with a Cu Kα 1.5406 Å X-ray source.

4. Instability of the Molybdenum Current Collector

4.1 Introduction: History of Current Collector Materials for RABs

Since Al tends to form a passivation layer of non-conductive aluminum(III)-oxide (Al_2O_3) on the surface, which harms the electroplating and electrostripping ability [91,92], it is necessary to remove the protective layer. Moreover, to obtain a reversible electroplating, the use of a Lewis acidic ionic liquid (IL) electrolyte made of aluminum chloride ($AlCl_3$) and 1-ethyl-3-methylimidazolium chloride (EMImCl) with a molar ratio $x > 1$ for $AlCl_3$ is required [93]. The latest findings prove that the ratio of 1.5:1 is the ideal compromise between electroplating/electrostripping ability and corrosion effects [93,94]. Furthermore, the ionic liquid forms the $AlCl_4^-$ complex, which can intercalate into the host lattice of the cathode materials (Graphite, for instance). Since the high charge density of Al^{3+} results in numerous interactions inside the host lattice of any material that leads to slow kinetics, Al^{3+} cannot be used and must be complexed by chloride anions. On the other hand, because of the high Lewis acidity of such ionic liquid electrolytes, the pure Al negative electrode suffers from pulverization, formation of inactive Al, dendrites, and corrosion [95]. Furthermore, $AlCl_3$-based ionic liquid electrolytes are costly, sensitive to air and moisture and they have a low anodic limit potential making it impossible for positive cathode materials, like metal-oxides (V_2O_5) [96] or -sulfides (Ni_3S_2) [97], to be charged to high voltage, reducing the available energy density. At high potentials, side-reactions, through the decomposition of the electrolyte and evolution of chlorine (Cl_2)-gas, are occurring. The anodic limiting potential of the $AlCl_3$:EMImCl electrolyte is reported to be less than 2.6 V (*vs.* Al) and becomes lower with increasing amounts of $AlCl_3$ (1.8 V (*vs.* Al) at a molar ratio of 2:1) [92]. The selection of the cut-off voltage for charging is one example of controversial data in the literature. Jiao *et al.* [95], for instance, reported a maximum limit of 2.3 V *vs.* Al for the 1.5:1 molar ratio electrolyte. It is worth noting that common aluminum chalcogen batteries such as sulfur (S), selenium (Se), and tellurium (Te)-based ones, suffer from capacity loss because of their chemical dissolution and even the dissolution of the oxidation products of the cathode into the electrolyte (**Chapter 2.3.2**, **Eq. 1** and **2**) [92,98,99]. Furthermore, due to electrochemical decomposition and dissolution, the active materials can detach from the current collector and solubilize into the ionic liquid and migrate/deposit on the negative electrode (so-called “shuttle effect”) [92,100]. The same behavior has been observed for the common V_2O_5 cathode compound [25]. It seems that all electrophilic elements (oxygen (O), S, Se, and Te) of the VI A group react and interact with the $AlCl_3$/EMImCl electrolyte [92,101]. However, in the early stage of investigations, several reports describe V_2O_5 to be a great cathode material for

$AlCl_3$-based RABs [30,96,102]. In 2011, Jayaprakash *et al.* [96] reported V_2O_5 to be a suitable Al^{3+} intercalation cathode material. The active material was coated on stainless steel (SS) and the measurements were done in SS coin cells. Two years later, Reed *et al.* [11] demonstrated that the whole electrochemical contribution came from the SS and not from the V_2O_5. The containing elements of SS, iron (Fe), and chromium (Cr) react with the $AlCl_3$-based ionic liquid to the corresponding metal chlorides [11] (**Eq. 11** and **12**):

$$4AlCl_4^- + Fe \rightleftharpoons 2Al_2Cl_7^- + FeCl_2 + 2e^- \quad (11)$$

$$4AlCl_4^- + Cr \rightleftharpoons 2Al_2Cl_7^- + CrCl_2 + 2e^- \quad (12)$$

In 2015, Wang *et al.* [30] replaced the SS with a nickel (Ni) foam as a current collector and the V_2O_5 positive electrode gave an initial discharge capacity of 239 $mAh \cdot g^{-1}$. Three years later, the reactivity between Ni and the $AlCl_3$:EMImCl (1.3:1) ionic liquid electrolyte has been demonstrated by Oh *et al.* [103] and the suggested reaction is shown below (**Eq. 13**):

$$xNi^{2+} + 4(1-x)Al_2Cl_7^- + (3-x)e^- \rightleftharpoons Ni_xAl_{1-x} + 7(1-x)AlCl_4^- \quad (13)$$

Table 2 Statistic representation of current collector materials used in RABs before 2018 (a) and starting from 2018 till present (b). Adapted from Journal of Physics: Energy Vol. 6 No.3 by Rosa M. Palacin *et al*. Copyright 2024 by IOP Publishing [24].

Current Collector (CC)	(a) before 2018; percentage [%]	(b) from 2018 till present; percentage [%]
Nickel (Ni)*	27	~9
Molybdenum (Mo)	16	~50
Stainless Steel (SS)#	11	~3 (sputtered with TiN or Cr_2N)
Carbon Paper (CP)	11	-
Glassy Carbon (GC)	9	~13
Tantalum (Ta)	9	~6
Tungsten (W)	5	~13
Inconel alloy (IA)	5	-
Platinum (Pt)	5	-
Titanium (Ti)	2	-
Carbon Fiber (CF)	-	~3
Niobium (Nb)	-	~3

The reaction of Ni occurs immediately after immersion into the ionic liquid electrolyte. Additionally, nickel(II)-oxide (NiO) and nickel(III)-oxide (Ni_2O_3) are formed on the surface by soaking the Ni metal for 10-30 days in the electrolyte as has been proven by XPS [103]. Similar to those results, tungsten (W) is mentioned to react with the electrolyte [103]. Obviously, it is difficult to find a stable current collector material for RABs. Therefore, Wang *et al.* [12] published an overview of suitable and unsuitable current collector materials in the potential range of 0-2.5 V *vs.* Al while using the strongest Lewis acidic ionic liquid electrolyte with the molar ratio of 2:1 ($AlCl_3$:EMImCl). The authors describe that Cr, SS, Al, titanium (Ti), and even gold (Au) are not suitable for $AlCl_3$:EMImCl-based RABs. They report higher stability for molybdenum (Mo), glassy carbon (GC), tungsten (W), chromium nitride (Cr_2N), and titanium nitride (TiN). Nickel is not mentioned, although it has been the most common current collector for RABs until 2018 [7,24] (**Table 2**). While Oh *et al.* [103] reported Mo to be more stable than W in an even lower Lewis acidic electrolyte with a molar ratio of 1.3:1, Wang *et al.* [12] describe the opposite. Further, Chen *et al.* [35] propose tantalum (Ta) as well as indium tin oxide (ITO) as a novel current collector, stable up to 2.75 V *vs.* Al. More importantly, Chen *et al.* [35] describe platinum (Pt) as well as Mo to oxidize at 1.8 V and 2 V in $AlCl_3$-EMImCl, 1.3:1 molar ratio, electrolyte. However, no further effort has been made to investigate the redox activity of Mo and its influence on the electrochemical performance. Nearly the same redox behaviour (1.85 V and 1.98 V *vs.* Al) is shown for Mo by Yu *et al.* [104] but like a lot of other authors, they use Mo-foil as a current collector since they falsely assumed the activity would be neglectable. In the following, the actual influence of side-reactions between the Mo current collector and the $AlCl_3$-based ionic liquid electrolyte on the electrochemical performance of RABs is demonstrated. In addition, it was possible to show that a coated layer of an inactive cobalt(II,III)-oxide (Co_3O_4), initially supposed to be an active material [105], hampers the reaction of the Mo current collector with the electrolyte.

4.2 Results and Discussions

After immersion of Mo-foil or powder with a bigger surface area (4 to 8 µm particle size), the colourless/yellowish $AlCl_3$-EMImCl (1.5:1) ionic liquid electrolyte turns red after a few seconds. This is the first indication that side-reactions take place, leading to the formation of Mo-cations that can form complexes with the $AlCl_3$-based ionic liquid. For clarity, in the following, in Lewis acidic electrolyte immersed Mo will be labelled as Mo-$AlCl_3$-EMImCl. Only a few authors, such as Chen *et al.* [35], who presented an alternative non-metallic indium tin oxide (ITO)-based current collector, mention a side effect of Mo to occur. However, in their

report, the oxidation of Mo is explained to occur due to the residual amount of water in the electrolyte. To ensure that the ionic liquid is water-free, ^{1}H- and ^{13}C-NMR (nuclear magnetic resonance) spectroscopy has been done. **Figure 6 A** and **B** show the ^{1}H- and ^{13}C-NMR of freshly prepared $AlCl_3$-EMImCl ionic liquid. All signals of both spectra can be assigned to the $EMIm^+$ cation. No hydrogen water peak at 2.84 ppm is visible before (**Fig. 6 A**) and after the immersion of Mo (**Fig. 6 C**). Since no signal appears, it can be assumed that the residual water amount is below the detection limit (0.01 mol·kg^{-1} or 0.02 wt.%) [106]. **Figure 6 C** and **D** show the ^{1}H- and ^{13}C-NMR measurements of the red Mo-$AlCl_3$-EMImCl.

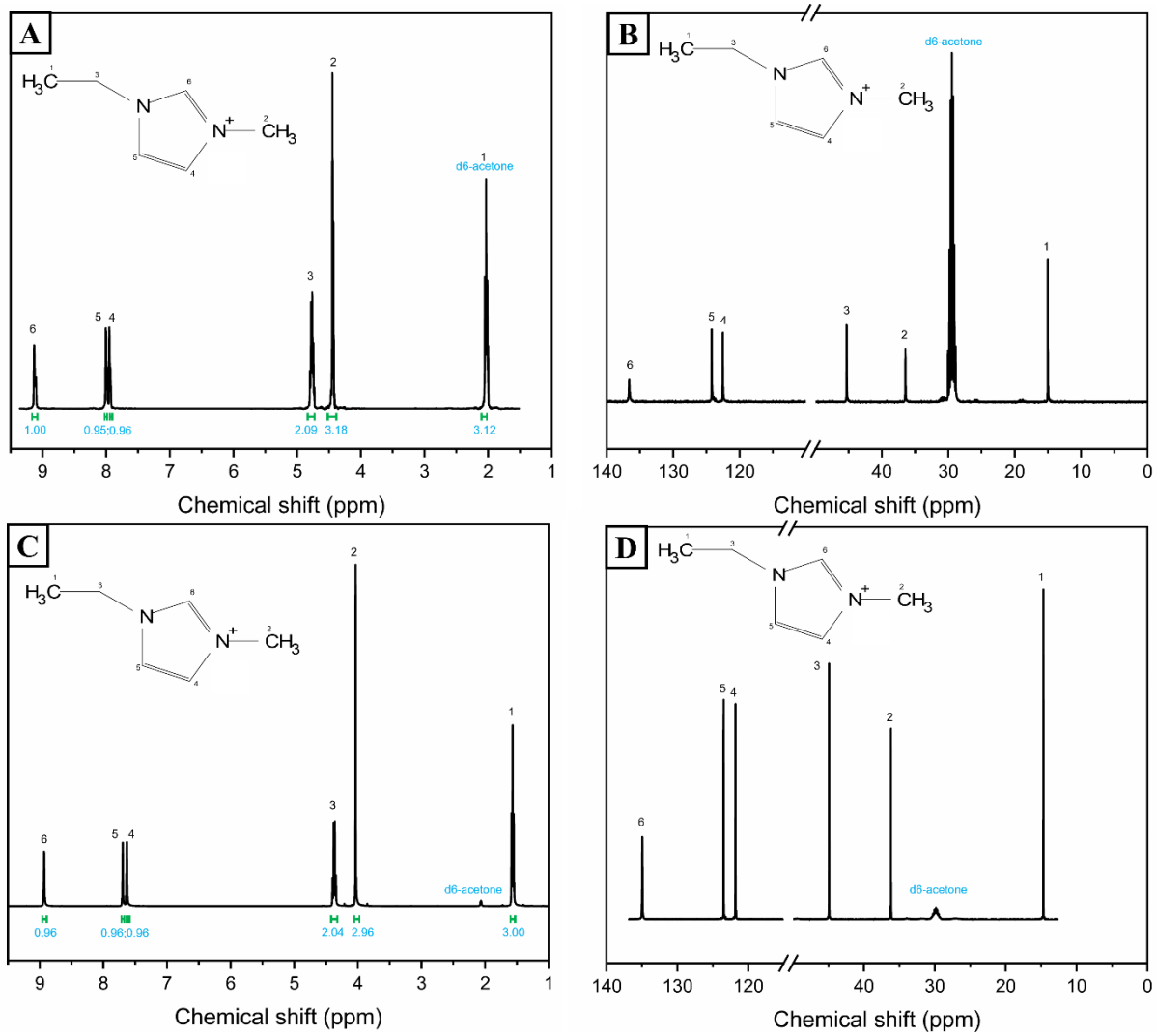

Figure 6 ^{1}H- and ^{13}C-NMR of freshly prepared $AlCl_3$-EMImCl electrolyte (A, B) and ^{1}H- and ^{13}C-NMR of red Mo-$AlCl_3$-EMImCl (C, D), respectively. Reprinted from Journal of Power Sources Vol. 633 by E. Zemlyanushin *et al*. Copyright 2025 by Elsevier [38].

Both NMR spectra (**Fig. 6 C** and **D**) prove that no structural change of the $EMIm^+$ happens after contact with a Mo source. Furthermore, no significant chemical shift occurs for the carbon

atoms of the $EMIm^+$. On the other hand, a slight upfield shift (~0.5 ppm) of all ^1H signals occurs for the Mo-$AlCl_3$-EMImCl sample. This phenomenon can be caused by an increased electron density around the hydrogen atoms due to the presence of metal cations. The increased electron density shields the hydrogen nucleus from the external magnetic field, resulting in an upfield shift [107]. Similar NMR results have been obtained for an EMImCl-$PbCl_2$ (lead(II)-chloride) system by Tan *et al.* [108], where $[Pb_mCl_{2m+1}][EMImCl]_n^-$ (m=1,2 and n=1-4) clusters or complexes have been formed. It should be noted that this Pb-Cl-EMImCl investigation has been done without the addition of $AlCl_3$. However, it is possible that molybdenum dissolves in the ionic liquid and forms similar complexes or clusters. Inductively coupled plasma optical emission spectroscopy (ICP-OES) confirmed that in 5 mg saturated Mo-$AlCl_3$-EMImCl electrolyte, it was possible to dissolve 1.99±0.06 w(%) of Mo. It should be noted that any remaining Mo nanoparticles (NP) that stay unfiltered can distort the ICP-OES result. Based on the result of ICP-OES, temperature-dependent magnetic susceptibility χ measurements have been performed. As shown in **Figure 7**, the pure $AlCl_3$-EMImCl ionic liquid electrolyte exhibits temperature-independent Langevin diamagnetism over almost the whole investigated temperature range from 160 K down to approximately 10 K. Below 10 K, the electrolyte is supposed to undergo a phase transition with an accompanying increase of electron density and corresponding stronger diamagnetic signal. On the other side, Mo metal (measured here as Mo-foil and powder, respectively) only exhibits a weak positive temperature-independent Pauli paramagnetism over the whole temperature range. When Mo metal powder has been immersed and stirred for 72 h in $AlCl_3$-EMImCl (1.5:1) ionic liquid electrolyte, the susceptibility increases strongly when the temperature is lowered as it is characteristic for Langevin-type paramagnetism of localized magnetic moments. The magnetic susceptibility that exclusively stems from the (partially) dissolved Mo can be obtained by subtracting the signal contribution of the pure electrolyte from that of the Mo immersed in the electrolyte (see experimental section for details). A Curie-Weiss fit (inset of **Fig. 7**) according to $\chi^{-1} = C^{-1}(T - \theta)$, with the Curie constant *C*, and the Weiss constant θ, has been done from 2 to 150 K. Referring to the total amount of Mo atoms contained in 7.165 mg Mo, a molar Curie constant of C_{mol}=2.70(1) $\cdot 10^{-2}$ $cm^3 \cdot K \cdot mol^{-1}$ is obtained that corresponds to a localized paramagnetic moment of 0.47(1) μ_B per Mo atom on average. Alternatively, the Curie constant could also be explained by approximately 8% of all Mo atoms exhibiting a single unpaired electron with paramagnetic moment of 1.73 μ_B. The obtained small negative Weiss-constant of $\theta = -2.7(4)$ K points either to a realized weak antiferromagnetic coupling between the Mo magnetic moments in a multi Mo containing complex and /or to weak single-ion anisotropy [109].

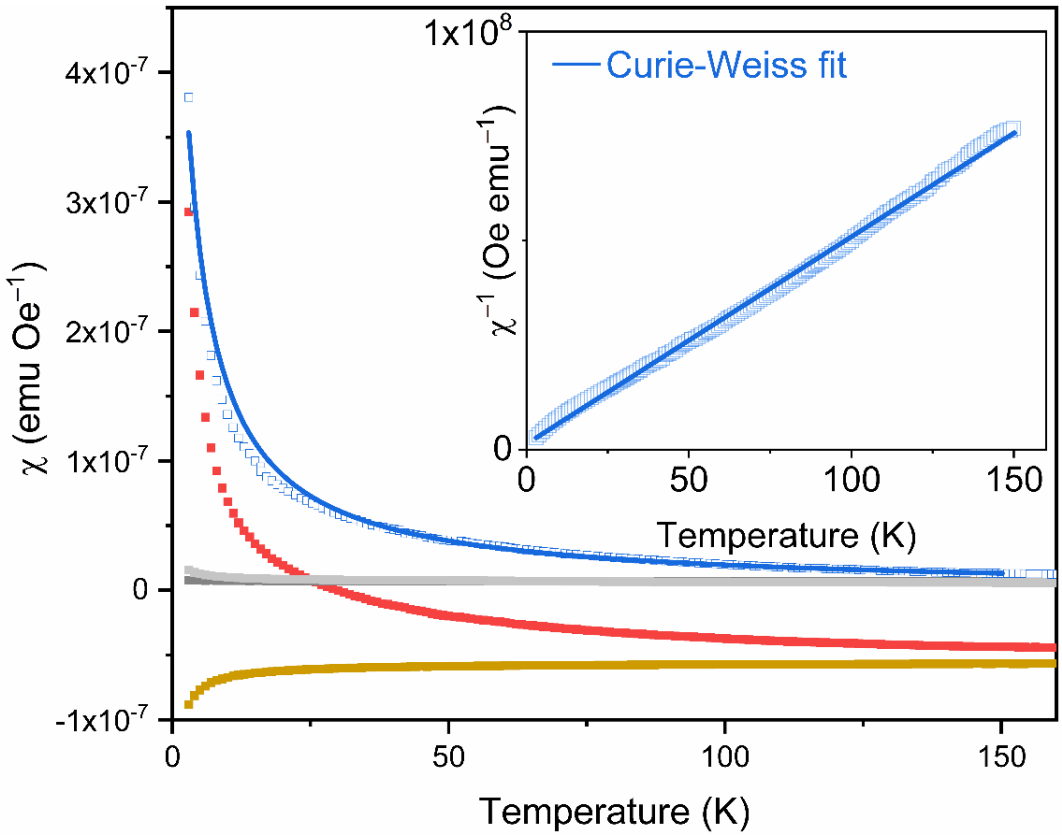

Figure 7 Magnetic DC susceptibility *vs.* temperature of Mo-$AlCl_3$-EMImCl (red), pure electrolyte (orange), metal Mo-foil (dark grey), and Mo-powder (light grey), Langevin-type paramagnetic contribution stemming from the immersed Mo (blue), and Curie-Weiss fit (blue solid line). The inset shows an inverse DC susceptibility *vs.* temperature plot. Reprinted from Journal of Power Sources Vol. 633 by E. Zemlyanushin *et al*. Copyright 2025 by Elsevier [38].

Misirlioğlu and Aksüt [110] demonstrated the formation of $[MoOCl_4]^-$ depending on the Cl^- concentration in a HCl solution, and $[MoOCl_4]^-$ is paramagnetic [111]. On the other hand, the formation of solvable $Mo^{(II-VI)}Cl_{(2-6)}$ complexes are also possible. Estager *et al.* [112] show in their review article from 2014 that such dissolution behavior of metal chlorides, like $CoCl_2$, $NiCl_2$, $FeCl_2$, $FeCl_3$, $CuCl_2$, $MoCl_3$, and $MoCl_4$, in basic chloroaluminate ionic liquid is possible. Ultraviolette-visible (UV-VIS) spectra (**Fig. 8 A** and **B**) of the red Mo-$AlCl_3$-EMImCl electrolyte have been recorded to get more information about potentially formed Mo cations. For dilution of the liquid sample, 1,2-Difluorobenzene (DFB) has been chosen since the solvent does not react with the ionic liquid and does not overlap with the UV-VIS bands of the red electrolyte with dissolved Mo cations (**Fig. 8 A**).

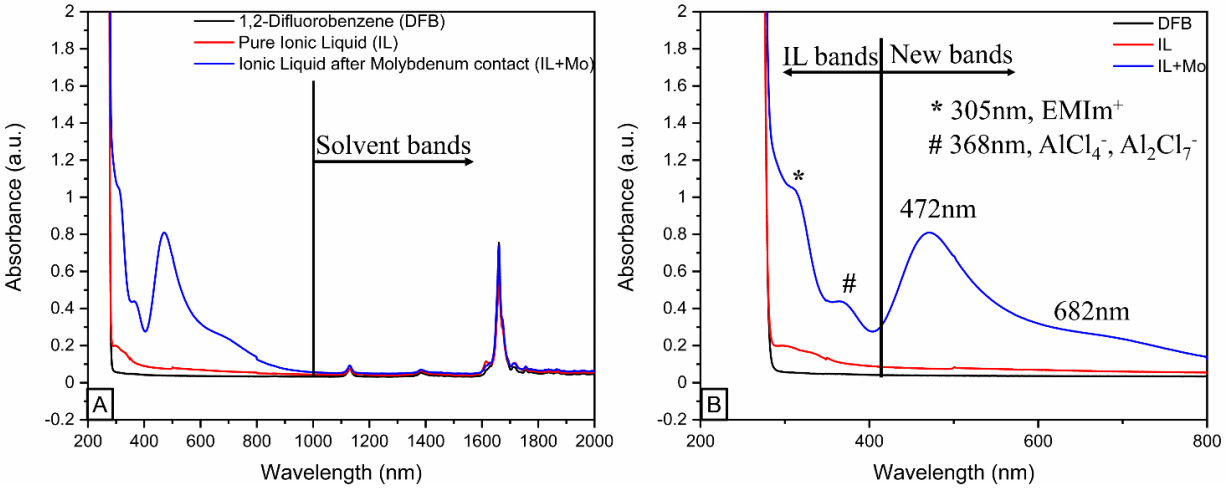

Figure 8 Ultraviolet-Visible (UV-VIS) spectra (A) of the whole wavelength range (200-2000 nm), and (B) in the range of 200-800 nm with occurring bands of the ionic liquid, marked with an asterisk (*); hash (#) and newly arising bands. Reprinted from Journal of Power Sources Vol. 633 by E. Zemlyanushin *et al*. Copyright 2025 by Elsevier [38].

It was not possible to obtain two bands for the pure ionic liquid electrolyte (**Fig. 8 A** and **B**, red line). Three reasons can be given for these bad signals, which are supposed to occur at 305 nm and 368 nm [113]. First of all, the samples were oversaturated. Secondly, the measurements have been done at room temperature. At elevated temperature, absorbance and splitting would be favored. Thirdly, $EMIm^+$, $AlCl_4^-$ and $Al_2Cl_7^-$ have a lack of UV-VIS active chromophores. Lang *et al.* [113] demonstrated that a concentration of 6.8 $mM \cdot L^{-1}$ of $AlCl_3$:EMImCl (2:1), diluted with dichloro methane (CH_2Cl_2) and the UV-VIS spectra will result in a sufficient splitting of the IL bands with relatively high absorbance at a temperature in the range of 40°C-100°C. After the reaction of the Mo with the ionic liquid (**Fig. 8 B**, blue line), a new Mo-$AlCl_3$-EMImCl related band at 472 nm (blue wavelength area) and a shoulder around 682 nm (red wavelength area) appear. Hartmann and Schmidt [114] reported similar results of absorption spectroscopy of molybdenum(III)-chlorides in acidic solutions. In addition, Scheffler *et al.* [115] published comparable results of solvated Mo^{3+} and Mo^{4+} chloro complexes in $AlCl_3$:EMImCl (1.3:1) ionic liquid environment. Therefore, it is expected that the dissolution of the Mo metal in the Lewis acidic electrolyte leads to the formation of Mo^{3+} and Mo^{4+} chloro complexes. It was possible to prove *via* ICP-OES, UV-VIS and temperature-dependent magnetic susceptibility measurements, that the instability of metallic Mo in Lewis acidic $AlCl_3$:EMImCl ionic liquid electrolyte leads to the dissolution of Mo. This finding raises the question to what extent the Mo instability influences electrochemical measurements.

Chen *et al.* [35] describe the electrochemical oxidation of Mo to be similar to platinum (Pt), whereby both metals show an onset oxidation peak at 1.8 V (*vs.* Al), measured *via* linear sweep voltammetry (LSV) with an $AlCl_3$-EMImCl (1.3:1) electrolyte. A similar activity of Mo has been reported by Yu *et al.* [104]. By running cyclic voltammetry (CV) measurements, the oxidation of Mo at 1.85 V and 1.98 V (*vs.* Al) could be recorded with an $AlCl_3$:BMImCl (1-butyl-3-methylimidazolium chloride) electrolyte in the molar ratio 1.6:1 [105]. However, Yu *et al.* [104] explain the reactivity of Mo to be negligible, compared to the contribution from the Graphite positive electrode. Nevertheless, while evaluating the electrochemical activity of novel promising materials, the redox reactions and related specific capacity may be misled by the Mo side-reaction with the Lewis acidic electrolyte. Moreover, to prove the stability of Mo, most reported investigations show only one LSV or one CV cycle, without considering a possible activation of the system, which may take several cycles [24]. Therefore, a cyclic voltammogram of pure Mo-foil (**Fig. 9 A**) and ball-milled Co_3O_4 coated on a Mo-foil (**Fig. 9 B**) at a scan rate of 0.5 $mV \cdot s^{-1}$ have been recorded against an Al anode. Co_3O_4 has been chosen because Liu *et al.* [105] reported this material to be an excellent positive electrode material for RABs, with an initial discharge capacity of 490 $mAh \cdot g^{-1}$ at a current density of 50 $mA \cdot g^{-1}$.

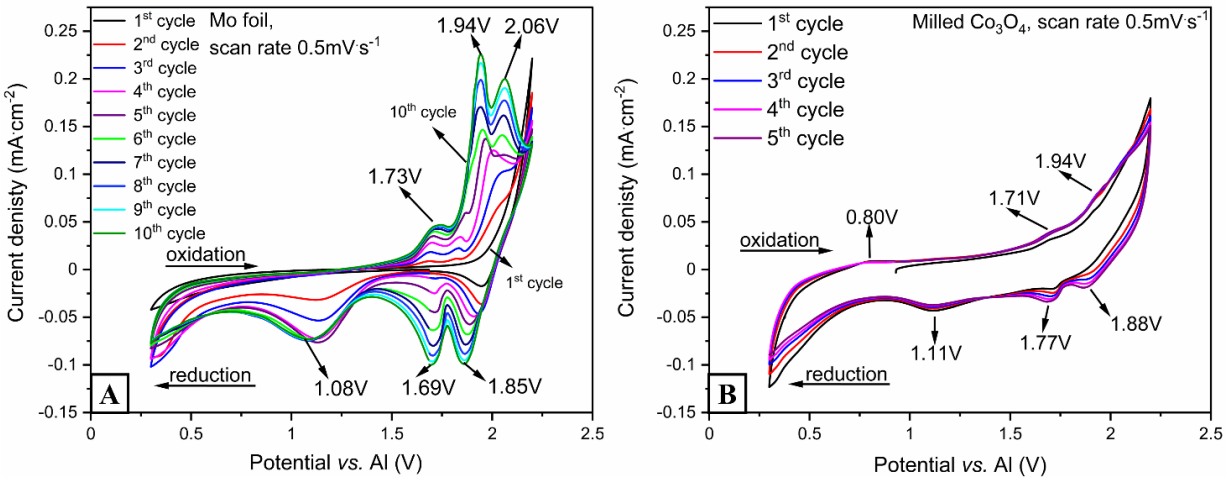

Figure 9 Cyclic voltammograms (CVs) of pure Mo-foil (A) and milled Co_3O_4 (B) that was coated on a Mo-foil at a scan rate of 0.5 $mV \cdot s^{-1}$ in a potential window of 0.3 V to 2.2 V. Reprinted from Journal of Power Sources Vol. 633 by E. Zemlyanushin *et al*. Copyright 2025 by Elsevier [38].

Both CVs, with and without Co_3O_4 material on the Mo-foil, show similar redox peak positions. Pure Mo-foil (**Fig. 9 A**) shows three reversible oxidation (1.73 V, 1.94 V and 2.06 V) and reduction (1.85 V, 1.69 V and 1.08 V) peaks, whose intensity increases with an increasing number of cycles. The redox activity recorded on the Mo-foil has a predominant influence on

the electrochemical signature and the rising current density is due to the longer reaction time. Co_3O_4 coated on Mo-foil (**Fig. 9 B**) shows redox activity at the same potentials and an additional small oxidation peak around 0.80 V, which belongs to the oxidation of the Co-based spinel and is comparable with the results of Liu *et al.* [105]. Certainly, the redox activity of the Co_3O_4 material is rather small. The intensity of the Mo peaks in **Figure 9 B** are lower because of the "protective" layer of coated quasi-inactive Co_3O_4. The reactive surface area of Mo is much more reduced compared with that of the pure Mo-foil. Since the dissolution of Mo takes place already after the contact with the electrolyte, it can be assumed that the previous $AlCl_4^-$, $Al_2Cl_7^-$, $EMIm^+$ compounds are not anymore responsible for the occurrence of redox activity, but newly formed Mo cation-based complexes or clusters in combination with the IL. Yu *et al.* [104] describe the identical redox behaviour of the Mo-foil current collector but report the redox activity would be negligible. Similar results, like those obtained by Yu *et al.* [104] and shown in this thesis, were published by Sun *et al.* [116], who describe the redox behaviour just to be an interface reaction between Mo and the electrolyte. However, a solid-liquid interface reaction does not lead to the dissolution of the electrode, like it is shown with Mo-$AlCl_3$-EMImCl. Such instabilities of metallic cell parts can lead to significant false discharge capacities from 150 $mAh \cdot g^{-1}$ to 400 $mAh \cdot g^{-1}$ and can be misleading when characterising novel electrode materials [117]. To prove the specific capacity contribution from molybdenum side-reactions, galvanostatic cycling with potential limitation (GCPL) has been done with Mo powder, coated on a tungsten (W) current collector. Tungsten has been chosen as the current collector because it is considered stable in IL electrolytes [12]. **Figure 10 A** shows the GCPL of Mo powder at a current density of 20 $mA \cdot g^{-1}$ in the potential window from 0.3 V to 2.2 V and **Figure 10 B** shows the corresponding coulombic efficiency of the charge (blue)/discharge (red) curves.

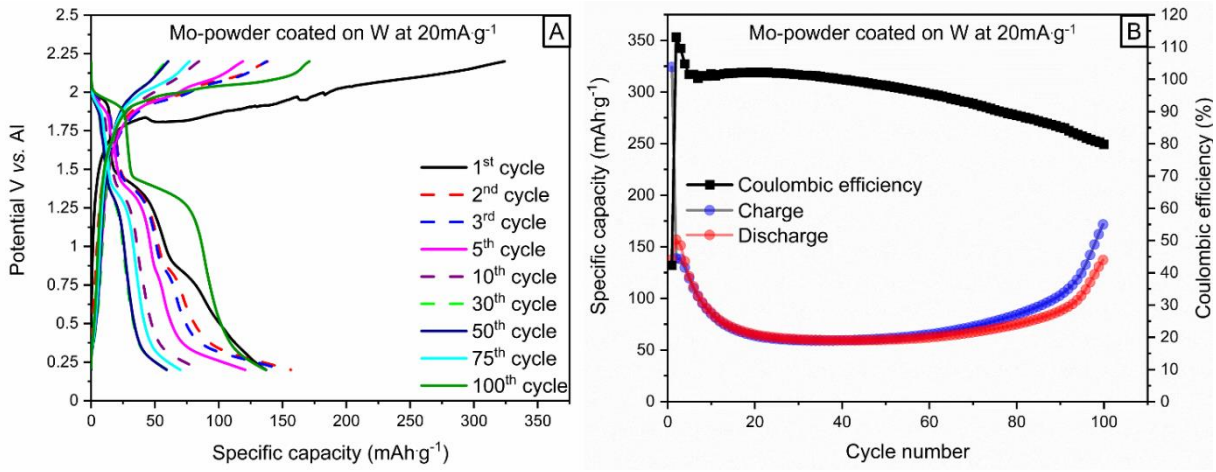

Figure 10 Galvanostatic cycling with potential limitation (GCPL) of Mo powder coated on W-foil in the potential window 0.3 V-2.2 V at a current density of 20 $mA \cdot g^{-1}$ (A) and the corresponding charge/discharge graph, including the coulombic efficiency (B). Reprinted from Journal of Power Sources Vol. 633 by E. Zemlyanushin *et al*. Copyright 2025 by Elsevier [38].

During the first charge cycle (**Fig. 10 A**, black curve), a long oxidation plateau occurs around 1.75 V, which corresponds to the first oxidation peak in the CV of the Mo-foil. Due to parasitic side-reactions, the potential shows instability until it reaches the upper limit of 2.2 V. Especially during the first 10 cycles, the influence of the side-reactions seems to have the biggest influence on the electrochemical performance. An indication of this assumption is that the coulombic efficiency is above 100% (**Fig. 10 B**) and falls below 100% after 40 cycles. For a certain time, the Mo powder cell delivers a relatively stable discharge capacity of ~60 $mAh \cdot g^{-1}$ before the capacity starts to increase again to reach a discharge capacity of ~136 $mAh \cdot g^{-1}$ at a current density of 20 $mA \cdot g^{-1}$ after 100 cycles. It is also worth mentioning that the GCPL measurement of the Mo powder collapses after 125 cycles. In total, the capacity increase over cycling and the evolution of the CE could be due to the following processes occurring in three steps; (I) The initiation of the parasitic side-reaction between Mo and the $AlCl_3$:EMImCl (1.5:1) ionic liquid electrolyte during the first 10 cycles. During the initial cycles, most possible side- and activation reactions occur and lead to a CE >100%. (II) Until the 40th cycle, charge and discharge are in a steady-state (ss) process with a stable CE. (III) After the 40th cycle, side-reactions are more pronounced during the oxidation/corrosion/dissolution process at the positive electrode causing a continuous decrease of the CE. It is assumed that after the second stage, the dissolution of Mo becomes the main reaction, providing more Mo-based redox active species. Diem *et al.* [118] obtained similar results for the dissolution of copper (Cu) in $AlCl_3$:EMImCl (1.5:1) ionic liquid electrolyte. Based on the Mo-$AlCl_3$-EMImCl results, an

additional indication of the proposed Mo-chloro complexes is the similarity with a tellurium (Te) metal system, which got dissolved in $AlCl_3$:EMImCl (1.3:1) ionic liquid electrolyte [98]. After adding Te powder to the $AlCl_3$-based electrolyte, Zhang *et al.* [98] describe the formation of AlTeCl and $TeCl_3{\cdot}AlCl_4$, which resulted in a color change of the ionic liquid from light-yellow to red-brown. Furthermore, a dissolution and electrochemical redox cycle for the metallic Te positive electrode has been proposed, leading to Te(II^-) and Te(IV^+) formation out of metallic Te [98]. The high redox ability of Te in a Lewis acidic ionic liquid electrolyte leads to the formation of an active tellurium chloroaluminate compound which delivers an initial discharge capacity of ~1026 $mAh{\cdot}g^{-1}$ at a current density of 0.5 $A{\cdot}g^{-1}$ [98]. Since molybdenum can reach the same oxidation states (II^- to VI^+) as tellurium, it is expected that the performance of both metals can be compared. An indication of the similarity concerning the dissolution characteristics between Mo and Te can be seen from the obtained X-ray photoelectron spectroscopy (XPS) results (**Fig. 11 B**). Since Mo gets dissolved and interacts with the ionic liquid electrolyte, a shuttle-effect of Mo-ions to the cycled aluminum negative electrode occurs. A similar migration effect has been reported by Reed *et al.* [119] in the case of using a current collector and cell body made of SS. As an explanation, it is mentioned that formed $FeCl_2$ and $CrCl_2$ can undergo a reduction reaction with Al and $AlCl_4^-$ (**Chapter 4.1**, **Eq. 11** and **12**), which results in iron and chromium metals. **Figure 11 A** shows the XPS survey of pure Al negative electrode. Besides the typical Al 2p and O 1s (and Al-O) signals, a Cl $2p_3$ peak is visible due to the chlorine-containing environment inside the Glovebox caused by the $AlCl_3$:EMImCl electrolyte. However, no Mo signals in the region from around 236 to 230 eV (**Fig. 11 A**) can be detected. **Figure 11 B** shows the XPS spectra of Mo^{4+}, Mo^{5+} and Mo^{6+} on an Al negative electrode stopped after complete discharge at 0.3 V. After fitting, peaks at (VI: Mo^{6+} $3d_{3/2}$) 235.68 eV, (IV: Mo^{5+} $3d_{3/2}$) 234.18 eV, (II: Mo^{4+} $3d_{3/2}$) 233.48 eV, (V: Mo^{6+} $3d_{5/2}$) 232.68 eV, (III: Mo^{5+} $3d_{5/2}$) 230.78 eV and (I: Mo^{4+} $3d_{5/2}$) 230.18 eV are obtained, which can be assigned to the oxidations states of Mo^{4+} (purple peaks), Mo^{5+} (yellow peaks), and Mo^{6+} (green peaks). However, metallic Mo is not present since the Mo $3d_{5/2}$ electron binding energy at 228 eV is missing. The oxidation states of Mo probably belong to several kinds of Mo-O layers. An indication for this assumption is that the two peaks at lower binding energies are symmetrical, while the peaks appear asymmetrical in the case of Mo metal.

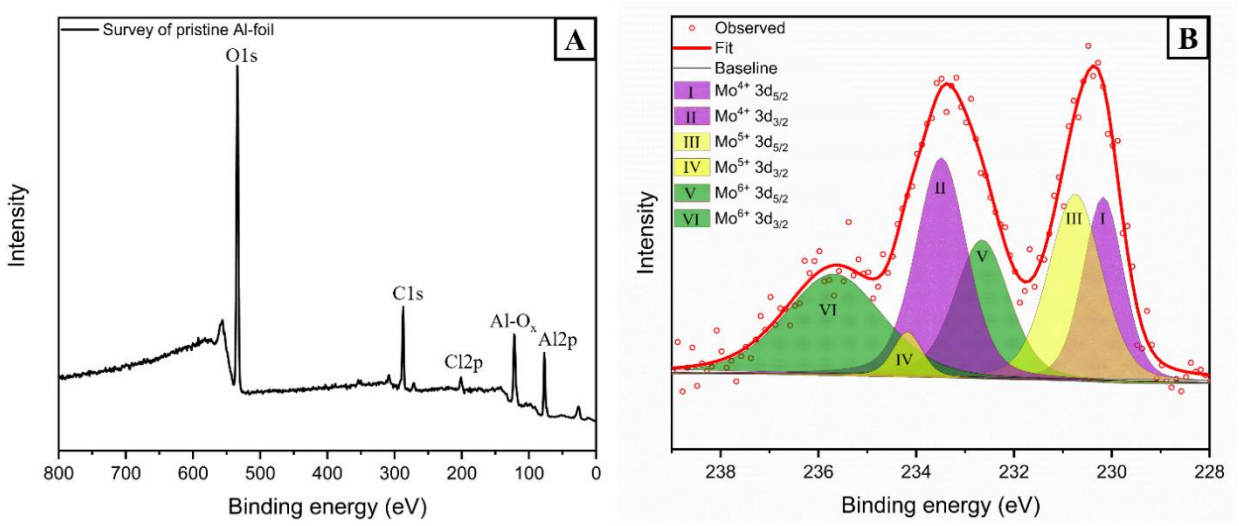

Figure 11 X-ray photoelectron spectroscopy **(**XPS) survey of pristine Al-foil (A) and XPS spectra of $Mo^{4+/5+/6+}$ cations on Al-foil (B) stopped at 0.3 V. Reprinted from Journal of Power Sources Vol. 633 by E. Zemlyanushin *et al*. Copyright 2025 by Elsevier [38].

Since the peaks with binding energies at 235.68 and 232.68 eV are characteristic for MoO_3 [120], it is assumed that this Mo-oxide has formed. A similar formation of a metal oxide layer has been reported for metallic Ni current collector used in an $AlCl_3$:EMImCl (1.3:1) electrolyte RAB system [103]. It has been shown that Ni used as a current collector forms an oxide layer consisting of NiO and Ni_2O_3 [103] as well and can, therefore, be compared with the Mo system. In contrast to the Mo-$AlCl_3$-EMImCl results of the UV-VIS spectroscopy, it was not possible to detect the Mo^{3+} oxidation state, *via* XPS. A reasonable explanation could be that the proposed Mo^{3+}-chloro compound is only stable in ionic liquid electrolytes. If Mo – Cl_x^{n-} compounds are formed during the reaction between Mo and $AlCl_4^-/Al_2Cl_7^-$, these Mo-compounds can perform a hydrolysis and oxidation reaction [121] after removing the sample from the electrolyte. Even a small amount of H_2O can initiate an oxidation of Mo^{3+}, resulting in higher Mo^{x+} (x = 4, 5, 6) oxidation states. Based on the obtained UV-VIS (**Fig. 8 A** and **B**) and XPS (**Fig. 11 B**) results and in comparison to Al-Te battery system [98,101], a potential two-step working mechanism of the *in-situ* occurring Mo current collector dissolution and complex formation is proposed (**Figure 12**).

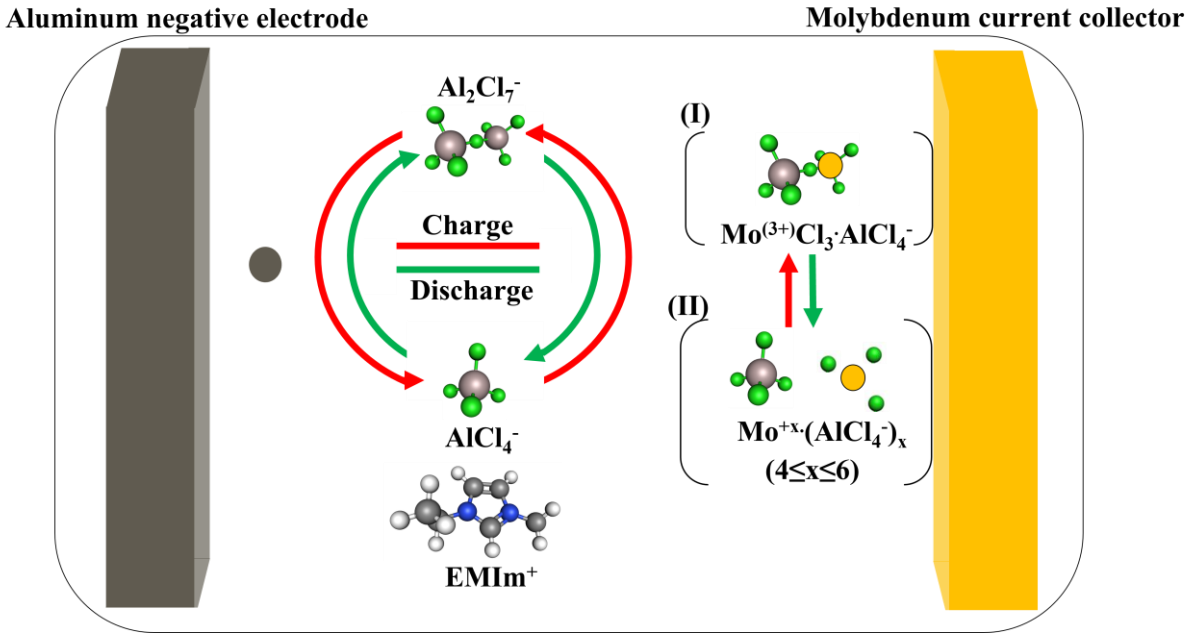

Figure 12 Schematic illustration of the proposed *in-situ* dissolution and complex formation of the Mo current collector in Lewis acidic $AlCl_3$:EMImCl (1.5:1) ionic liquid electrolyte.

During charge process (I) the oxidation reaction between the metallic Mo current collector and the $AlCl_4^-$ takes place and leads to the formation of $Mo^{(3+)}Cl_3{\cdot}AlCl_4^-$ complex. This Mo^{3+} species is only stable in an ionic liquid environment due to the interaction of one of the chloride atoms from $AlCl_4^-$. However, during discharge (II) the bond between the Mo^{3+} and $AlCl_4^-$ get interrupted and thereby enables the oxidation of Mo^{3+} to higher states (4^+,5^+ and 6^+) connected with the release of electrons. By this, the shuttle-effect of $Mo^{4+/5+/6+}$ towards the Al negative electrode becomes reasonable. Moreover, it seems that the initiated parasitic side-reaction for the formation of $Mo^{(3+)}Cl{\cdot}AlCl_4^-$ is the reaction-determining step. As it is visible in the GCPL measurement (**Fig. 10 A** and **B**), initially, the specific capacity drops and stabilizes for a certain time when the redox reactions between Mo^{3+} and $Mo^{4+/5+/6+}$ are in a steady-state situation. Nevertheless, before reaching the peak point of the reaction-determining step, the charge/discharge capacities start to increase before the cell collapses.

In order to obtain a stable current collector, a 30 µm thick gold colored TiN layer has been coated on SS-(72 µm thickness) and Cu-foil (42 µm thickness) *via* magnetron sputtering technique [122]. The sputtering was made by Dr. Michael Stüber and apl. Prof. Sven Ulrich from the Institute for Applied Materials – Applied Materials Physics (IAM-AWP) at the Karlsruhe Institute of Technology (KIT). For clarity and simplified explanations, in the following, the SS and Cu with TiN sputtered substrates will be called TiN@SS and TiN@Cu, respectively. Wang *et al.* [12] reported the successful sputtering of TiN@SS and TiN@PI (polyimide) with

high stability against the most Lewis acidity $AlCl_3$:EMImCl (2:1) ionic liquid electrolyte. However, the performed sputtering of TiN@SS at KIT failed because it was impossible to fix and tighten the SS-foil into the substrate holder to get a smooth and flat surface for the sputtering. **Figure 13 A** shows the unsuccessful coated TiN@SS foil, whereby some unevenness and irregularities on the surface are marked with a red circle. The relatively high thickness of the SS made the foil very robust and hard, therefore, it was impossible to achieve a flat surface by polishing. In **Figure 13 A** it can be seen that the sputtering took place only in certain spots, which indicates the high impact of the substrate surface [123].

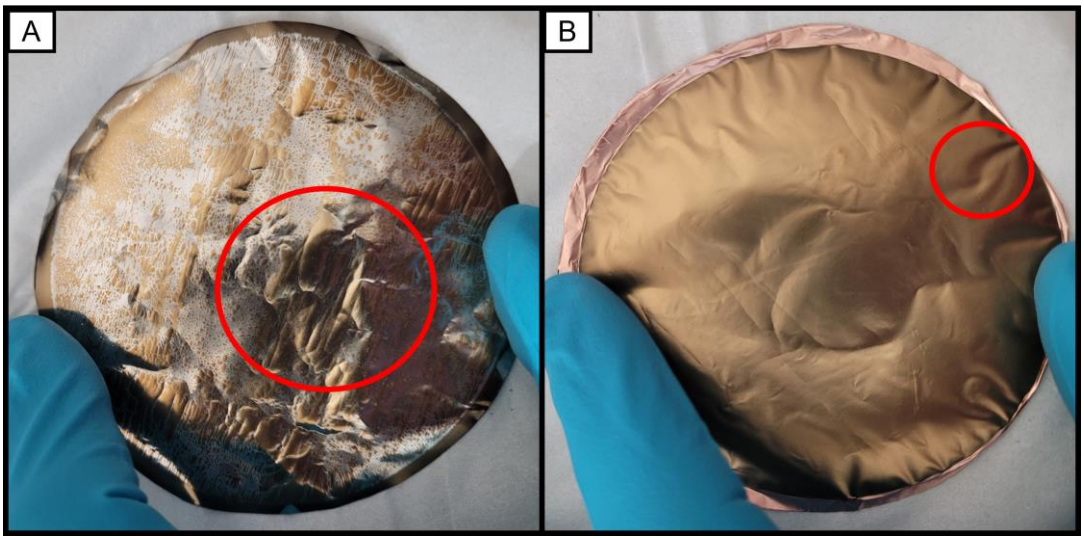

Figure 13 (A) Failed magetron sputtered titanium nitride on stainless steel (TiN@SS) foil and (B) successfully prepared titanium nitride on copper (TiN@Cu) foil.

Nevertheless, the coating of TiN@Cu (**Fig. 13 B**) was successful even if the TiN layer is under high tension (marked with a red circle), which results in an arched/curved foil. Further investigations have been done only with the TiN@Cu foil. X-ray diffraction (XRD) pattern of the sputtered TiN@Cu foil is shown in **Figure 14 A**. All reflections (111, 200, 220, 311 and 222) indicate a pure cubic TiN structure without any impurities and are consistent with the literature (JCPDS 38-1420). Scanning electron microscopy (SEM) and energy-dispersive X-ray (EDX) images (**Fig. 14 B1-D3**) confirm the formation of a multilayer of TiN@Cu with a heterogenous distribution of Ti- and N-atoms.

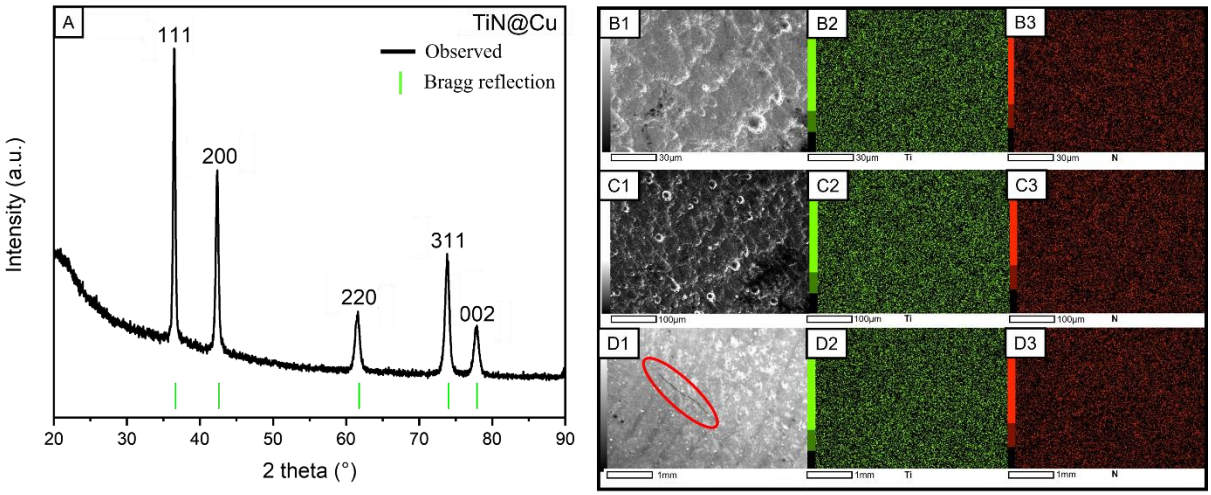

Figure 14 (A) X-ray diffraction (XRD) pattern of TiN@Cu measured with a Cu Kα 1.5406 Å X-ray source. (B) Scanning electron microscopy (SEM) and energy-dispersive X-ray (EDX) images of TiN@Cu at a zoom of 30 µm (B1-B3), 100 µm (C1-C3) and 1 mm (D1-D3), respectively. All measurements were done at Chiba University, Japan.

However, some cracks (**Fig. 14 D1**, marked with a red circle) are visible on the TiN@Cu surface. It is assumed that the cracks are formed during unrolling the high-tension arched/curved foil to punch out discs (1.131 cm^2) for the XRD, SEM and EDX investigations. The main idea and difference to the work of Wang *et al.* [12] is to obtain a freestanding TiN foil by dissolving the Cu (and SS) substrate. First of all, chemical etching with concentrated (conc. 32%) and diluted (10%) hydrochloric acid (HCl) has been done. It was impossible to dissolve the copper from the TiN@Cu foil with diluted HCl, while conc. HCl removed the entire metal (**Eq. 14**). However, the remaining TiN is brittle and crumbles into small pieces. The assumption is that due to the strong acidity of conc. HCl, the dissolution takes place very fast and the TiN suffers from the high tension which leads to the breakage of the foil. With a slower dissolution rate, TiN could erase and stay in a stable shape.

$$Cu + 2HCl_{(conc.)} \rightarrow H_2 + CuCl_2 \qquad (14)$$

Therefore, a mixture of diluted HCl (5 ml) with the addition of 0.1 $mol \cdot L^{-1}$ iron(III)-chloride hexahydrate ($FeCl_3$ x $6H_2O$) (135.15 mg, 0.50 mmol) powder was prepared. Iron ions in a

chloride solution environment are well known to dissolve metallic Cu [124]. The corresponding reactions between Cu and Fe^{3+} are shown in **Equation 15-19**.

$$2Fe^{3+} + Cu \rightarrow Cu^{2+} + 2Fe^{2+} \quad (15)$$

$$Cu^{2+} + Cu \rightarrow 2Cu^{+} \quad (16)$$

$$Cu^{+} + Fe^{3+} \rightarrow Cu^{2+} + Fe^{2+} \quad (17)$$

$$Cu^{+} + nCl^{-} \rightarrow CuCl_n^{(n-1)-} \quad (18)$$

$$CuCl_n^{(n-1)-} + Fe^{3+} \rightarrow Cu^{2+} + Fe^{2+}\, nCl^{-} \quad (19)$$

The dissolution of Cu in an $HCl/FeCl_3$ solution was successful, but the same crumble effect of the TiN appeared. Based on the recommendation of Dr. Toshihiko Mandai (National Institute for Materials Science (NIMS), Japan), the removal of Cu has been done *via* electrolysis. In a glass cell with 0.5 $mol \cdot L^{-1}$ copper(II)-sulfate pentahydrate ($CuSO_4$ x $5H_2O$) (12.48 g, 49.98 mmol) solution (V=100 ml), the TiN@Cu foil (1.131 cm^2) was used as the positive electrode and a pure copper wire as the negative electrode. The electrolysis was done at a constant current density of 80 $mA \cdot cm^{-2}$ for 3 hours. Just like with attempts to remove the Cu by chemical etching, the TiN was becoming brittle after electrolysis and, therefore, not suitable for further investigations. All trials (chemical and electrochemical) to obtain a freestanding TiN foil are summarized as a flow chart in **Figure 15 A**. Nevertheless, Graphite powder was coated on the TiN@Cu current collector to run CV measurements to investigate the influence of the Cu substrate. Due to the high tension, it was impossible to fix the foil to obtain a smooth and flat surface to run a coating. As a result, the distribution of the slurry became non-homogeneous, which led to different active masses on all punched positive electrodes.

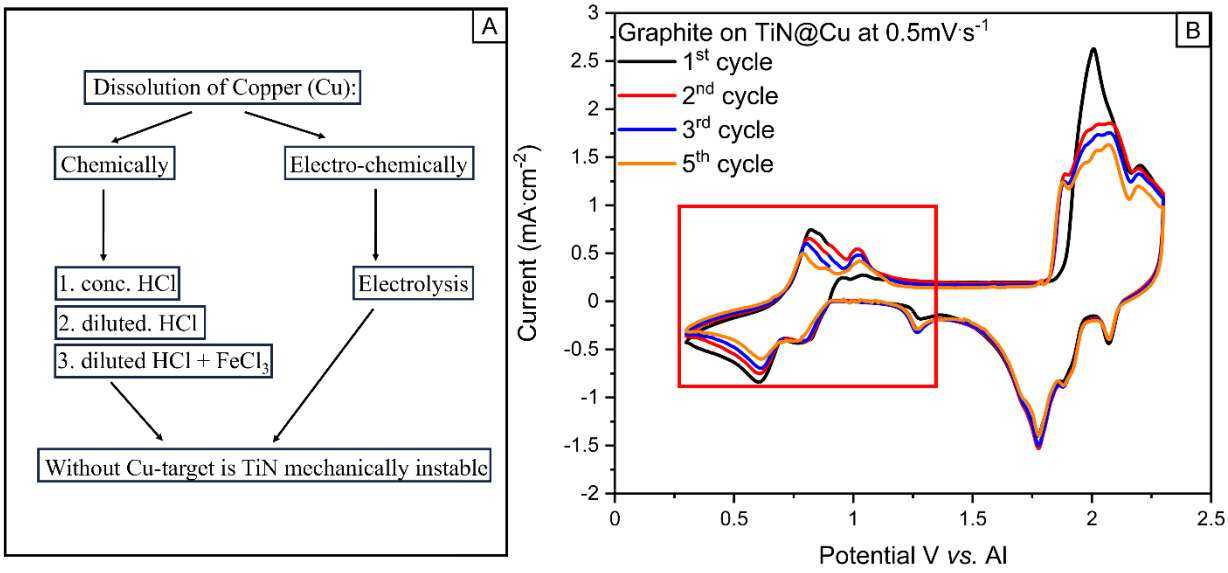

Figure 15 (A) Flow chart of chemical and electrochemical attempts to remove the Cu of the TiN@Cu to obtain a freestanding TiN foil. (B) Cyclic voltammogram (CV) of Graphite, coated on TiN@Cu foil in an $AlCl_3$:EMImCl (1.5:1) ionic liquid electrolyte at a scan rate of 0.5 $mV \cdot s^{-1}$.

In **Figure 15 B**, the redox contribution of metallic Cu in $AlCl_3$:EMImCl (1.5:1) ionic liquid electrolyte at a scan rate of 0.5 $mV \cdot s^{-1}$ is marked with a red rectangle. It has been proven that magnetron sputtering on only one side of the Cu-foil is not sufficient to hinder the oxidation of Cu by $AlCl_4^-/Al_2Cl_7^-$. Even small uncovert Cu surface areas are enough to obtain reversible redox reactions [118]. Usually, side-reactions and dissolutions of metallic parts, organic binder-or positive electrode host materials are not initiated by $AlCl_4^-$ but by the much more Lewis acidic $Al_2Cl_7^-$ [125]. In fact, Cu-foil can be oxidized in basic [125,126], neutral [126,127] and acidic [125,126] ionic liquid electrolytes. Therefore, the low resistance of Cu towards all formed Al-Cl complexes and chloride anions [112] at all possible molar ratios (**Chapter 2.4.3**, **Eq. 3-8**) results in the anodic dissolution of Cu and the formation of active Cu^+/Cu^{2+} redox couples.

To sum up, several observations clearly indicate that the molybdenum, used as the current collector, is unstable and undergoes a reaction with the $AlCl_3$:EMImCl (1.5:1) ionic liquid electrolyte. One indication of a dissolution and complex formation is the change of the electrolyte colour from colourless/yellowish to red after getting in touch with a Mo source. UV-VIS measurements of the red Mo-$AlCl_3$-EMImCl ionic liquid show newly occurring non-electrolyte-related bands, which usually appear for Mo^{3+} and Mo^{4+} ions. Moreover, in comparison to the fresh mixed ionic liquid, the electrolyte after reacting with Mo exhibits Langevin-type paramagnetism from localized magnetic moments as present in Mo-complexes

or also -oxides, for instance, whereas metallic Mo would only exhibit temperature-independent Pauli paramagnetism. ICP-OES tests confirm a dissolution of Mo of 1.99±0.06 w(%) in 5 mg ionic liquid electrolyte. Cyclic voltammograms were recorded to understand the effect of Mo on the electrochemical reaction with $AlCl_3$-EMImCl electrolyte. Oxidation peaks around 1.73 V, 1.94 V and 2.06 V as well as reduction peaks at 1.85 V, 1.69 V and 1.08 V, confirm that reversible reactions take place on the Mo electrode surface similar to Pt [35]. It is important to stress that, in the literature, the impact of Mo in $AlCl_3$-based RABs is described to be negligible [104]. Instead, according to the results of this thesis, the entire capacity of ~136 $mAh \cdot g^{-1}$ at a current density of 20 $mA \cdot g^{-1}$ after 100 cycles, is due to the Mo side-reactions. Furthermore, *via* XPS measurements it was possible to show that three different oxidation states of Mo^{x+} (x = 4,5,6) exist on the Al negative electrode after running electrochemical tests. The Mo dissolves partly in the ionic liquid and shuttles to the anode. Mo^{3+} is supposed to be stable only in $AlCl_3$-based ionic liquid electrolyte. Based on all shown results, it is assumed that Mo reacts similarly to tellurium and nickel to form Mo – Cl_x^{n-} and/or $MoOCl_x^{n-}$complexes with $AlCl_4^-$. Furthermore, all efforts to obtain a freestanding TiN CC were unsuccessful due to the low stability of the 30 µm magnetron sputtered TiN without the Cu substrate. TiN@Cu cannot be used as a CC because Cu-foil forms in a basic, neutral and acidic IL electrolyte active Cu^+/Cu^{2+} redox couple.

4.3 Conclusion

All results suggest that the Mo current collector suffers from side-reactions. The assumption that molybdenum shows redox activity due to residual water in the ionic liquid electrolyte as reported in literature, could be discarded according to the results obtained in this thesis. The electrochemical oxidation of unstable metals can lead to significant false discharge capacities from 150 $mAh \cdot g^{-1}$ to 400 $mAh \cdot g^{-1}$ and be misleading when characterizing novel electrode materials. Therefore, using Mo as a current collector and cell housing should be avoided. Instead, anodic stable materials like carbon paper, glassy carbon, TiN, or ITO should be used for $AlCl_3$:EMImCl ionic liquid-based RABs.

4.4 Outlook and Future Work

After careful investigation of the dissolution and redox activity of the Mo current collector, all Mo sources inside the cells were replaced by stable materials. Further measurements are done with a carbon paper current collector and W-pistons to close the PFA Swagelok cells. For scientific purposes on a laboratory scale, the use of W-pistons is fine but not suitable for

upscaled applications. Tungsten has two major disadvantages compared to Mo: (I) Tungsten is more expensive than Mo [128] and (II) has nearly a two times higher intrinsic density of ~19.34 $g \cdot cm^{-3}$ (Mo = ~10.23 $g \cdot cm^{-3}$). Theoretically, W can be used as a current collector as well, however, the large intrinsic density will result in a high ratio difference between non-active and active compounds and reduce the effective energy density of the positive electrode [35]. One approach to keep the Mo current collector and pistons could be to prohibit the shuttling of the newly formed Mo-species between the positive and negative electrodes and prevent those redox activities. The Mo-complexes could be intercepted by modifying the separators. For instance, Zhang *et al.* [98] prepared an Al-Te (tellurium) battery, which suffered from the dissolution of Te in contact with the Lewis acidic $AlCl_3$:EMImCl (1.3:1) ionic liquid electrolyte. To prevent the shuttle-effect of formed Te-complexes, the separator was modified with single-walled carbon nanotubes (SWCNTs). Since SWCNTs are able to adsorb generated tellurium chloroaluminate compounds, the same could happen with Mo-Cl ions. A similar strategy has been applied to Al-Ni batteries by Wu *et al.* [129]. Instead of catching the shuttling species, the separator was modified with a kind of scavenger to hinder unwanted side-reactions (alloying) on the Al negative electrode. The alloying process is initiated by the formation of nickel(II)-chloride ($NiCl_2$) due to the reaction between the Ni-positive electrode and the $AlCl_3$:EMImCl (1.3:1) ionic liquid electrolyte (**Chapter 4.1**, **Eq. 13**). Wu *et al.* [129] prepared an Al-powder interlayer between two separators, which reacts with dissolved Ni^{2+} ions (**Eq. 20**).

$$2Al + 3Ni^{2+} \rightarrow 2Al^{3+} + 3Ni \qquad (20)$$

However, the newly formed Ni metal between the separators should continuously further react with the ionic liquid electrolyte. The strategy to use a scavenger will probably only remain successful until the Al-powder is completely exchanged by Ni. Moreover, the formation of sharp Ni dendrites could penetrate the separators and cause a short circuit. Therefore, the safer method to avoid shuttling of dissolved Te, Ni or Mo species seems to be to modify the separators with a catching material.

5. Reactivity of Binder materials

5.1 Introduction: Impact of Polyvinylidene fluoride (PVdF) in RABs

So far, polyvinylidene fluoride (PVdF) is the most widely used binder material for cathodes in Lithium-Ion Batteries (LIBs) [130]. The following properties of the fluoropolymer make it almost indispensable as a battery component: Thermal stability, mechanical strength and chemical resistance. PVdF does not show any reactions in contact with acids, bases, aromatic solvents and oxidizing agents [131,132]. However, strong bases and organic amines initiate a gradual dehydrofluorination (DHF), which leads to the formation of hydrofluoric acid (HF) and sp^2-hybridized carbon-carbon double bonds in the polymer chain [131,133]. In the case of the usage of PVdF as a binder material for the positive electrodes in Rechargeable Aluminum-Batteries (RABs), several authors report a visible side-reaction between the aluminum chloride ($AlCl_3$) / 1-ethyl-3-methylimidazolium chloride (EMImCl)-based ionic liquid (IL) and the polymer [14,30,134]. It is possible to see with the naked eye that the mix of the white PVdF powder and the colourless/yellowish electrolyte turns black very quickly (**Fig. 16**).

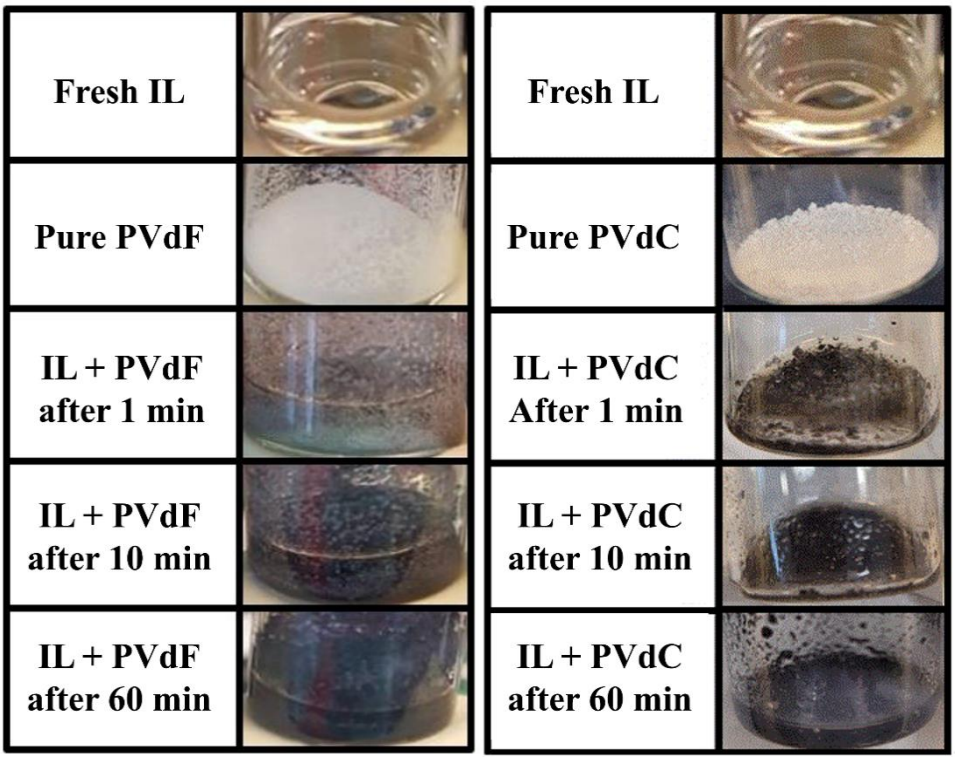

Figure 16 Reaction between polyvinylidene fluoride (PVdF) and polyvinylidene chloride (PVdC) with Lewis acidic ionic liquid electrolyte after 1 min, 10 min and 60 min, respectively.

To date, only Chen *et al.* [35,135] mentioned the decomposition of the difluoromethylene ($-CF_2$) functional group of PVdF and described no effect on the performance of cobalt boride (CoB)

cathode material. Smajic *et al.* [14] reported similar results for reduced graphene oxide dried under supercritical conditions (RGOCPD) used as a positive electrode for RABs in ionic liquid electrolyte. A detaching/delamination effect of the active material from the current collector has been observed by Chen *et al.* [35] due to a swelling effect of PVdF in $AlCl_3$:EMImCl (1.3:1) electrolyte. In 2015 Wang *et al.* [30] reported that PVdF dissolves and partially reacts with the ionic liquid electrolyte which leads to a significant decrease in the electrochemical performance. Therefore, a new binder-free Ni-V_2O_5-based positive electrode was investigated [30]. It is worth mentioning that the used ionic liquid was made of $AlCl_3$ and 1-butyl-3-methylimidazolium chloride (BMImCl) in the molar ratio of 1.1:1. Nevertheless, both $AlCl_3$:EMImCl and $AlCl_3$:BMImCl electrolytes form the same two necessary complexes, $AlCl_4^-$ and $Al_2Cl_7^-$. Therefore, the interaction between the polymer binder and the $AlCl_4^-/Al_2Cl_7^-$ is the same. Yang *et al.* [32] reported a capacity decay of PVdF Graphite-based electrodes at 1000 $mA{\cdot}g^{-1}$ compared to the investigated sodium-alginate (Na-Alg) binder material. The dissolution and disappearance of $-CF_2$ groups is considered to be responsible for worse cyclability. In 2022, Yu *et al.* [31] utilized pencil-drawing graphite nanosheets (PGN) as the positive electrode and coated a protective PVdF layer on the surface of PGN. The idea was to enhance the cathode stability, during the volume expansion caused by the $AlCl_4^-$ intercalation. Rate capability tests of PGN with and without a PVdF layer show a huge difference. Without PVdF the initial cycle at 0.5 $A{\cdot}g^{-1}$ shows a specific discharge capacity of ~45 $mAh{\cdot}g^{-1}$, PGN with PVdF delivers a specific discharge capacity of ~72 $mAh{\cdot}g^{-1}$. The same trend of higher charge/discharge capacities was obtained at 1.0 $A{\cdot}g^{-1}$, 2.0 $A{\cdot}g^{-1}$ and 5.0 $A{\cdot}g^{-1}$. Two further effects need to be taken into account. With a layer of PVdF on the electrode, the charge and discharge capacities increased slightly with a further number of cycles at all current densities. As a result, after returning to the current density of 0.5 $A{\cdot}g^{-1}$, the PVdF layered electrode delivered ~94 $mAh{\cdot}g^{-1}$, while the PGN electrode without PVdF returned to the initial value. On the other hand, the same authors mention a dissolution of PVdF during the initial cycles. Yu *et al.* [33] were able to show the disappearance of $AlCl_4^-$ and $Al_2Cl_7^-$ bands of the IL electrolyte after adding 2.5 w(%) of PVdF *via* Raman spectroscopy. If the active electrolyte species get deactivated, the whole charge/discharge process will be disturbed. To sum up: In the case of using PVdF as a binder material in RABs, three different interpretations on the influence of occurring side-reactions are reported (**Table 3**). Firstly, the reaction between PVdF and the $AlCl_3$:EMImCl electrolyte has no negative impact. Secondly, the unwanted side-reaction and dissolution negatively influence the electrochemical performance. Thirdly, the use of PVdF

results in an increased specific capacity and higher electrode stability besides the dissolution of the binder material.

Table 3 Summary of mentioned effects of the reaction between PVdF and the $AlCl_3$:EMImCl (or $AlCl_3$:BMImCl) ionic liquid electrolytes in the literature. Checkmark (✓) symbolizes reported effect, while cross (✖) stands for not mentioned information.

Authors, Year of publication	Colour change	Dissolution	Compositional changes	Effect on electrochemistry	No effect on electrochemistry
L.L. Chen *et al.*[35,135], both **2020**	✖	✓	✓	✖	✓
J. Smajic *et al.* [14], **2019**	✓	✖	✖	✖	✓
Y. Uemura *et al.* [134], **2018**	✓	✖	✓	✖	✖
H. Wang *et al.* [30], **2015**	✓	✓	✖	✓ **(negative)**	✖
Z. Yang *et al.* [32], **2023**	✓	✓	✓	✓ **(negative)**	✖
J. Yu *et al.* [31], **2022**	✖	✓	✖	✓ **(positive)**	✖
Z. Yu *et al.* [33], **2023**	✓	✖	✓	✓ **(negative)**	✖

Despite these findings, the impact of PVdF instability on battery performance remains inconclusive due to conflicting research results and a lack of studies directly addressing its effects on the electrochemical performance of different electrode materials. Until now, no one has uncovered the possible side-reaction products of PVdF or been able to explain the change in powder and electrolyte colour. This chapter focuses on understanding the side-reaction mechanism of the binder material with the IL electrolyte in the standard and well-investigated Al-Graphite cell configuration. In addition, polyvinylidene chloride (PVdC) is tested under the same conditions to have a direct comparison and to possibly find an alternative for PVdF because the European Chemical Agency (ECHA) could decide to restrict the use of per- and polyfluoroalkyl substances (PFAS) by 2025 [15]. Furthermore, the idea is to use a chloride-based material to avoid halogen exchange reactions, the dissolution of the binder and the resulting detaching of active material from the current collector. Moreover, an alternative slightly Lewis

acidic electrolyte made of $AlCl_3$:Urea (1.07:1), in which the molar ratio of 1.07 was the minimum amount of $AlCl_3$ to get a fully dissolved and colourless electrolyte, was used to prove that $Al_2Cl_7^-$ is responsible for occurring side-reaction.

5.2 Results and Discussions

According to the literature, the side-reactions of the PVdF could be explained by two different approaches: First, the above-mentioned interaction with $Al_2Cl_7^-$ [30,136] or the influence of the EMImCl salt to achieve a phase transformation of a non-polar α-PVdF toward an electroactive, highly polar β-PVdF [137]. The phase transformation can occur because of the interaction of the positive charge of the imidazolium ring's nitrogen with the PVdF's fluoride atoms and the interaction of $AlCl_4^-$ anions with the PVdF`s hydrogen atoms. Both interactions lead to rearranging the F- and H-atoms of the PVdF as shown in **Figure 17**. This comparison has been done with a similar system based on the electrostatic interaction between PVdF, $EMIm^+$ and PF_6^- [138].

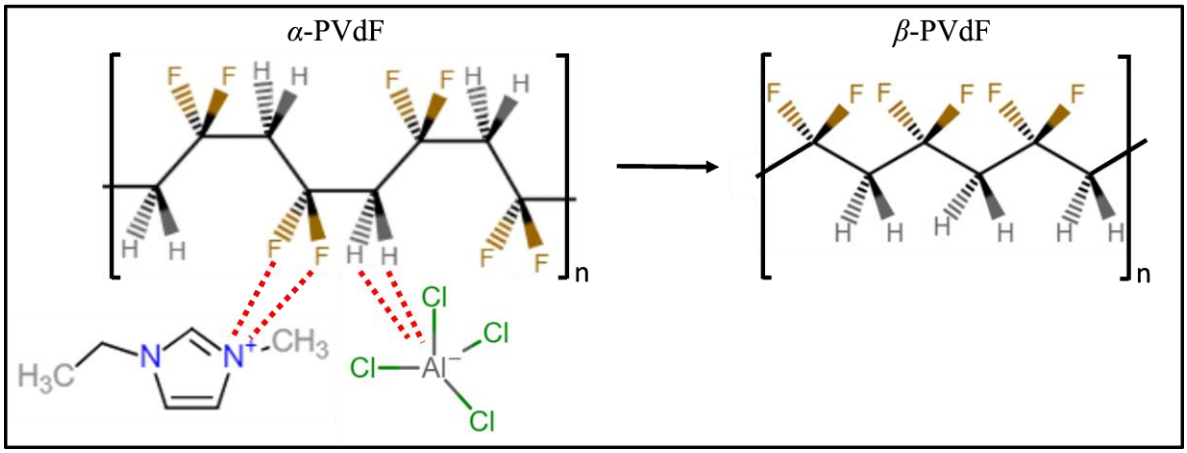

Figure 17 Schematic illustration of the phase transformation of α-PVdF into β-PVdF due to the interaction with $EMIm^+$ and $AlCl_4^-$. Reprinted from Journal of the Electrochemical Society Vol. 171 No. 11 by E. Zemlyanushin *et al*. Copyright 2024 by IOP Publishing [34].

To make sure which component of the ionic liquid is responsible for the side-reaction, including the colour change, the PVdF and PVdC binders were soaked in $AlCl_3$:Urea (1.07:1) electrolyte. The $AlCl_3$:Urea electrolyte does not contain any EMImCl but forms $Al_2Cl_7^-$ complex like it is shown in **Eq. 21-23** [69,139,140]. The ratio of 1.07:1 has been chosen because it is the first $Al_2Cl_7^-$-containing ratio which results in a completely dissolved clear electrolyte.

$$n(Urea) + AlCl_3 \rightleftharpoons [AlCl_2 \cdot (Urea)_n]^+ + AlCl_4^- \quad (21)$$

$$AlCl_4^- + AlCl_3 \rightleftharpoons Al_2Cl_7^- \quad (22)$$

$$Al_2Cl_7^- + AlCl_3 \rightleftharpoons Al_3Cl_{10}^- \quad (23)$$

In **Eq. 21**, *n* is the coordination number of Urea, which depends on the molar ratio between $AlCl_3$ and Urea. In the case of preparing a neutral system of $AlCl_3$:Urea (1:1), several $[AlCl_y \cdot Urea_w]^{u+}$ complexes are formed, but no $Al_2Cl_7^-$ is obtained (**Eq. 24**) [69,140,141].

$$4xAlCl_3 + 4xUrea \rightleftharpoons$$
$$xAlCl_4^- + y[AlCl_3 \cdot Urea] + x[AlCl_2 \cdot (Urea)_2]^+ + z[AlCl_3 \cdot (Urea)_2] \quad (24)$$

The values of *x*, *y* and *z* were determined to be 1, 2.49 and 0.03, respectively, for the species shown in **Eq. 24** [69]. Soaking tests show that both, PVdF and PVdC, change their colour from white and light brown to black, respectively, in $AlCl_3$:Urea (1.07:1). Since even the slightly Lewis acidic non-EMImCl containing electrolyte leads to the same colour change as the $AlCl_3$:EMImCl (1.5:1) ionic liquid, it is confirmed that the side-reactions and colour change are related to the $Al_2Cl_7^-$ complex. The same soaking test was done for PVdF and PVdC using the $AlCl_3$:EMImCl electrolyte and both polymers turned black (**Fig. 16**). To separate the liquid from the binder powders, a syringe filter was used. The residual ionic liquid was removed by washing the powders with 1,2-Difluorobenzene before drying at 60 °C under vacuum for 6 h. The residual dark compound was investigated without any further treatments. First, Fourier-transform infrared spectroscopy (FT-IR) measurements of the pristine PVdF and PVdC (**Fig. 18 A** and **B**) were performed and compared with soaked binders (**Fig. 18 C** and **D**). For easier demonstration of the results, the soaked materials are called s-PVdF and s-PVdC, while pristine polymer powders are labelled as p-PVdF and p-PVdC. In the case of p-PVdF, it was possible to assign all vibrational modes (**Table S2**) of α-PVdF (main-phase) and β-PVdF (side-phase) according to the literature [142,143]. The same analysis was done with the p-PVdC [144,145]. The FT-IR spectra confirm that p-PVdF has no impurities while p-PVdC shows unexpected additional bands at 1745 cm^{-1} and 1636 cm^{-1} (**Fig. 18 B**, marked with an asterisk). Both bands result from an unsaturated carbonyl (-C=O) impurity, which is also responsible for the yellowish/light brown colour of the usually colourless p-PVdC powder [146]. Two suitable explanations for this impurity can be given as follows: (I) During the synthesis of PVdC some

additives like plasticizers [147] are added and remain in the final product; (II) Chlorinated polymers like polyvinyl chloride (PVC) or PVdC are sensitive to run photooxidation reactions [148]. **Figure 18 C** and **D** show the FT-IR spectra of s-PVdF and s-PVdC after the reaction with the electrolyte. For comparison, possible products arising from radiation, heating, and/or used strong bases like NaOH/KOH dehydrofluorinated PVdF have been considered. In addition, one publication that demonstrated an FT-IR of PVdF after soaking in $AlCl_3$:EMImCl (1.3:1) electrolyte [32] was taken into account. The FT-IR spectra of s-PVdF (**Fig. 18 C**) show four main differences, compared to the p-PVdF one. First, the dominant bands at 2560-3725 cm^{-1}, 1639 cm^{-1}, 1569 cm^{-1} and 1458 cm^{-1} are visible. At first sight, a dehydrofluorination of the binder material was taking place in contact with the ionic liquid. In the case of a successful DHF, additional sp^2 hybridized carbon-carbon double bands appear at 1639 cm^{-1} and 1569 cm^{-1} [149,150]. In addition, the corresponding -CF_2-based bands become weaker and lower in intensity, which would indeed lead to the formation of C=C bonds and the release of hydrofluoric acid (HF). However, the bands at 3725-2560 cm^{-1} and 1458 cm^{-1} indicate that still $EMIm^+/AlCl_4^-$ is inside the sample. The broad huge band is based on the interaction of C-H symmetric/asymmetric stretching of the alkyl chains, which is causing the signal at 1458 cm^{-1} as well, N-H stretching of the amide and probably O-H stretching, which can interact with chloride ions [151]. Since the washing process was not enough, or the $EMIm^+/AlCl_4^-$ is stuck inside the s-PVdF matrix, several important bands of $EMIm^+$ are overlapping with DHF-PVdF, therefore, it is hard to say if the DHF was at least partly occurring. All overlapping bands of s-PVdF and $EMIm^+$ are listed in **Table S4**, which are based on several reports about EMImCl-based systems [151,152]. Especially the band at 1569 cm^{-1} can lead to a misinterpretation since the signal can appear because of O-H deformation or carbon-carbon double bonds caused by DHF [153] but at the same time, it can be assigned as the C=C asymmetric stretching vibration of the imidazolium ring [152,154]. The same results have been obtained with s-PVdC (**Fig. 18 D**). Only the broad and vanished area between 1050-400 cm^{-1} implies a dehydrochlorination (DHC) reaction [146,155,156]. All overlapping bands of s-PVdC and $EMIm^+$ are listed in **Table S4**. To overcome the problem of overlapped signals of s-PVdF and s-PVdC with IR-active modes of EMImCl, Raman measurements have been done.

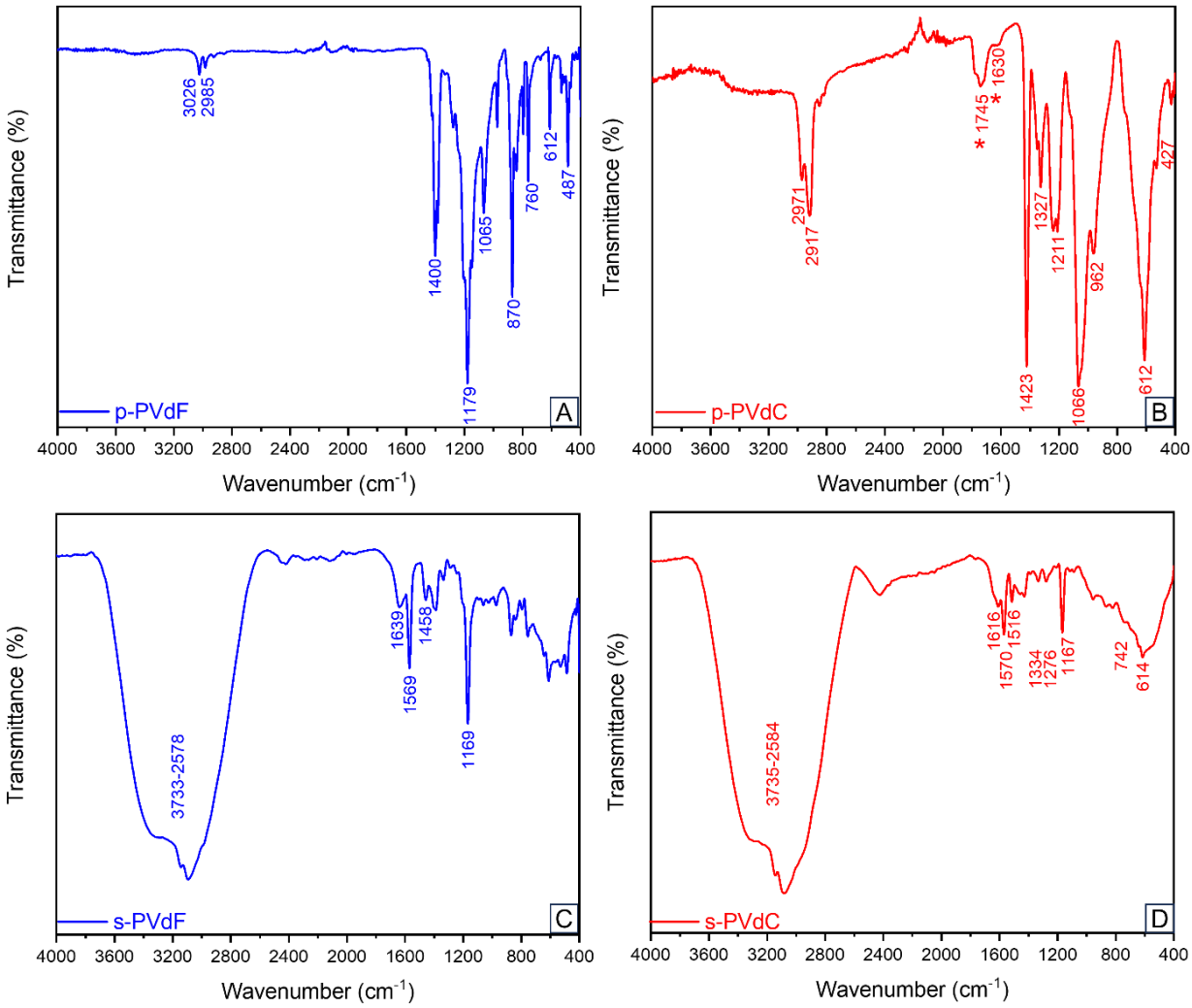

Figure 18 Fourier-transform infrared (FT-IR) spectrograms of (pristine) p-PVdF (A) and p-PVdC (B) powders and soaked in $AlCl_3$:EMImCl s-PVdF (C) and s-PVdC (D). Reprinted from Journal of the Electrochemical Society Vol. 171 No. 11 by E. Zemlyanushin *et al*. Copyright 2024 by IOP Publishing [34].

Figure 19 C shows the Raman spectra of the s-PVdF. The Raman results indicate the formation of amorphous carbon (AC) after contact with the Lewis acidic $AlCl_3$:EMImCl ionic liquid electrolyte. After sample immersion, typical Raman broad signals for AC at 1580 cm^{-1} and 1342 cm^{-1} are present [157,158], while other Raman bands from the pristine material are not visible anymore (**Fig. 19 A**). The conclusion is that the DHF, caused by interaction with $Al_2Cl_7^-$, leads to the carbonization of PVdF. The formation of pure carbon would also explain the colour change of the colourless powder, as well as, of the electrolyte from colourless/yellowish to black. In addition, the vibration mode at 2200 cm^{-1} is an indication of the formation of sp hybridized carbon-carbon triple bond, the so-called polyyne, which has been reported to be

typical for the dehydrohalogenation of halogens-containing polymers [159,160]. A similar result is obtained for s-PVdC, whereby the D- and G bands are slightly shifted to lower wavenumbers (**Fig. 19 D**). The corresponding signals are located at 1485 cm^{-1} and 1107 cm^{-1}. The Raman spectra of p-PVdC (**Fig. 19 B**) were measured after dissolving the chloride-based binder material in acetone because the pure material was impossible to measure. The pristine material shows huge differences from the literature spectra of Xiao *et al.* [148]. One possible explanation could be a structural change by dissolving in acetone. On the other hand, maybe the spectra differ because of the decomposed PVdC surface caused by UV. As a result, DHC can occur and intern crosslink products can be formed. One indication of an impurity is given by the carbonyl group, measured in the FT-IR (**Fig. 18 D**). The same group activity can be identified by Raman spectroscopy. Taking into account that the D- and G-bands are shifted after reacting with the IL, it can be assumed that the PVdC changed. Streletskiy *et al.* [158,161] investigated the DHC of PVdC-PVC and obtained a similar Raman band shift. This is an indication that the used PVdC formed some dechlorinated sequences in the polymer chain, which caused a longer sp^2-carbon hybridization bond compared to pure PVdC [161,162]. Moreover, vibration modes at 2200 cm^{-1} appear because of the formed carbon-carbon sp triple bond [161].

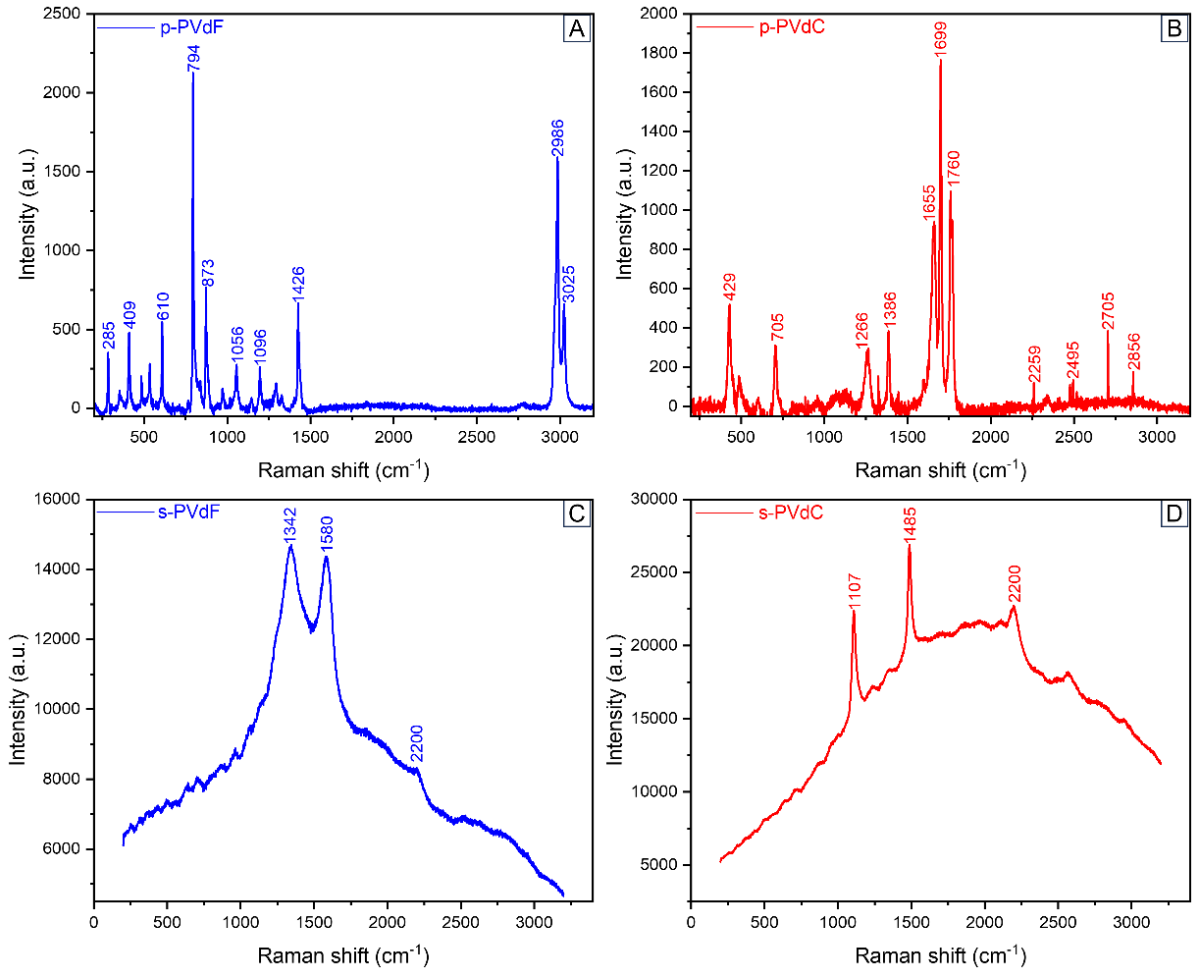

Figure 19 Raman spectra of (pristine) p-PVdF (A) and p-PVdC (B) powders. Furthermore, in $AlCl_3$:EMImCl ionic liquid (soaked) s-PVdF (C) and s-PVdC (D). Reprinted from Journal of the Electrochemical Society Vol. 171 No. 11 by E. Zemlyanushin *et al*. Copyright 2024 by IOP Publishing [34].

On the other hand, Niino and Yabe [163] obtained the same Raman signals for dehydrochlorinated PVdC, *via* photo-irradiation, but unfortunately, they do not show Raman spectra of the pristine material, which could confirm the same kind of degradation as presented in this thesis. All results indicate that $EMIm^+/AlCl_4^-$ always remains in both polymer matrices and that a DHF and DHC for PVdF and PVdC, respectively, occur. Further investigations *via* NMR (nuclear magnetic resonance) spectroscopy have been done to understand the influence of formed HF and HCl on the electrolyte and the impact of these binders on the electrochemical performance of an Aluminum-Graphite (Al-C) cell. In the case of the ^{19}F-NMR of the ionic liquid after soaking PVdF powder (**Fig. 20 A**) for 1 hour, two peaks at -155.40 ppm and -158.15 ppm can be observed.

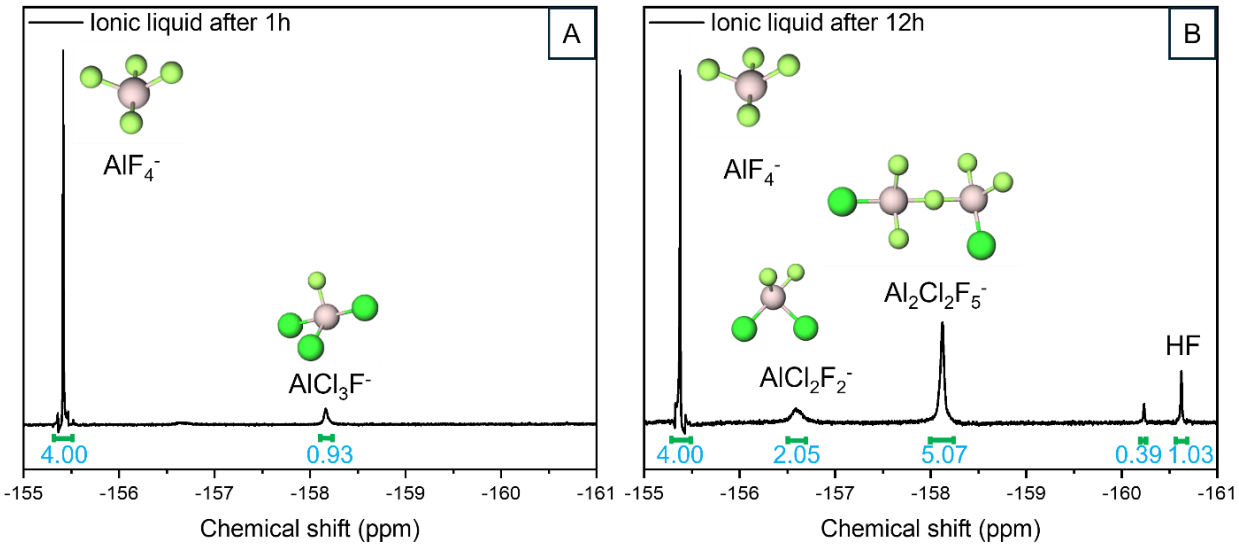

Figure 20 ^{19}F-NMR (nuclear magnetic resonance) spectroscopy of ionic liquid electrolyte (black liquid) after soaking PVdF for 1 hour (A) and electrolyte soaked for 12 hours (B). Adapted from Journal of the Electrochemical Society Vol. 171 No. 11 by E. Zemlyanushin *et al*. Copyright 2024 by IOP Publishing [34].

The chemical shifts at -155.40 ppm and -158.15 ppm belong to aluminum fluoride (AF) and aluminum chlorofluoride (ACF) complexes. Regarding the report of Bodor *et al.* [164] and Ji *et al.* [165], a less negative chemical shift in the ^{19}F-NMR is related to a complex with higher fluoride content. Therefore, the peaks around -155.40 ppm appear because of the presence of tetrafluoroaluminate (AlF_4^-). The chemical shift at -158.15 ppm should belong to trichlorofluoroaluminate ($AlCl_3F^-$). After 1 hour, the DHF of the PVdF polymers leads to halogen exchange of the ionic liquid electrolyte. After soaking PVdF for 12 hours (**Fig. 20 B**), the black ionic liquid was measured again. Besides the AlF_4^- signal around -155.36 ppm and the peak at -158.11 ppm, three additional signals at -156.59 ppm, -160.22 ppm (unknown), and -160.61 ppm were obtained. However, the chemical shift at -158.11 ppm does not anymore belong to the $AlCl_3F^-$ complex. With further soaking time, the DHF of the PVdF binder has increased to the level that HF at -160.61 ppm can be detected. Formed HF and ACF complexes can encourage further and faster DHF, which results in the formation of dichlorodifluoroaluminate ($AlCl_2F_2^-$) out of $AlCl_3F^-$ and a downshift to - 156.59 ppm. The peak at -158.11 ppm belongs to the new dichloropentafluorodialuminate ($Al_2Cl_2F_5^-$) complex. It is important to notice that one of the $Al_2Cl_2F_5^-$ fluorine atoms serves as a bridge between the two chlorodifluoroaluminate ($AlClF_2$)-parts. Otherwise, the signal would not be a singlet due to the different chemical environment of all the other fluorine atoms and the whole complex would

not get an upshift [166]. This would be comparable with the bromotrichloroaluminate ($AlCl_3Br^-$) and bromohexachlorodialuminate ($Al_2Cl_6Br^-$) (bromine atom is bridging) complexes, which have been used for Aluminum-Sulfur (Al-S) and Aluminum-Selenium (Al-Se) batteries [167,168]. Moreover, by increasing the soaking time the DFH and the hydrolyzation to HF are more favorable. ^{1}H- and ^{13}C-NMR measurements of the black ionic liquid electrolyte confirm that EMImCl does not participate in the side-reaction with the PVdF. The ^{1}H- and ^{13}C-NMR spectra of fresh and reacted black electrolytes are shown in **Figure S3 A-D**, respectively. Based on the NMR and Raman results, PVdF and PVdC are considered to be a precursor carbon sources. With the progressive decomposition, the ratio of $AlCl_3$:EMImCl should decrease because of the loss of $Al_2Cl_7^-$ required to produce AC, HF, HCl, $AlCl_3F^-$, $AlCl_2F_2^-$, $Al_2Cl_2F_5^-$, $AlCl_4^-$ and AlF_4^-. AlF_4^- is considered to be a result of the equilibrium of formed AlF_3 and HF [165]. The proposed initial reaction equation for PVdF and PVdC is shown in **Equations 25, 26** and **27**, respectively.

$$PVdF: \quad 2(C_2H_2F_2)_n + nAl_2Cl_7^- \rightarrow 4nC + nAlF_3 + nAlCl_4^- + nHF + 3nHCl \quad (25)$$

$$AlF_3 + HF \rightleftharpoons AlF_4^- + H^+ \quad (26)$$

$$PVdC: \quad (C_2H_2Cl_2)_n + 2Al_2Cl_7^- \rightarrow 2nC + 2nAlCl_4^- + 2nAlCl_3 + 2nHCl \quad (27)$$

A reaction cycle mechanism of the DHF for the formation of sp^2 hybridized carbon-carbon double bonds in the PVdF polymer chain is shown in **Figure 21**.

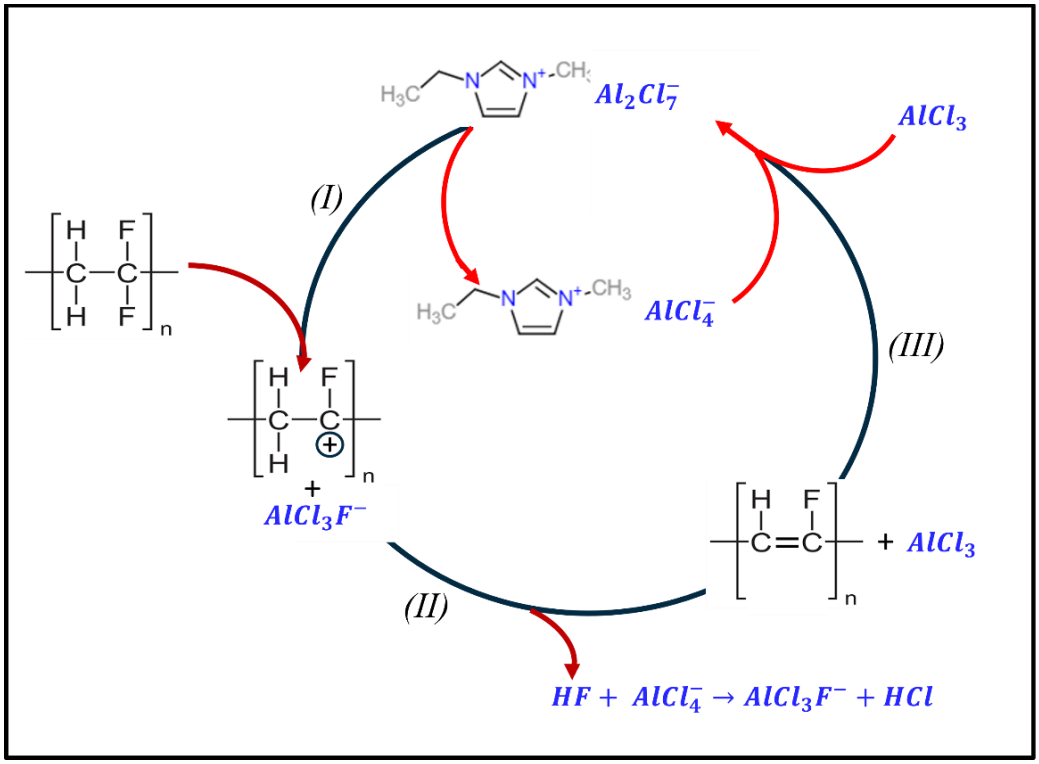

Figure 21 Reaction cycle mechanism of the dehydrofluorination (DHF) of PVdF resulting in a sp^2 hybridized carbon-carbon double bond and aluminum chlorofluoride (ACF) formation.

This kind of reaction mechanism principle is similar to the so-called Friedel-Crafts alkylation and acylation [169]. The main difference between the dehydrofluorination and the Friedel-Crafts reactions is the reaction-initiating species. Both, the alkylation and acylation require $AlCl_4^-$ as an initiator, while the dehydrofluorination occurs due to the presence of $Al_2Cl_7^-$ active species. In the first step, PVdF forms a carbocation during defluorination by $Al_2Cl_7^-$, which splits into $AlCl_4^-$ and $AlCl_3F^-$. Afterwards, $AlCl_3F^-$ can fulfil the dehydrofluorination with the PVdF-carbocation to form a carbon-carbon sp^2 hybridization bond and the release of $AlCl_3$ and HF. In turn, HF is able to react with $AlCl_4^-$ to form more $AlCl_3F^-$ and HCl, which explains the absence of HF after a short reaction time. However, after 12 hours the concentration of HF is saturated and can be detected *via* ^{19}F-NMR (**Fig. 20 B**). Last but not least, formed $AlCl_3$ reacts with $AlCl_4^-$ to form the unchanged $Al_2Cl_7^-$ species, which can again initiate further DHF. Under the same mechanism principle, the formation of a sp hybridized carbon-carbon triple bond (polyyne) can be formed. The only urgent condition is, that the dehydrofluorination leads to a cis arrangement of the remained hydrogen and fluoride atoms (**Figure 22**). If the dehydrofluorination results in a trans arrangement, a carbon-rich material such as Graphene, Graphene oxide (GO) or AC.

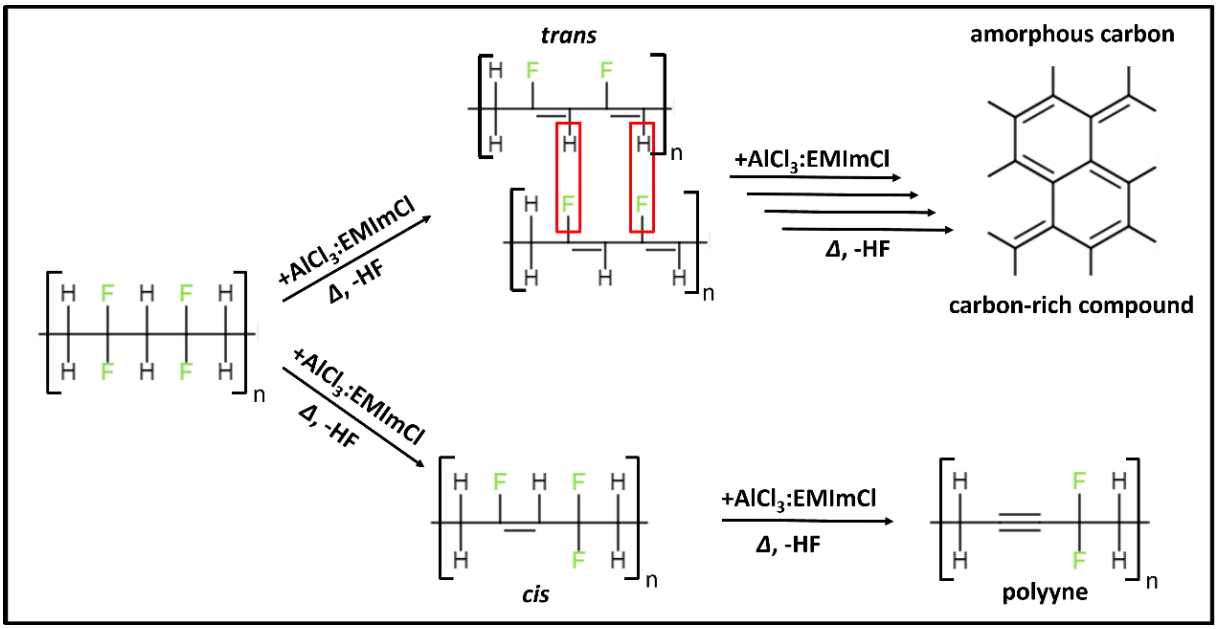

Figure 22 Reaction mechanism for the formation of carbon-rich compounds, such as amorphous carbon (AC), due to dehydrofluorination (DHF) resulting in a sp^2 hybridized trans arrangement, while a cis configuration leads to an sp hybridized carbon-carbon triple bond (polyyne).

Since the Raman D- and G bands at 1342cm^{-1} and 1580 cm^{-1} for s-PVdF and the slightly shifted bands at 1107 cm^{-1} and 1485 cm^{-1} for s-PVdC are typical for AC, it can be assumed that the trans arrangement during the DHF is more favoured. However, the Raman spectra of both polymers also indicate the formation of polyyne which results in the band at 2200 cm^{-1}. The transformation of PVdF and PVdC to amorphous carbon and polyyne is more encouraged by increased temperatures. Formed hot spots are generated by the side-reactions between $Al_2Cl_7^-$ and the polymers themselves [18,33]. While mixing both components the vial becomes hot due to the exothermic reaction. Khokarale *et al.* [170] obtained similar results of the phase change of PVdF from the α- to the polar *β*-phase as well as the dehydrofluoriantion which results in the formation of carbon-rich materials. Two main aspects have to be clarified at this point. Kohkarale *et al.* [170] used an ionic liquid made of 1-ethyl-3-methylimidazolium acetate [$EMIm^+$][CH_3COO^-], while in this work 1-ethyl-3-methylimidazolium heptachlorodialuminate [$EMIm^+$][$AlCl_4^-$/$Al_2Cl_7^-$] has been chosen. Furthermore, acetic acid (CH_3COOH (AA)) has been added to [$EMIm^+$][CH_3COO^-] in different ratios and treated under increased temperature after adding PVdF powder. The purpose was to obtain a more porous and electroactive PVdF phase, which has never been applied and tested in any kind of battery system.

Further investigation has been done by ultraviolet-visible (UV-VIS) spectroscopy, whereby 1,2-Difluorobenzene (DFB) was chosen as a solvent since it is not reacting and overlapping with the UV-VIS bands of the IL electrolyte (similar to **Chapter 4.2**).

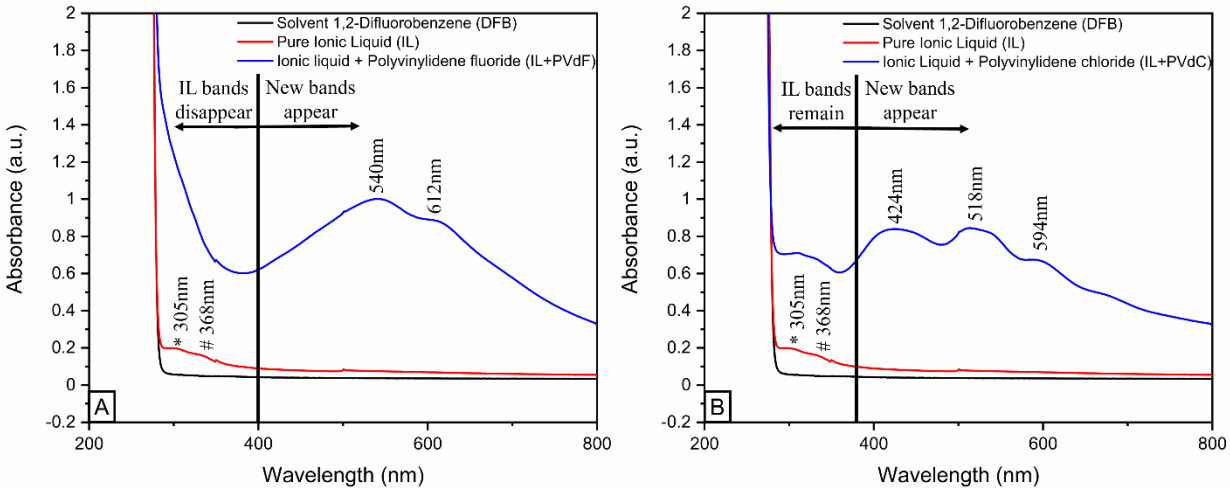

Figure 23 Ultraviolet-visible (UV-VIS) spectra of 1,2-Difluorobenzene (DFB) solvent, pure ionic liquid electrolyte and (A) PVdF after reaction with the ionic liquid and (B) PVdC after the reaction with the electrolyte. Marked bands belong to the $EMIm^+$ (305 nm, asterisk) and $Al_2Cl_7^-$ (368 nm, hash).

Since the wavelength of absorbance depends on the solvent, the UV-VIS results about IL electrolyte of Lang *et al.* [113] and Lyu *et al.* [169] were involved in the spectra interpretation. By using ethanol (C_2H_5OH (EtOH)) as a solvent for the ionic liquid, Lyu *et al.* [169] obtained bands in the very same wavelength region as shown in **Figure 23**. Considering the results of both groups the band at 305 nm can be assigned to the $EMIm^+$ cations, while the band at 368 nm corresponds to $Al_2Cl_7^-$ anions [113,169]. After the reaction between PVdF and the IL, two new bands at 540 nm and 612 nm appear. A similar spectrum is obtained after the reaction of PVdC with IL and results in three new bands at 424 nm, 518 nm, and 594 nm. Unfortunately, it was not possible to identify the newly formed species which causes an adsorption at the corresponding bands. However, it is believed that they belong to formed polyynes with a random arrangement of sp, sp^2 and sp^3 hybridizations. During the UV-VIS measurements, black unsolvable particles were distributed in the liquid samples inside a cuvette. In that case, it is possible to measure formed particles too. In contrast to the UV-VIS spectroscopy, performed ^1H- and ^{13}C-NMR (**Fig. S3**) measurements could not show any structure information because the black powder was unsolvable in deuterated solvents and just precipitated inside the NMR tubes.

After studying the decomposition product of PVdF and PVdC in contact with Lewis acidic ionic liquid electrolyte, galvanostatic cycling with potential limitation (GCPL) and cyclic voltammetry (CV) measurements have been done. The cells consist of positive electrodes made of Graphite prepared with PVdF and PVdC binder materials and pure Al-foil as the negative electrode. **Figure 24 A**, shows the GCPL of PVdF- and PVdC-based Graphite electrodes at a current density of 20 $mA \cdot g^{-1}$. In both cases, the initial discharge capacity of circa 45 $mAh \cdot g^{-1}$ is quite low but increases with further cycles. After 80 cycles, the PVdF-based cell reaches a discharge capacity of ~70 $mAh \cdot g^{-1}$ (average coulombic efficiency (CE): ~92%) while the PVdC electrode extends to ~50 $mAh \cdot g^{-1}$ (average CE: ~77%). In the case of the PVdF-based electrodes, the specific capacity has been reported to be in the range of 70-80 $mAh \cdot g^{-1}$ [78]. The increase in capacity with further cycles has been described already for several different kinds of Graphite-based cathode materials. For example, Elia *et al.* [171] reported a rising capacity for Pyrolytic Graphite (PG) and Mukundan *et al.* [172] for Natural Graphite (NG). Elia [171], Mukundan [172] and Huang [173] explain the increase of the capacity with further cycle number by the increase of the *d*-spacing of the Graphite layers. By this, the reversible intercalation of the $AlCl_4^-$ anions can be improved, which results in a higher capacity and enhanced rate capability.

It is expected that the capacities of both, PVdF and PVdC-based materials would be relatively low because of the chosen high wet thickness of 200 µm (dry thickness: 238 nm). Huang *et al.* [173] reported that in $AlCl_3$-based RABs, a high Graphite loading leads to lower capacity because the higher volume of Graphite hinders the smooth diffusion of $AlCl_4^-$ into the host material. Just for comparison, Appiah *et al.* [174] figured out that the optimal thickness of a Graphite electrode, made of 90% Graphite mixed with 10% PVdF binder, in an $AlCl_3$:EMImCl ionic liquid electrolyte system is 50 µm. Moreover, a greater thickness increases the diffusion length of $AlCl_4^-$ and prevents complete deintercalation [174]. By this, the concentration of the $AlCl_4^-$ in the ionic liquid electrolyte decreases and the remaining active species inside the Graphite layers hinder intercalation pathways. Consequently, the charge/discharge capacities become lower. In addition, initial cycles count as the activation phase of the Graphite during the intercalation of $AlCl_4^-$. During this phase, the specific charge capacity increases while the specific discharge capacity decreases due to irreversibly trapped $AlCl_4^-$ anions [172]. For both materials, the CVs (**Fig. 24 B**) show similar current density as well as stability, which is consistent with the results of Wei *et al.* [175], who compared Graphite and Graphite/AC RABs based on $AlCl_3$:EMImCl (1.3:1) ionic liquid electrolyte without any changes in redox activity.

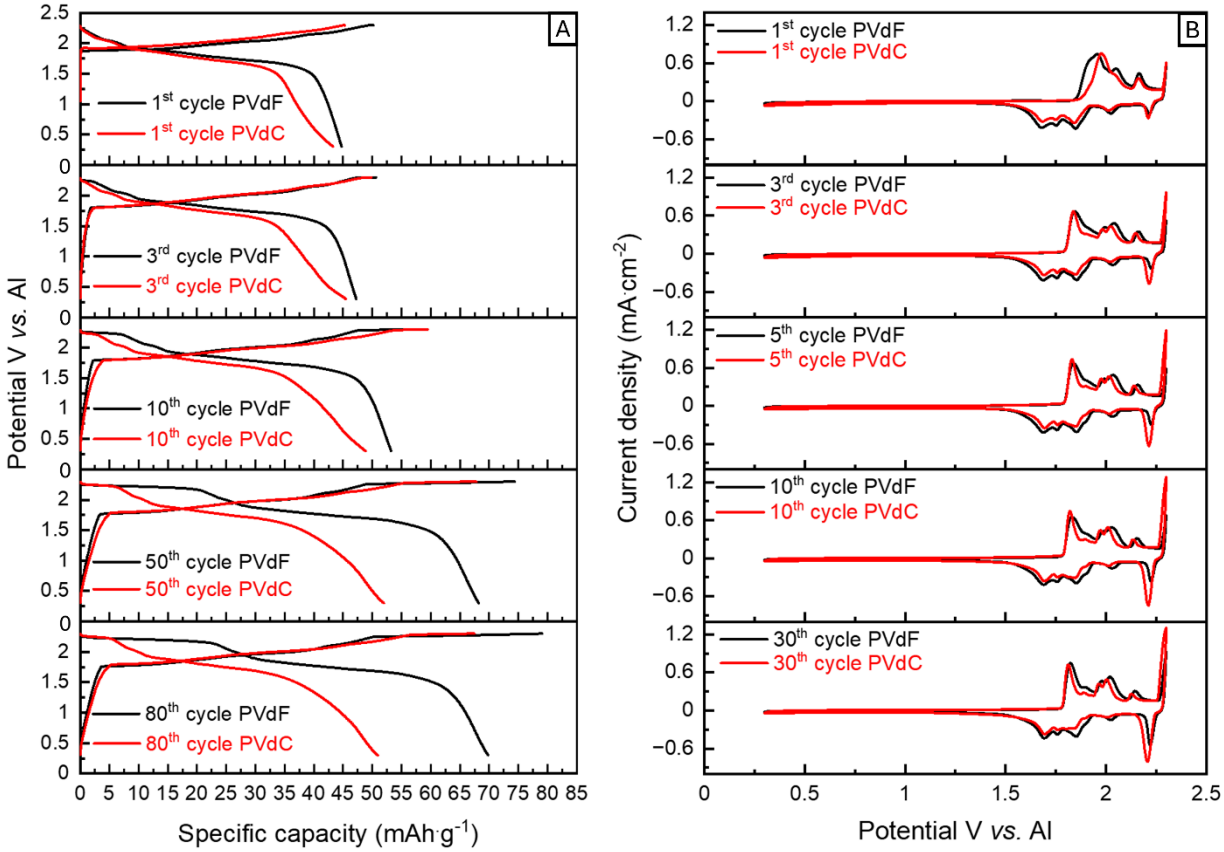

Figure 24 (A) Galvanostatic cycling with potential limitation (GCPL) in the potential window 0.3 V-2.3 V at 20 $mA{\cdot}g^{-1}$ of PVdF- and PVdC-based Graphite positive electrodes at different cycle numbers. (B) Corresponding cyclic voltammograms (CVs) with a scan rate of 0.20 $mV{\cdot}s^{-1}$ at different cycles.

By this, it is proven that amorphous carbon contributes to improved stability and higher capacity of Graphite-based RABs without showing any redox activity. The difference between PVdF and PVdC-based electrodes is the newly formed AlF_3/AlF_4^- species (**Eq. 25** and **26**), which could be active as well. XPS results of Chen *et al.* [35] confirm that the ratio of -CF_2 signal of PVdF-based electrodes after getting in touch with $AlCl_3$-based ionic liquid electrolyte, reinforces the ^{19}F-NMR results that the newly formed species is dissolved in the electrolyte. Moreover, in 2023, Yu *et al.* [33] demonstrated *via* Raman measurements that 2.5 w(%) of added PVdF is enough to destroy the $AlCl_4^-$ and $Al_2Cl_7^-$ species of the ionic liquid. By this, the ionic liquid electrolyte gets deactivated in its functionality. This could explain why the capacity of the PVdC-based samples is stable at a certain value without relevant variations upon cycling. Captured $AlCl_4^-$ in the Graphite host and partly destroyed/deactivated species are replaced by newly formed active species by the side-reaction between $Al_2Cl_7^-$ and PVdC. On the other hand, PVdF generates new $AlCl_4^-$ as well as AlF_4^-, which should be able to intercalate too. Indeed,

Matsumoto *et al.* [176] showed that the intercalation of AlF_4^- occurs successfully in Graphite. Moreover, in their study, they suggest a further side-reaction of the intercalation product (C_XAlCl_4) with formed HF (**Eq. 28**) [177].

$$C_xAlCl_{4\,(s)} + 4HF_{(l)} \rightarrow (x - 0.25)C_{(s)} + AlF_{3\,(s)} + 4HCl_{(g)} + 0.25CF_{4\,(g)} \quad (28)$$

In that case, the formed AlF_3 can further react with HF to produce AlF_4^-, as shown in **Equation 26**. Wang *et al.* [26] even predict that the use of AlF_4^- as active intercalating species of RABs will lead to larger cathode-specific capacity, higher voltage and higher rate capability. Another reason for the increase of capacity with further cycle numbers could be caused by the fact that electrochemically inactive binder materials act like precursors for generating amorphous carbon. Amorphous carbon has been shown by Wei *et al.* [175] to be able to protect the Graphite from disintegration and, therefore, contribute to the improvement of the cycling stability of RABs. Moreover, amorphous carbon can enhance the surface area and increase the conductivity [178]. This is probably the reason why many researchers still use PVdF as a binder despite the side-reaction with the ionic liquid electrolyte. Without amorphous carbon, pure Graphite electrodes showed in $AlCl_3$/EMImCl (1.3:1) electrolyte a lower initial increase of the specific capacity and a faster capacity decay [175]. Compared to PVdF, one major weak point of the PVdC binder must be taken into account; the binding effect of PVdC is noticeably worse. After preparing the electrodes, it was very difficult to handle the PVdC-based Graphite electrode without damaging the surface because of the lack of cohesion between the active material and the carbon paper current collector. Since the contact of Graphite to the current collector was very weak, the detaching effect (**Fig. S4 A-H**) during cycling can explain the very low coulombic efficiency of ~77% of PVdC, compared to ~92% of PVdF. To sum up, the side-reactions of PVdF and PVdC binder materials for RABs have been investigated. Both polymers show the same kind of interaction with the Lewis acidic $AlCl_3$:EMImCl (1.5:1) ionic liquid. The used electrolyte forms two active species, $AlCl_4^-$ and $Al_2Cl_7^-$ while $Al_2Cl_7^-$ is responsible for the dehydrofluorination (DHF) and dehydrochlorination (DHC) of PVdF and PVdC, respectively. At the same time, the $EMIm^+$ countercation does not show any changes and therefore does not participate in the side-reactions with the binder materials. As a result of DHF and DHC, the polymer binders change to an amorphous carbon compound, by forming sp^2 carbon-carbon hybridization and possibly sp polyyne. In the case of PVdF, the two typical D- and G bands of amorphous carbon (1580 cm^{-1} and 1342 cm^{-1}) have been observed, while PVdC

shows a slight shift to lower wavenumber (1485 cm^{-1} and 1107 cm^{-1}). This Raman shift is caused by a shorter average carbon-carbon bond of the final product of PVdC, which is a further indication of the formed sp hybridization. In addition, ^{19}F-NMR measurements of ionic liquid electrolyte after soaking PVdF for 1 hour, validate the formation of AlF_4^- and $AlCl_3F^-$ anions. After a soaking time of 12 hours, AlF_4^-, $AlCl_2F_2^-$, $Al_2Cl_2F_5^-$ and HF are detected. Electrochemical tests show that PVdF is a better binder material than PVdC for Aluminum-Graphite RABs. Both the capacity and coulombic efficiency of a Graphite-based electrode are noticeably better by using PVdF as a binder. The reason for that could be the additional AlF_4^- active species which can intercalate into the Graphite host.

5.3 Conclusion

Formed amorphous carbon can protect the Graphite from disintegration and, therefore, contribute to the improvement of the cycling stability of RABs without showing any redox activity. Furthermore, amorphous carbon can increase the surface area of the electrode and improve the conductivity. Moreover, cross-link reactions between the polymer chains are also possible as ring-closing reactions (**Fig. 22**) because of the exothermic reaction between $Al_2Cl_7^-$ and the polymers as well as the great ability of $AlCl_4^-$ to initiate such reactions. Both binder materials form during the DHF and DHC reactions $AlCl_4^-$, HF and HCl, respectively. The generated acids enable a further, even easier DHF and DHC reaction. However, formed HF and HCl can cause additional corrosion reactions between the metallic current collector and cell parts, which consequently lead to even more unwanted side-reactions. Furthermore, the mechanical instability, caused by the lack of cohesion between Graphite and carbon paper current collector, of PVdC-based electrodes, makes further investigations and research difficult.

5.4 Outlook and Future Work

Besides the fact that the side-reactions between PVdF and PVdC with the Lewis acidic $AlCl_3$:EMImCl (1.5:1) ionic liquid electrolyte have a positive impact on the electrochemical performance of Graphite-based RABs, it is always better to use a stable binder material. Unwanted and undesired side-reactions can disturb the sensitive working principles and mechanisms of individual cells and batteries. The investigated formation of AlF_4^- is directly connected with the lowering of the $AlCl_4^-$ concentration, resulting in a new molar ratio between $AlCl_3$ and EMImCl. Furthermore, the acidity of the ionic liquid electrolyte will decrease due to the lower Lewis acidity of AlF_4^- compared to $AlCl_4^-$ (order of Lewis acidity: $AlF_4^- < AlCl_4^- < AlBr_4^- \approx AlI_4^-$) [179]. A lower acidity can influence the electroplating and electrostripping process and the AlF_4^- can lead to the formation of an additional F-based solid

electrolyte interface (SEI) on the Al negative electrode. Moreover, the newly formed aluminum tetrafluoride complex can show two different negative aspects, both resulting in loss of specific capacity: (I) In the case that AlF_4^- is not able to intercalate into the positive electrode and (II) if the AlF_4^- destroy the structure or get stuck in the host material and damage or block suitable pathways for active intercalating species. Therefore, it is urgent to find and use stable binder materials for further research on RABs. Initial soaking tests of polyvinylpyrrolidone (PVP**, Fig. 25 A**) in $AlCl_3$:EMImCl (1.5:1) electrolyte indicate no reactions between the polymer powder and the ionic liquid. Neither a dissolution of the PVP nor a change of the white powder and colourless/yellowish electrolyte occurs. Uemura *et al.* [134] investigated the stability of polyimide (PI, **Fig. 25 B**) in $AlCl_3$:EMImCl (1.5:1) ionic liquid electrolyte. Unfortunately, the exact name or structure of the used PI is not mentioned, therefore, a typical PI-subunit is shown in **Figure 25 B**. Equal to PVP (soaked for 3 days), PI (soaked for 168 days) did not show any visible degradation of the polymer or the electrolyte.

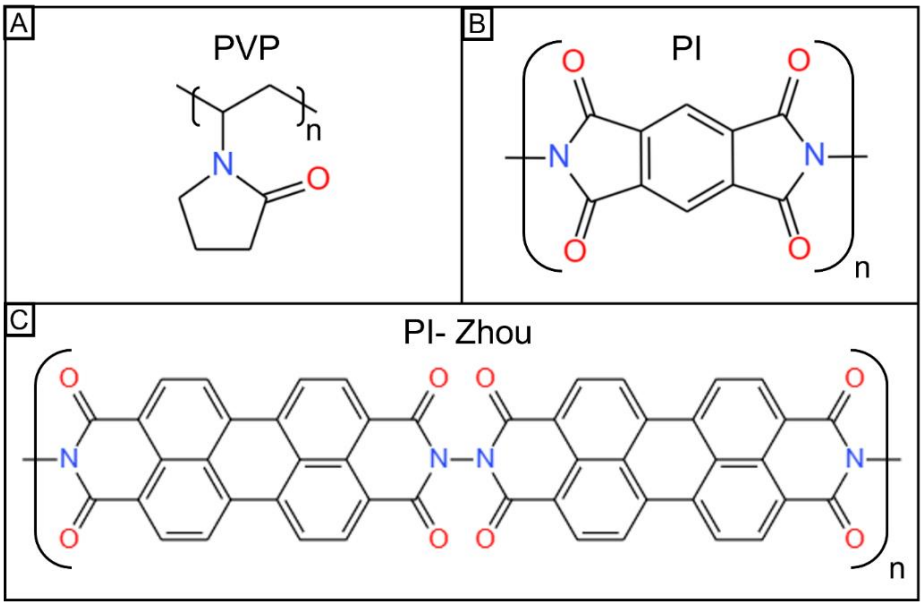

Figure 25 Molecular structure of (A) polyvinylpyrrolidone-PVP, (B) polyimide-PI and (C) PI-Zhou used by Zhou *et al*. [180].

Both polymers have a similar subunit structure, which could be responsible for the stability in contact with $AlCl_3$-based Lewis acidic electrolytes. Zhou *et al.* [180] proposed a reversible interaction between the carbonyl groups of the PI-Zhou (**Fig. 25 C**) and the Al-Cl complex ($AlCl_3$:EMImCl (1.3:1)) during discharge. Analogous intermolecular interplay can take place between $AlCl_4^-/Al_2Cl_7^-$ and the carbonyl groups of PI and PVP without decomposition or dissolution of the polymer binder materials. Uemura *et al.* [134] demonstrated a charge-discharge

profile of Graphene nanoplatelet-PI composite positive electrode in an $AlCl_3$:EMImCl (1.5:1) ionic liquid electrolyte with a stable discharge capacity of circa 70 $mAh \cdot g^{-1}$ at 2000 $mA \cdot g^{-1}$ over 3000 cycles. Such results could be obtained by using PVP as a binder too. However, further investigations of the PVP structure after soaking and cycling in $AlCl_3$:EMImCl (1.5:1) electrolyte-based cells are required to confirm the stability of the polymer and its impact on cycling stability as well as rate capability in RABs.

6. Alloying of the Aluminum negative electrode

6.1 Introduction: Activation and Protection of the Aluminum negative electrode

The greatest drawback of pure Al-foil to be used as a negative electrode in RABs is the naturally formed aluminum(III)-oxide (Al_2O_3) protective layer. The thickness of natural Al_2O_3 passivation film formed in the ambient atmosphere on rolled or annealed Al-foil typically ranges from 3-10 nm, while in fabricated artificial reinforced Al (*e.g.*, *via* anodization, chemical or plasma oxidation) the passivation film ranges from 0.1-5 µm [181]. Since the insulating and protective oxide layer suppresses the proper electroplating and electrostripping of Al [182], it is crucial to remove the oxide layer, which is done by chemical etching with Lewis acidic ionic liquid electrolytes. Besides $AlCl_4^-$, a second species ($Al_2Cl_7^-$) is formed, which is responsible for the electroplating- and stripping during cell cycling and corrodes the Al_2O_3 in contact between Al-foil and ionic liquid [183]. Next to chemical etching, other pretreatment techniques were established to remove the oxide film before cell assembling *e.g.*, *via* mechanical- and electrochemical polishing [174,182]. After removing the oxide layer by electropolishing, the Al-foil has a smooth surface, which suffers from crack and pit formation after soaking in $AlCl_3$:EMImCl (1.3:1) ionic liquid for 24 h. In contrast, untreated Al-foil shows linear cracks under the same conditions and it takes 96 h of soaking time to obtain a similarly distorted surface. On the other hand, Choi *et al.* [183] demonstrated that an electropolished Al metal with a residual thin oxide layer provides a high capacity and stable surface reactions due to a balanced Al electroplating and electrostripping. Because of the thin oxide film, the area for the interaction between pure Al and IL decreases. The *in-situ* activation of the untreated Al negative electrode takes about 15 cycles to remove the oxide layer locally [71,184]. Because of the initial activation cycles for the pristine Al-foil, the capacity increase is limited. A suitable explanation for this capacity restriction could be that the acidic IL dissolves the thinner parts of the oxide layer faster than the thicker film and the electrochemical reactions only occur in those areas and not on the whole surface, like for an electropolished foil. Based on all those results, it is not necessary to remove the Al_2O_3 completely. Instead, it is more favourable to modify the surface and/or the protective oxide film structure to allow better ion and electron diffusion during charge/discharge processes. Such a modification can be achieved by immersing the Al negative electrode into an $AlCl_3$-based ionic liquid solution which can reconstruct the oxide layer by first partial dissolution and the generation of a new porous structured Al_2O_3 film [182]. Another serious issue is the formation of dendrites (**Fig. 26 A**), followed by the occurrence of inactive ("dead")

Al (**Fig. 26 B**), which are also connected to the Al_2O_3 layer. Similar to Li, Na, and other Metal-Ion Batteries (MIBs), the dendrite formation, once started, cannot be controlled, especially at high current densities [185]. Chen *et al.* [186] demonstrated that an oxide layer can suppress the formation and growth of dendrites. In general, the effectiveness and influence of the Al_2O_3 film depend on the thickness, microstructure and modification. A thin oxide layer with a porous structure could be beneficial for the RABs performance [183]. However, the prevention of the formation of dendrites, dead Al and uncontrollable structure changes (cracks, pits, pulverization, *etc.*) are still unavoidable during the charge/discharge process of RABs with the mentioned pretreatment methods.

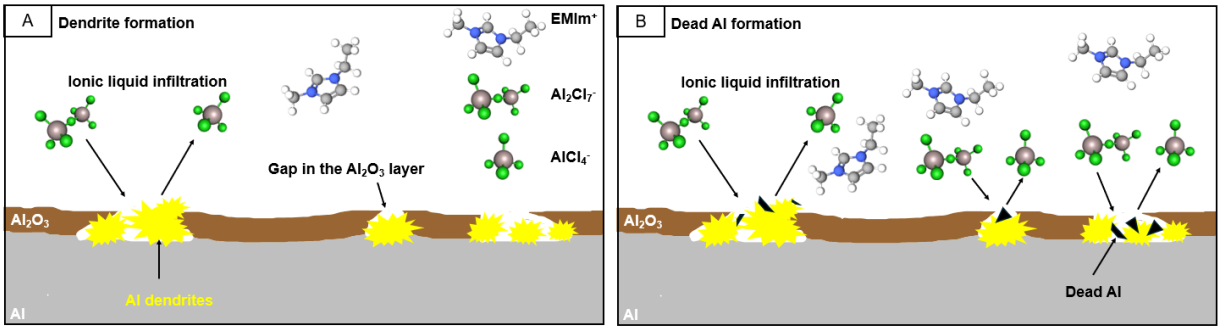

Figure 26 Schematic illustration of dendrite formation due to infiltration of ionic liquid electrolyte into gaps of the Al_2O_3 layer (A) and the formation of inactive "dead" Al (B).

Therefore, it is urgent to develop a new kind of negative electrode material to avoid all issues without creating further unfamiliar challenges and problems. One way to overcome the listed drawbacks of pure Al-foils is to establish an alloy system as a negative electrode. The issues of the interface/interphase include the electrochemical redox reactions, composition and structural changes of the Al surface, which influence the ion- and mass transport and kinetic behaviour. The interface/interphase can be regulated by the formation of an alloy, grain refinement, surface modification of the Al negative electrode and electrolyte additives [24,186]. Using different types of alloys seems to be a promising way to achieve a more resistant Al electrode for high-performance RABs. This is possible due to the capability of Al alloys to stabilize the Al interface. Some additional metal components can induce a more aluminophilic species on the electrode surface, which can provide smoother and easier Al nucleation and growth. At the same time, inactive components inside the alloys can act as a stabilizing lattice matrix to avoid a structural collapse of the negative electrode. Some alloy systems can suppress the formation of a thick protective oxide layer, which leads to reduced charge transfer resistance and smoother electroplating and electrostripping of the Al. Systems based on Al-Mg, Al-Fe, Al-Zn and Al-Cu are proposed to have a more stable electrode/electrolyte interface compared to pure Al [71,185].

The presence of a second or even third metal can create an oxide layer with more active defect sites, which may lead to more pathways for the Al-Cl complexes of the electrolyte to reach the pure Al surface for running reversible electroplating and electrostripping [185,187]. On the other hand, choosing the wrong alloy composition has the opposite effect of the preferred crack generation and induces a worse Al dendrite growth, which results in a short lifetime of RABs. From an economic point of view, it is desirable to develop Al negative electrodes based on smelter-grad metal (99% Al) instead of the high-cost and high-purity metal. Common household Al with a purity of ~99% is generally considered a cost-effective metal [51]. However, high-purity Al-foils are needed to avoid side-reactions of impurities such as iron and/or chrome, as shown in **Chapter 4.1**, **Eq. 11** and **12**). In 2024, the price per kilogram (kg) of high-purity Al varied based on the level of purity: 4N (99.99%) costs 261.95€·kg^{-1}, 5N (99.999%) costs 475.95€·kg^{-1} and 6N (99.9999%) costs 950.95€·kg^{-1}. The production of primary Al involves two main steps. First, alumina (Al_2O_3) is extracted from bauxite through the Bayer process. Next, Al manufacturing occurs *via* the Hall-Héroult process to achieve a purity of 3N (99.9%). Additional time- and energy-intensive steps, such as vacuum distillation, three-layer electrolysis and segregation, are necessary to achieve high- or ultra-high purity Al [51,188]. With the increasing purity of Al, the demand for required energy rises and causes higher production costs. An example of the energy consumption of different stages of Al production is visualized in **Figure 27**.

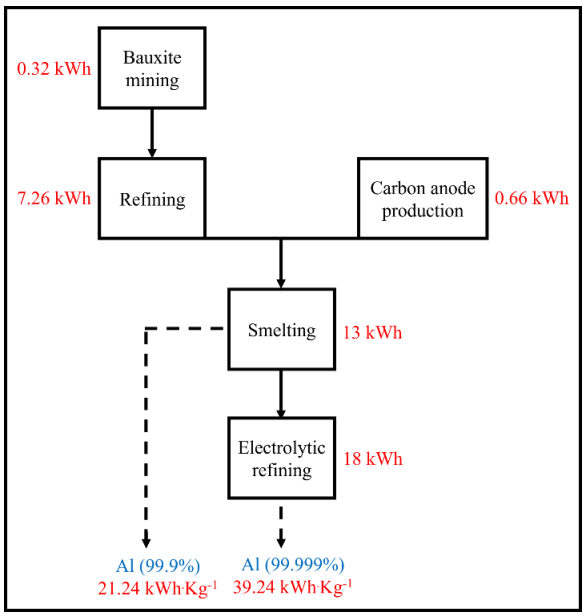

Figure 27 Flow chart of the average energy demand for the production of 3N Al (99.9%) and 5N Al (99.999%). Adapted from Applied Energy Vol. 90 No. 1 by H. Wang *et al.*, p. 101. Copyright 2012 by Elsevier [189].

It seems to be that the use of expensive high-purity Al-foils can only be avoided by the preparation and utilization of Al-based alloy systems. Alloys are merely responsible for deactivating the influence of impurities [190]. The main impurities that are more electropositive than Al, such as silicon (Si) and Fe, do not dissolve but remain in the alloy and accumulate gradually [191]. For instance, Mg is usually used in Al alloys to form Mg_2Si on interaction with possible Si impurities to avoid its harmful corrosion effect [77]. Even small amounts of impurities can affect the cell performance. Small changes in the Al alloy composition can result in substantial changes in the battery performance. An effective alloying element should possess the following properties: (I) a melting point below the melting temperature of Al (657°C); (II) good solid solubility in the Al matrix; (III) a higher nobility than Al in the electrochemical series as determined from the Pourbaix diagram [192]. According to these requirements, research on negative electrode alloys for aluminum batteries has focused on Mg, Zn, lead (Pb), tin (Sn), gallium (Ga), indium (In), manganese (Mn), mercury (Hg) and thallium (Tl) elements. Of all the mentioned potential alloying metals, Ga (29.76°C) and Hg (-38.83°C) have the lowest melting points [193] and can form an alloy with Al without high demand for thermal energy consumption. However, due to the high toxicity of mercury and mercury-based compounds [194], Ga has been chosen to prepare AlGa alloys with an eutectic temperature of only 26.6°C (**Figure 28**) as a semisolid self-healing negative electrode in RABs [77,192]. Two different methods can be applied to obtain AlGa alloys; (I: *Ex-situ* method) By mixing pure metallic Al and Ga at room temperature (RT) under continuous stirring [195] and (II: *In-situ* method) by adding a Ga-cations source into an ionic liquid electrolyte [192,193]. For the purpose of using the formed AlGa compound as a negative electrode in RABs, the simple mixing method of both metals was not suitable (see **Chapter 6.2**). Therefore, all further activation mechanisms, explanations, measurements and discussions are based on the *in-situ* prepared AlGa method.

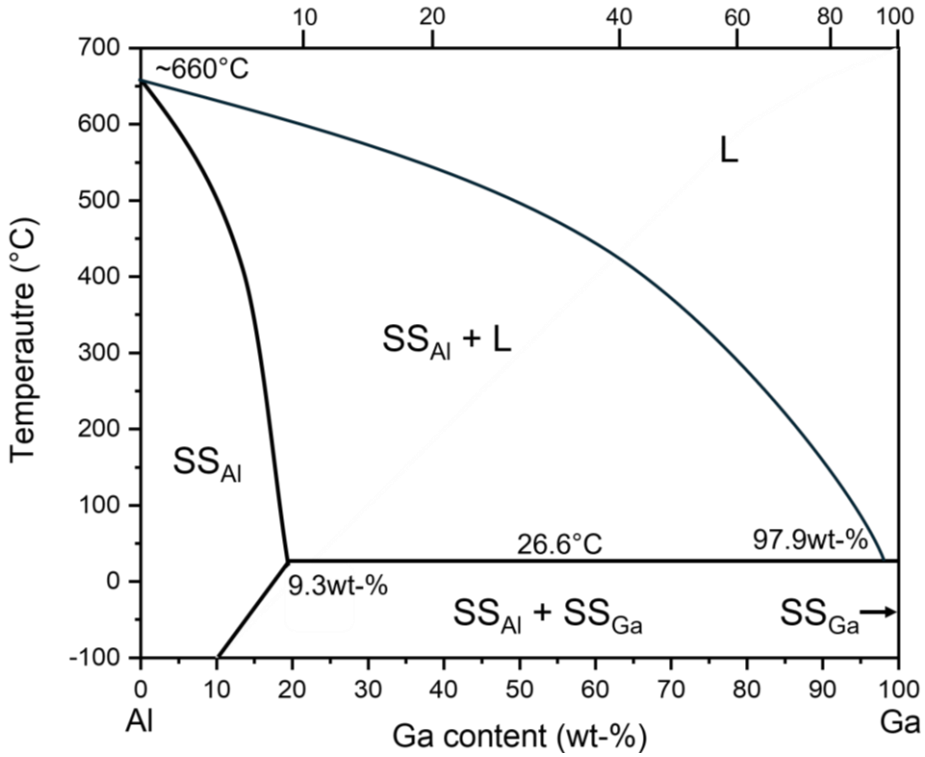

Figure 28 Binary phase diagram of Aluminum-Gallium (AlGa) alloy. Adapted from Bulletin of Alloy Phase Diagrams Vol. 4 No. 2 by J.L. Murray, 1983, p. 184. Copyright 1983 by Springer Nature [193].

In general, a four-step mechanism occurs for the activation of an Al negative electrode by involving one of the above-listed metals. In the following, all four mechanism steps will be demonstrated by adding gallium ions (Ga^{3+}) to the ionic liquid electrolyte. Breslin *et al.* [196] describe the deposition of Ga on the surface of Al *via* cathodic polarization out of an aqueous halide solution with gallium nitrate ($Ga(NO_3)$) as a gallium ion source. Since Ga/Ga^{3+} is galvanically nobler than Al, it gets enriched at the surface, which leads to the formation of an AlGa (**Eq. 29**) solid solution (ss) [196].

$$2Al + Ga^{3+} \rightarrow Al^{3+} + [Al_{bulk}Ga_{surface} \rightarrow (AlGa)_{ss}] \qquad (29)$$

According to the findings of Reboul *et al.* [197] for similar systems, namely alloys of Al with Zn, In, Sn and Hg, the proposed next activation mechanism steps can be described as follows: During the discharge process, the galvanic $(AlGa)_{SS}$ couple gets oxidized, which cause a dissolution (diss) and release of Al^{3+} and Ga^{3+} into the electrolyte (**Eq. 30**).

$$(AlGa)_{ss} \rightarrow Al^{3+} + Ga^{3+} + 6e^{-} \quad (30)$$

On the other hand, during the charge (reduction) process, released cations can be electroplated/alloyed on the Al negative electrode again, as illustrated in **Eq. 31**.

$$Al_{bulk} + Al^{3+} + 2Ga^{3+} + 9e^{-} \rightarrow 2(AlGa)_{ss} \quad (31)$$

The main activation effect of the negative electrode occurs during the formation of $(AlGa)_{SS}$ (**Eq. 31**). The electroplating of Al and Ga causes local detaching of the insulating Al_2O_3 on the Al_{Bulk} surface (**Eq. 32**) and is known as the Rehbinder effect. Without the protective oxide layer, the potential get shifted towards that of pure Al [197].

$$Al_{bulk}(Al_2O_3)_{surface} + Al^{3+} + 2Ga^{3+} + 9e^{-} \rightarrow 2(AlGa)_{ss} + (Al_2O_3)_{diss} \quad (32)$$

In this chapter, the activation of the Al-foil and suppression of the parasitic corrosion are the main focus of developing an Al alloy as a negative electrode for RABs. *Via* the mixing of different amounts of metallic Ga with Al-foil (*ex-situ* method) and the addition of different $GaCl_3$ content to the $AlCl_3$:EMImCl (1.5:1) ionic liquid electrolyte (*in-situ* method), an AlGa alloy negative electrode is prepared to obtain a stable interface between the electrode and the ionic liquid electrolytes. The active AlGa negative electrode is expected to show several advantages, such as the removal of the insulating and protective Al_2O_3 layer and the initiation of Al growth that will no longer be limited to defects on the Al surface. Instead, Al should grow over the amorphous boundaries everywhere, which reduces the possibility of dendrite growth and formation of inactive Al. Thus, there is interest in understanding the role of Ga as an activating addition and the possible adventitious influence on the electrochemistry of RABs.

6.2 Results and Discussions

First of all, the *ex-situ* method was used to fabricate AlGa alloys with different mass ratios between both metals. The focus was on the preparation of the following mass ratios: $Al_{10}Ga_{90}$, $Al_{20}Ga80$, $Al_{30}Ga_{70}$ and $Al_{40}Ga_{60}$. Higher Al- *and vice versa* lower Ga-content ($Al_{40+x}Ga_{60-x}$; x=10, 20, 30, 40 and 50) would not result in the formation of a semisolid AlGa alloy but a solidified compound with small unreacted remaining Al fragments on the surface [195]. Only a semisolid amalgam-like interface on the negative electrode can go through a self-healing

process to repair formed cracks, pits and other surface damages [198]. After the preparation of the Al_yGa_x (y=10, 20, 30, 40 and x=90, 80, 70, 60, respectively) alloys, two significant challenges appeared: (I) By the naked eye, it is visible that the Al_yGa_x electrode does not have a homogeneous distribution of Al and Ga metal. Scanning electron microscopy (SEM) images (**Figure 29 A-D**) confirm the unequal surface conditions. Moreover, the surface of the electrode is not smooth and the thickness varies (1.52±0.62 mm) all around the alloy. (II) The average weight of the AlGa electrodes (1.131 cm^2) is 121±15 mg. To obtain round electrodes, the mixed metals were heated to 50°C and poured into a 12 mm diameter round shape body. Afterwards, the alloys were allowed to cool down in a refrigerator at 0°C for 12 hours.

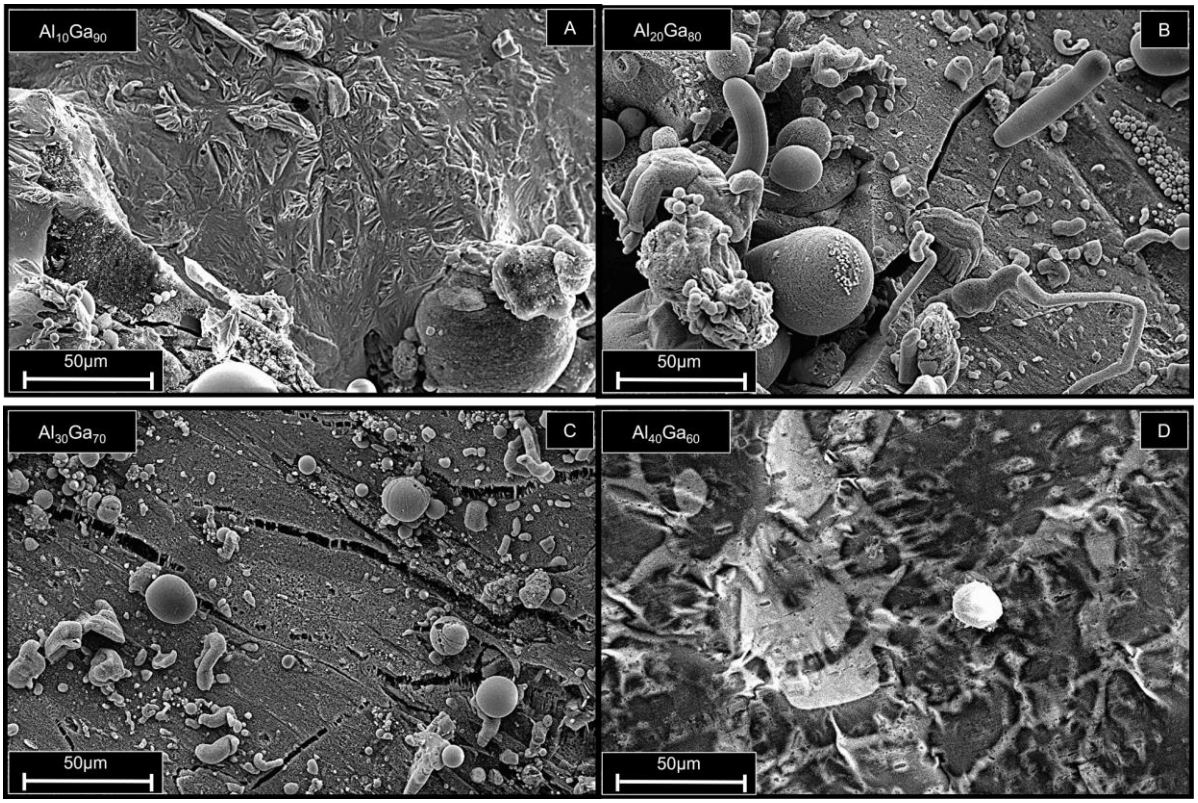

Figure 29 Scanning electron microscopy (SEM) images of (A) $Al_{10}Ga_{90}$, (B) $Al_{20}Ga_{80}$, (C) $Al_{30}Ga_{70}$ and (D) $Al_{40}Ga_{60}$ alloys at a zoom of 50 µm.

Both, the non-homogeneous distribution of Al/Ga and the heavy uneven electrode result in several disadvantages, generally in Metal-Ion Batteries (MIBs). For instance, a non-uniform surface and thickness of the metallic negative electrode can result in a worse electrode/electrolyte interface, leading to increased interfacial resistance [199]. Moreover, due to the non-homogeneous distribution of both metals inside the alloy, Al electroplating will occur on preferred active sites because of the decreased deposition interface [200]. As a result, high-volume expansion and the growth of dendrites can occur and cause a short circuit. All

these aspects contribute to low specific capacities and low cycling stability, fast capacity decay and decreased rate capabilities, which end with a short cell lifetime. In total, the formation of AlGa alloys by the *ex-situ* method is unsuitable for generating a stable negative electrode for use in $AlCl_3$-based RABs. Therefore, the *in-situ* fabrication method is applied to obtain a smooth protective and self-healing AlGa surface on the Al-foil. For this purpose, different molar ratios of $GaCl_3$ (0.1 M, 0.2 M, 0.3 M and 0.5 M) salt were added to the prepared $AlCl_3$:EMImCl (1.5:1) ionic liquid electrolyte. After adding $GaCl_3$ salt into the electrolyte, it was found that mere contact between modified electrolytes and the Al-foil is sufficient to form an AlGa alloy (**Fig. S5**), which is in agreement with the enrichment of the $(AlGa)_{ss}$ on the Al-foil surface (**Eq. 29**). In the case of the $AlCl_3$:EMImCl:$GaCl_3$ electrolytes, the following reaction is occurring (**Eq. 33**).

$$2Al + GaCl_4^- \rightarrow (AlGa)_{ss} + AlCl_4^- \qquad (33)$$

The formation of the more Lewis acidic $Ga_2Cl_7^-$ species, which could run the alloying process with Al-foil too, can be excluded because of the low molar ratio of added $GaCl_3$ (0.1 M, 0.2 M, 0.3 M, 0.5 M) salt. The pristine Al-foils remain intact but lose their ductility in contact with $GaCl_3$ containing electrolytes. As a result, the foils immediately break under mechanical force. This finding raises the question of whether Al can be used as a reference electrode. To prove the stability of Al as a reference electrode, open circuit voltage (OCV) for at least 70 hours (**Fig. 30 A**) was recorded in an Al-Graphite two-cell configuration with pure $AlCl_3$:EMImCl (1.5:1) and $GaCl_3$:EMImCl (1.5:1) as well as for modified $AlCl_3$-based electrolytes with a content of 0.1M, 0.2M, 0.3M and 0.5M $GaCl_3$, respectively.

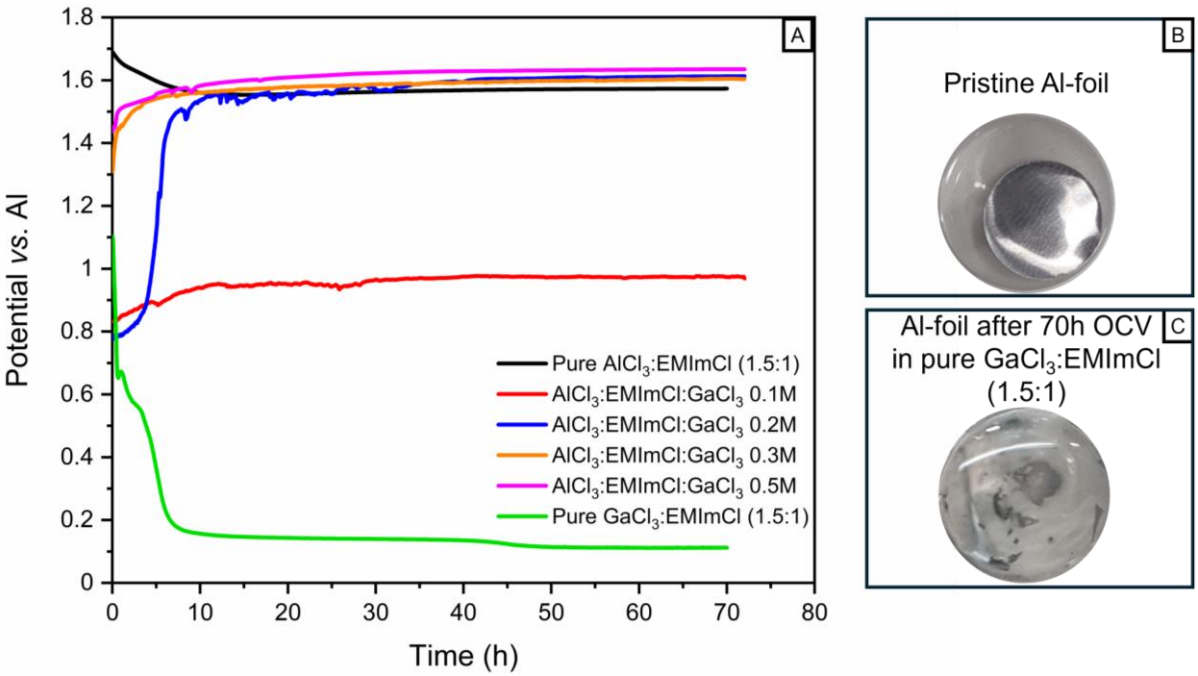

Figure 30 Open circuit voltage (OCV) of pure $AlCl_3$:EMImCl (black) and pure $GaCl_3$:EMImCl (green) ionic liquids in the molar ratio of 1.5:1, respectively. In addition, the OCVs of added $GaCl_3$ content with the molar ratio of 0.1M (red), 0.2M (blue), 0.3M (orange) and 0.5M (pink), respectively. B) Pristine Al-foil and C) Al-foil after 70 h OCV in Lewis acidic $GaCl_3$:EMImCl (1.5:1) electrolyte.

Carpenter and Verbrugge [201] reported that Ga electrodes and Al-wire reference quickly dissolve in acidic $GaCl_3$:EMImCl (molar ratio not reported) ionic liquid. However, in a basic $GaCl_3$:EMImCl (0.67:1) electrolyte, the dissolution of Al was negligible for 24 hours and showed a stable potential *vs.* Al. Similar results are visible in **Figure 30 A-C**, the green curve represents the pure Lewis acidic $GaCl_3$:EMImCl (1.5:1) electrolyte with constantly decreasing potential *vs.* Al. The instability of Al in a $GaCl_3$-based harsh Lewis acidic environment leads to the dissolution of the Al-foil, which is related to the high corrosivity of the ionic liquid and the difference in standard electrode potential ($\Delta E^0_{Al\text{-}Ga}$) *versus* hydrogen ($H_2$). Since Al ($E^0_{Al}$= -1.667 V) has a lower redox potential compared to Ga (E^0_{Ga}= -0.549 V), the Al-foil gets oxidized while Ga^{3+} gets reduced due to the ability to take electrons (e^-). The corresponding reactions are shown in **Equation 34-36**. It is worth mentioning that the listed standard potentials of the electrochemical series *vs*. H_2 are obtained in water-based electrolytes.

$$Al^{3+} + 3e^- \rightleftharpoons Al\ (E^0_{Al} = -1.667\ V) \quad (34)$$

$$Ga^{3+} + 3e^- \rightleftharpoons Ga\ (E^0_{Ga} = -0.549\ V) \quad (35)$$

$$Al + Ga^{3+} \rightarrow Al^{3+} + Ga\ (\Delta E^0_{Al-Ga} = -1.118\ V) \quad (36)$$

Bakkar and Neubert [202] demonstrated that Ga electrodes dissolve in $AlCl_3$:EMImCl (1.5:1) ionic liquid as well. *Via* immersion experiments, the dissolution rate of an 80x10x3 mm strip-shaped solid Ga electrode was measured to be 85 $\mu g \cdot cm^{-2} \cdot h^{-1}$ in 50 ml electrolyte [202]. In a liquid state of Ga (m= ~0.58 g), the dissolution rate is reported to be 1.5 $mmol \cdot ml^{-1}$ equal to ~105 $mg \cdot ml^{-1}$ in $AlCl_3$:EMImCl (1.3:1) [16]. This result shows that the concentration of $GaCl_3$ in the electrolyte must be kept low to activate the negative electrode without dissolving both, the Al-foil and Ga content. On the other hand, a low amount of $GaCl_3$ additive seems to influence the cells negatively as well. With a content of 0.1 M $GaCl_3$, the OCV reaches ~0.9 V *vs.* Al and the electrolyte with 0.2 M $GaCl_3$ concentration shows an increase in potential in the first 10 hours and for further ca. 25 hours an unstable potential before reaching a constant value of ~1.6 V *vs.* Al, which is the regular OCV potential in Graphite-based RABs. Pure $AlCl_3$:EMImCl ionic liquid electrolyte, as well as those with 0.3 M and 0.5 M $GaCl_3$ content, needs around 10 hours to stabilize at ~1.6 V. Following three reasons can cause this behaviour: (I) Complete wetting of all electrodes, (II) entirely soaking of the separator and (III) removal of the Al_2O_3 layer by galvanic corrosion due to $Al_2Cl_7^-$ and the formation of AlGa alloy on the surface. Since it is possible to reach a stable OCV, Al will further be used as a quasi stable reference electrode (QSRE) for all electrochemical measurements. Al as QSRE will be used to have a direct comparison of results, produced under similar conditions, as Carpenter / Verbrugge [201] and Bakkar / Neubert [202]. First of all, the current contribution of the electroplating of Al and the formation of the AlGa alloy was investigated. Cyclic voltammetry (CV) of Al-symmetric cells at varying sweep rates (5, 10, 20 and 30 $mV \cdot s^{-1}$) are performed for $AlCl_3$:EMImCl, $AlCl_3$-based ionic liquid with 0.1 M, 0.2 M, 0.3 M and 0.5 M $GaCl_3$ additive and pure $GaCl_3$:EMImCl (1.5:1) electrolytes (**Fig. 31 A1-F1**). **Figure 31 A2-F2** shows the calculated contribution of surface-controlled nucleation and diffusion-controlled growth.

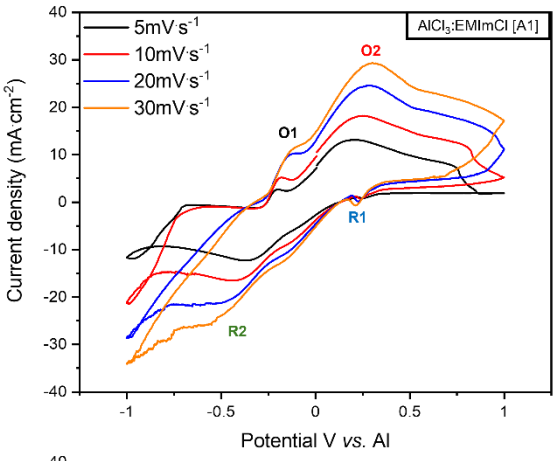
AlCl3:EMImCl [A1]
5mV·s-1
10mV·s-1
20mV·s-1
30mV·s-1
O1
O2
R1
R2
Current density (mA·cm-2)
Potential V vs. Al

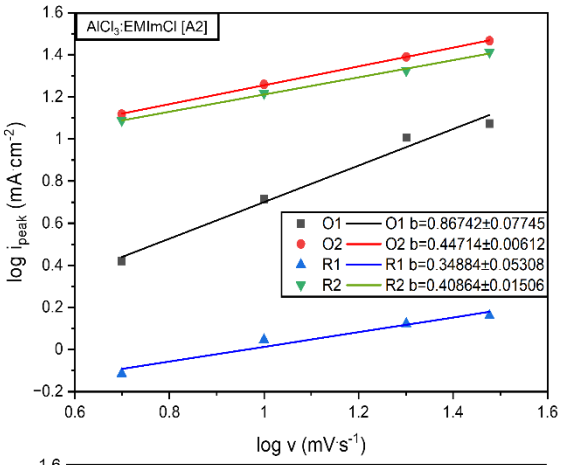
AlCl3:EMImCl [A2]
O1 O1 b=0.86742±0.07745
O2 O2 b=0.44714±0.00612
R1 R1 b=0.34884±0.05308
R2 R2 b=0.40864±0.01506
log ipeak (mA cm-2)
log v (mV·s-1)

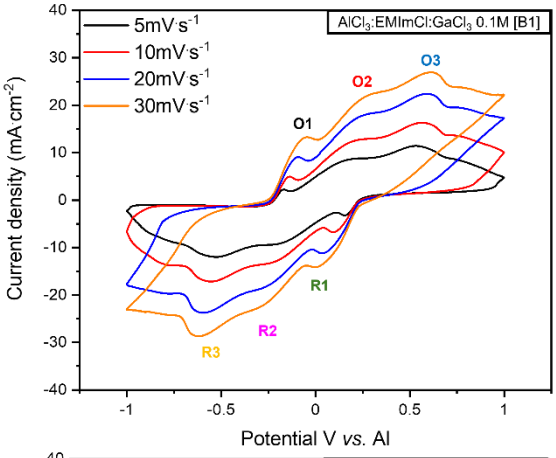
AlCl3:EMImCl:GaCl3 0.1M [B1]
5mV·s-1
10mV·s-1
20mV·s-1
30mV·s-1
O1
O2
O3
R1
R2
R3
Current density (mA·cm-2)
Potential V vs. Al

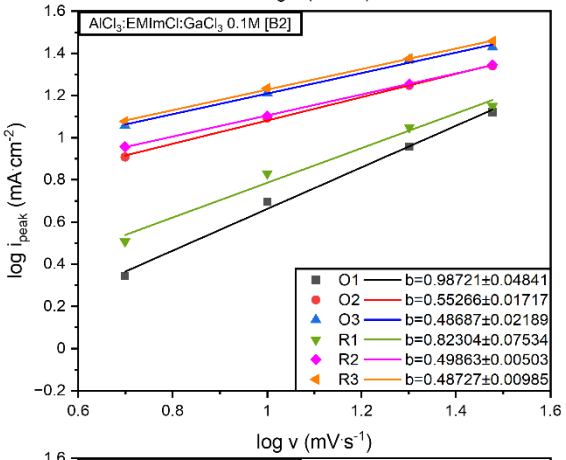
AlCl3:EMImCl:GaCl3 0.1M [B2]
O1 b=0.98721±0.04841
O2 b=0.55266±0.01717
O3 b=0.48687±0.02189
R1 b=0.82304±0.07534
R2 b=0.49863±0.00503
R3 b=0.48727±0.00985
log ipeak (mA cm-2)
log v (mV·s-1)

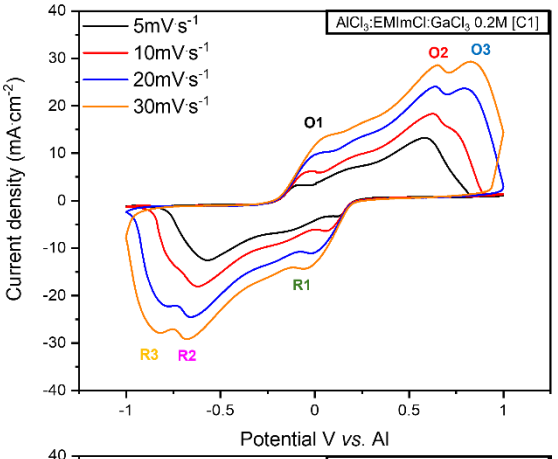
AlCl3:EMImCl:GaCl3 0.2M [C1]
5mV·s-1
10mV·s-1
20mV·s-1
30mV·s-1
O1
O2
O3
R1
R2
R3
Current density (mA·cm-2)
Potential V vs. Al

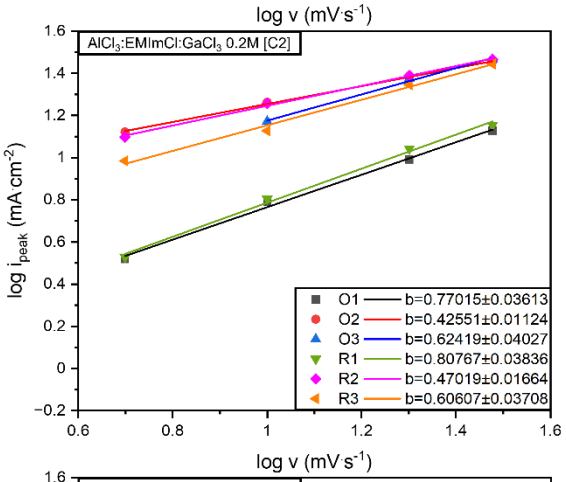
AlCl3:EMImCl:GaCl3 0.2M [C2]
O1 b=0.77015±0.03613
O2 b=0.42551±0.01124
O3 b=0.62419±0.04027
R1 b=0.80767±0.03836
R2 b=0.47019±0.01664
R3 b=0.60607±0.03708
log ipeak (mA cm-2)
log v (mV·s-1)

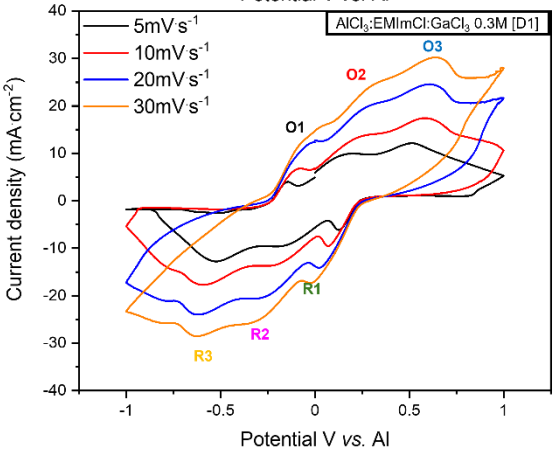
AlCl3:EMImCl:GaCl3 0.3M [D1]
5mV·s-1
10mV·s-1
20mV·s-1
30mV·s-1
O1
O2
O3
R1
R2
R3
Current density (mA·cm-2)
Potential V vs. Al

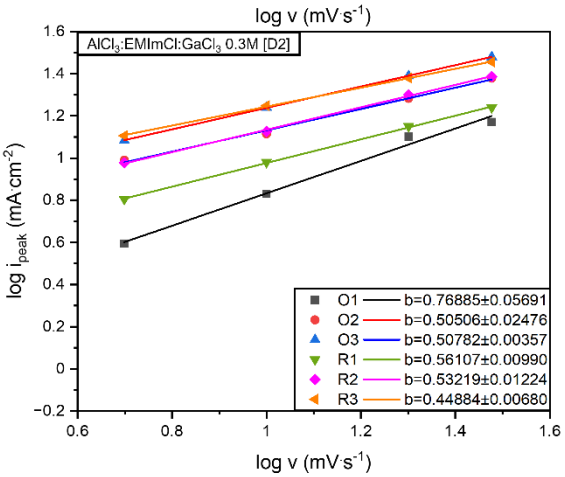
AlCl3:EMImCl:GaCl3 0.3M [D2]
O1 b=0.76885±0.05691
O2 b=0.50506±0.02476
O3 b=0.50782±0.00357
R1 b=0.56107±0.00990
R2 b=0.53219±0.01224
R3 b=0.44884±0.00680
log ipeak (mA cm-2)
log v (mV·s-1)

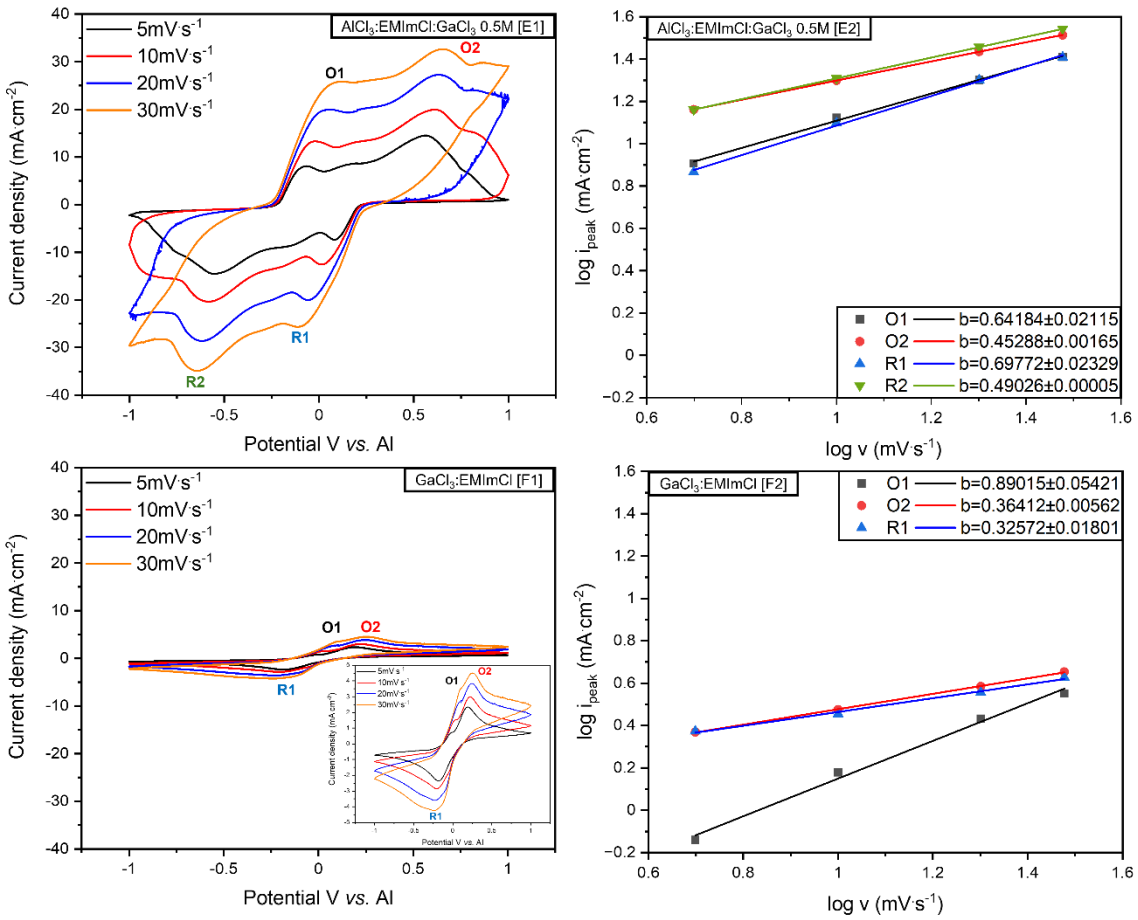

Figure 31 Cyclic voltammograms (CVs) of $AlCl_3$:EMImCl (**A1**), $AlCl_3$:EMImCl:$GaCl_3$ 0.1M (**B1**), $AlCl_3$:EMImCl:$GaCl_3$ 0.2M (**C1**), $AlCl_3$:EMImCl:$GaCl_3$ 0.3M (**D1**), $AlCl_3$:EMImCl:$GaCl_3$ 0.5M (**E1**) and $GaCl_3$:EMImCl (**F1**) at 5, 10, 20 and 30 $mV \cdot s^{-1}$. **A2-F2** plots show the corresponding log(i_{peak}) *vs.* log(v) diagrams for determining slope b, respectively.

The peak current densities (i_{peak}) of CV and the scan rate (v) follow a power law relation, given by $i = a \cdot v^b$; where a and b are adjustable parameters, which are calculated from the linear plot of log*(i) vs.* log*(v)*. If the value of b is around 0.5, the process is a diffusion-controlled growth, while b~1.0 indicates a surface-controlled nucleation of Al metal or AlGa alloy. The diffusion-controlled growth dominates the electrodeposition of Al [203] (**Fig. 31 A2**) and Ga [204] (**Fig. 31 F2**), while the electroplating of the AlGa alloy includes a certain part of kinetically controlled electrode surface reactions. Complementary results have been achieved for the co-deposition of Ga-Se (selenium) [205], Ga-Ni (nickel) [206] and Al-Mn [207] alloys. Similar to the Ga-Ni [206], it is assumed that initially an interface reaction leads to the formation of an AlGa surface, like it is shown by Breslin [196] and Reboul [197] (**Eq. 29-32**). Due to the emergence of AlGa, the electrode surface becomes amorphous and porous, which causes a higher surface area

for the nucleation sites, resulting in a diffusion-controlled process. With the newly formed AlGa surface, the negative electrode is considered activated due to the removed dielectric Al_2O_3 layer [208,209]. Therefore, the electrochemical properties of the activated anode material have been tested in an Al-Graphite two-cell configuration by CV with a scan rate of 0.1 $mV \cdot s^{-1}$ (**Fig. 32 A1-F1**), galvanostatic cycling with potential limitation (GCPL) at a current density of 20 $mA \cdot g^{-1}$ (**Fig. 32 A2-F2**) and rate tests with 20, 50, 100, 200, 500 and 1000 $mA \cdot g^{-1}$ before returning to the initial current density of 20 $mA \cdot g^{-1}$ and 10 $mA \cdot g^{-1}$ (**Fig. 32 A3-F3**). The 100 GCPL cycles were carried out after the CV recording followed by the rate tests. This was done to activate the system and to make sure that the alloying of the Al with Ga was successful for generating a stable Al/AlGa QSRE. All electrochemical tests have been done with an Al-Graphite two-electrode cell configuration in the potential window 0.3-2.3 V *vs.* Al. Cyclic voltammetry was performed on Al-Graphite cells to elucidate further insights into the electrochemical differences among $GaCl_3$ additives in the ionic liquid electrolyte. Three major facts are visible in the CV measurements: (I) Compared to the $AlCl_3$:EMImCl, the ionic liquids with 0.1 M, 0.2 M, 0.3 M and 0.5 M $GaCl_3$ additive show a shift of the anodic and cathodic peaks towards lower potential (**Fig. 32 A1-E1**). This is probably caused by the change of the QSRE electrode from pure Al to AlGa, however, after a few cycles all peaks do not shift anymore and are reversible; (II) With increasing $GaCl_3$ amount, a sharp increase of oxidative current occurs (**Fig. 32 A1-E1**) which is associated with irreversible electrochemical reactions [210]. On the other hand, pure $AlCl_3$ and $GaCl_3$ (**Fig. 32 A1** and **F1**) ionic liquids do not show an anodic peak around 2.3 V; (III) The CV of $GaCl_3$:EMImCl (**Fig. 32 F1**) electrolyte is not stable and therefore stopped after 5 cycles to avoid cell collapse to continue with the GCPL and rate tests. For direct comparison of the $GaCl_3$ additive on the capacities and stabilities, pure $AlCl_3$:EMImCl ionic liquid electrolyte was measured at a current density of 20 $mA \cdot g^{-1}$. After 100 cycles, a specific discharge capacity of circa 52 $mAh \cdot g^{-1}$ is obtained at an average CE of ~98.5% (**Fig. 32 B1**). With further cycle number, the discharge capacity slightly increases, probably due to the activation of the negative electrode [71,184], expansion of Graphite interlayers [171] and the decomposition of polyvinylidene fluoride (PVdF) binder into amorphous carbon and the formation of AlF_4^- [34]. With increasing $GaCl_3$ content, the initial specific discharge capacity increases, while the CE is worse than in pure $AlCl_3$:EMImCl ionic liquid, resulting in lower cyclability after 100 cycles. In detail, the $AlCl_3$:EMImCl:$GaCl_3$ 0.1 M electrolyte Al-Graphite cell shows an initial specific capacity of around 61 $mAh \cdot g^{-1}$ and drops to 54 $mAh \cdot g^{-1}$, which is a loss of 11.48% and a CE of circa 94.7%. With an amount of 0.2 M $GaCl_3$, it is possible to reach in the first cycle ~61 $mAh \cdot g^{-1}$. After 100 cycles, the capacity

dropped to ~56 $mAh \cdot g^{-1}$ (loss of 8.2%) with an average CE of ~97%. In the case of $AlCl_3$:EMImCl:$GaCl_3$ 0.3M electrolyte, the initial discharge capacity of ~67 $mAh \cdot g^{-1}$ was reached again after 100 cycles. However, the CE in this system is only around 93%. The electrolyte with 0.5 M $GaCl_3$ showed an average initial specific discharge of circa 73 $mAh \cdot g^{-1}$, dropping 13.7% to ~63 $mAh \cdot g^{-1}$ with a CE of ~91%. Last, but not least, the GCPL of pure $GaCl_3$:EMImCl ionic liquid electrolytes was investigated. The first charge of the pure $GaCl_3$-based electrolyte confirms the instability of the system, which was already visible in the CV measurements. The capacity at different cycle numbers is always below 30 $mAh \cdot g^{-1}$ with an average CE of 79%. The relatively high CE is because the cell was stable for a certain time (cycle 18-65). Subsequent measured rate tests show a general trend too. Compared to the pure $AlCl_3$:EMImCl ionic liquid, all electrolytes with $GaCl_3$ additive show increased cycle stability at higher current densities. Especially at 200, 500 and 1000 $mA \cdot g^{-1}$ nearly no capacity loss is observed and the CE rises to ≥99%. Superior to the pure Al, the AlGa negative electrodes even show higher discharge capacities with minimal increase of voltage polarization, which originates from the fast reaction kinetics enabled by alloying of Ga with Al. Similar results are reported for an Al-Zn negative electrode in aqueous Al batteries [211]. After returning to the starting specific current of 20 $mA \cdot g^{-1}$, all cells reach the initial capacities. However, a lower current density (10 $mA \cdot g^{-1}$) leads to just a slightly higher specific capacity with an increasing overpotential and lower CE of the $GaCl_3$-containing cells. In the case of the $GaCl_3$:EMImCl ionic liquid, the specific discharge capacity dropped stepwise up to ~4 $mAh \cdot g^{-1}$. If the content of $GaCl_3$ is too high, the formation of AlGa on the surface of the negative electrode is impeded and the diffusion of Ga into the Al matrix becomes dominant. In that case, Al dissolution is obtained due to grain boundary attack and disintegration of the Al-foil [212]. After 145 cycles, the Al negative electrode was nearly completely dissolved, as shown in **Figure 30 C** after 70 h of OCV, which explains the poor electrochemical performance of this cell. On the other hand, 150 cycles in the $AlCl_3$:EMImCl and 0.1 M, 0.2 M, 0.3 M and 0.5 M $GaCl_3$- based electrolytes did not lead to the dissolution of the Al electrode.

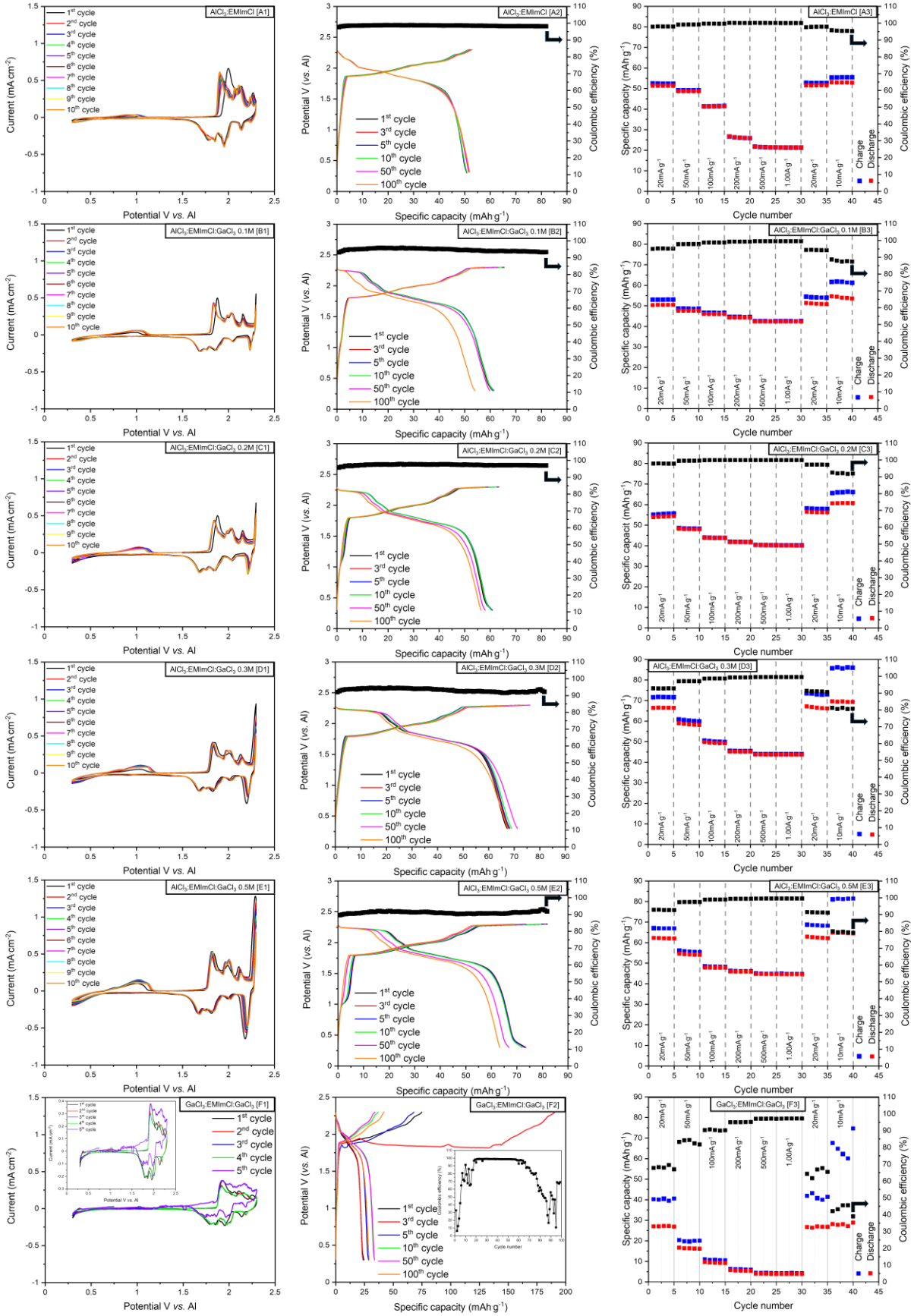
AlCl3:EMImCl [A1]
AlCl3:EMImCl [A2]
AlCl3:EMImCl [A3]
AlCl3:EMImCl:GaCl3 0.1M [B1]
AlCl3:EMImCl:GaCl3 0.1M [B2]
AlCl3:EMImCl:GaCl3 0.1M [B3]
AlCl3:EMImCl:GaCl3 0.2M [C1]
AlCl3:EMImCl:GaCl3 0.2M [C2]
AlCl3:EMImCl:GaCl3 0.2M [C3]
AlCl3:EMImCl:GaCl3 0.3M [D1]
AlCl3:EMImCl:GaCl3 0.3M [D2]
AlCl3:EMImCl:GaCl3 0.3M [D3]
AlCl3:EMImCl:GaCl3 0.5M [E1]
AlCl3:EMImCl:GaCl3 0.5M [E2]
AlCl3:EMImCl:GaCl3 0.5M [E3]
GaCl3:EMImCl:GaCl3 [F1]
GaCl3:EMImCl:GaCl3 [F2]
GaCl3:EMImCl:GaCl3 [F3]
1st cycle
2nd cycle
3rd cycle
4th cycle
5th cycle
6th cycle
7th cycle
8th cycle
9th cycle
10th cycle
50th cycle
100th cycle
Current (mA·cm-2)
Potential V vs. Al
Potential V (vs. Al)
Specific capacity (mAh·g-1)
Specific capacity (mAh·g-1)
Coulombic efficiency (%)
Cycle number
20mA·g-1
50mA·g-1
100mA·g-1
200mA·g-1
500mA·g-1
1.00A·g-1
10mA·g-1
Charge
Discharge

Figure 32 Cyclic voltammograms (CVs) of Al-Graphite cells with $AlCl_3$:EMImCl (1.5:1) (**A1**), $AlCl_3$:EMImCl:$GaCl_3$ 0.1M (**B1**), $AlCl_3$:EMImCl:$GaCl_3$ 0.2M (**C1**), $AlCl_3$:EMImCl:$GaCl_3$ 0.3M (**D1**), $AlCl_3$:EMImCl:$GaCl_3$ 0.5M (**E1**) and $GaCl_3$:EMImCl (1.5:1) (**F1**) ionic liquid electrolytes. Galvanostatic cycling with potential limitation (GCPL) with a current density of 20 $mA \cdot g^{-1}$ and the corresponding coulombic efficiency (CE) are shown for all electrolytes in **A2-F2**, respectively. Rate tests at 20, 50, 100, 200, 500, 1000, 20 and 10 $mA \cdot g^{-1}$ are illustrated in **A3-F3**.

After cycling, the morphology changes of the Al negative electrodes were investigated *via* scanning electron microscopy (SEM) and energy-dispersive X-ray spectroscopy (EDS). It is worth mentioning that all $GaCl_3$-containing electrolytes caused a brittleness of the Al-foil and pure $GaCl_3$:EMImCl, resulting in the pulverization of the Al negative electrode. The pure/pristine Al-foil (**Fig. 33 A1-A2**) shows no surface cracks or pits. Merely a kind of lamella structure is visible, which forms during the rolling process of the Al-foil production. In comparison, 12 h of electrode`s soaking in $AlCl_3$:EMImCl:$GaCl_3$ 0.1 M led to crack (**Fig. 33 B1**) and pit (**Fig. 33 B2**) formation on the surface. In the case of cycling in pure $AlCl_3$:EMImCl (1.5:1) ionic liquid electrolyte, the Al-foil suffers from deep cracks and pits. With further cycle number, created cracks and pits would result in pulverization and dendrite formation, followed by loss of inactive "dead"-Al [16]. On the other hand, for the 0.1 M (**Fig. 33 D1-D2**), 0.2 M (**Fig. 33 E1-E2**) and 0.3 M (**Fig. 33 F1-F2**) $GaCl_3$-based ionic liquid electrolytes, the surface has fewer cracks and pits. However, due to the brittleness of the alloyed AlGa, fibres of the SiO_2 separator can penetrate (**Fig. 33 D2**) the surface and get stuck there (**Fig. 33 F1-F2**). Nevertheless, $AlCl_3$:EMImCl:$GaCl_3$ 0.5 M electrolyte completely covers the surface with AlGa and starts aggressive grain boundary penetration, which results in a river-like surface structure (**Fig. 33 G1-G2**) [213]. As mentioned before, the Al-foil cycled in pure $GaCl_3$:EMImCl electrolyte completely pulverizes. The remaining powder seems to consist of pure Ga with a quite smooth morphology (**Fig. 33 H1-H2**) compared to the other Al-foils soaked or cycled in $GaCl_3$-containing ionic liquids. In addition to the SEM results, EDS images (**Fig. 34 A-H**) show the formation of the AlGa alloy on the surface of the Al-foils in contact and after cycling in the corresponding ionic liquid electrolyte systems.

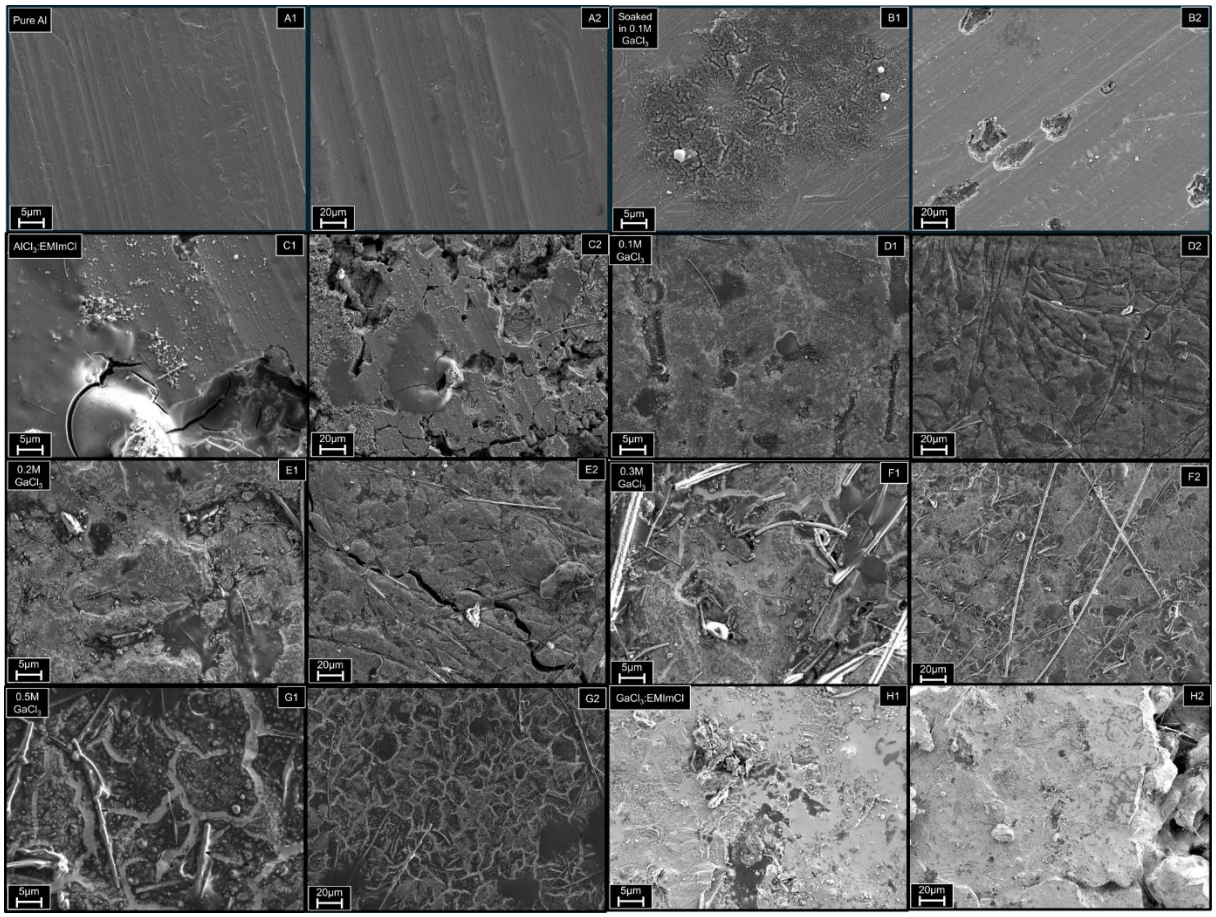

Figure 33 Scanning electron microscopy (SEM) images of Al negative electrodes with a zoom of 5 µm and 20 µm; **A1-A2** pure/pristine Al; **B1-B2** soaked in $AlCl_3$:EMImCl:$GaCl_3$ 0.1 M for 12 h; **C1-C2** cycled in $AlCl_3$:EMImCl (1.5:1); **D1-D2** cycled in $AlCl_3$:EMImCl:$GaCl_3$ 0.1 M; **E1-E2** cycled in $AlCl_3$:EMImCl:$GaCl_3$ 0.2 M; **F1-F2** cycled in $AlCl_3$:EMImCl:$GaCl_3$ 0.3 M; **G1-G2** cycled in $AlCl_3$:EMImCl:$GaCl_3$ 0.5 M and **H1-H2** cycled in $GaCl_3$:EMImCl (1.5:1).

The EDS images of pure/pristine Al (**Fig. 34 A1-A2**), soaked in $GaCl_3$ 0.1 M and cycled negative electrode with $AlCl_3$:EMImCl ionic liquid-based electrolyte (**Fig. 34 B1-B2**), confirm the results of the SEM measurements, **Figure 33 A1-A2**, **B1-B2** and **C1-C2**, respectively. Uncycled/untreated Al-foil shows a lamella surface while cycling with pure $AlCl_3$-electrolyte it forms cracks and pits. In contact with $AlCl_3$:EMImCl:$GaCl_3$ 0.1 M ionic liquid pits are occurring and the Ga inserts on preferred spots/areas (**Fig. 34 C1-C2**). In the case of cycled Al electrodes, the formation of AlGa becomes more dominant with increasing amount of $GaCl_3$ in the electrolytes (0.1 M (**Fig. 34 D1-D3**), 0.2 M (**Fig. 34 E1-E3**) and 0.3 M (**Fig. 34 F1-F3**)). With the highest amount of $GaCl_3$ (0.5 M), the river-like insertion of Ga into the Al grain boundaries [213] is visible and the stuck remaining SiO_2 separator fibers are due to the brittleness

of the AlGa electrode (**Fig. 34 G1-G3**). In pure $GaCl_3$:EMImCl ionic liquid, the pulverized electrode (**Fig. 34 H1-H3**) barely contains remaining Al because of the dissolution initiated by Ga^{3+} reduction (**Eq. 34-36**).

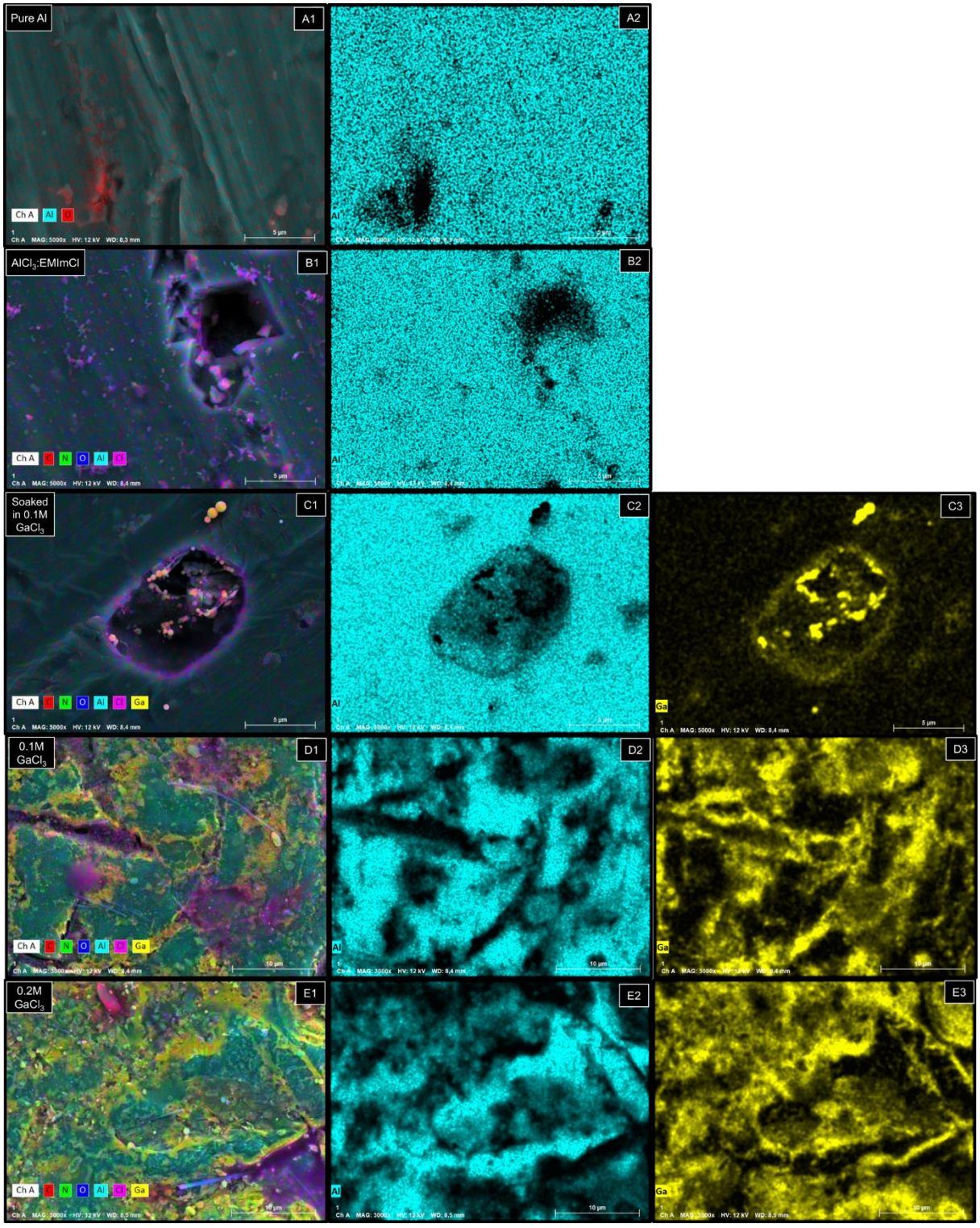

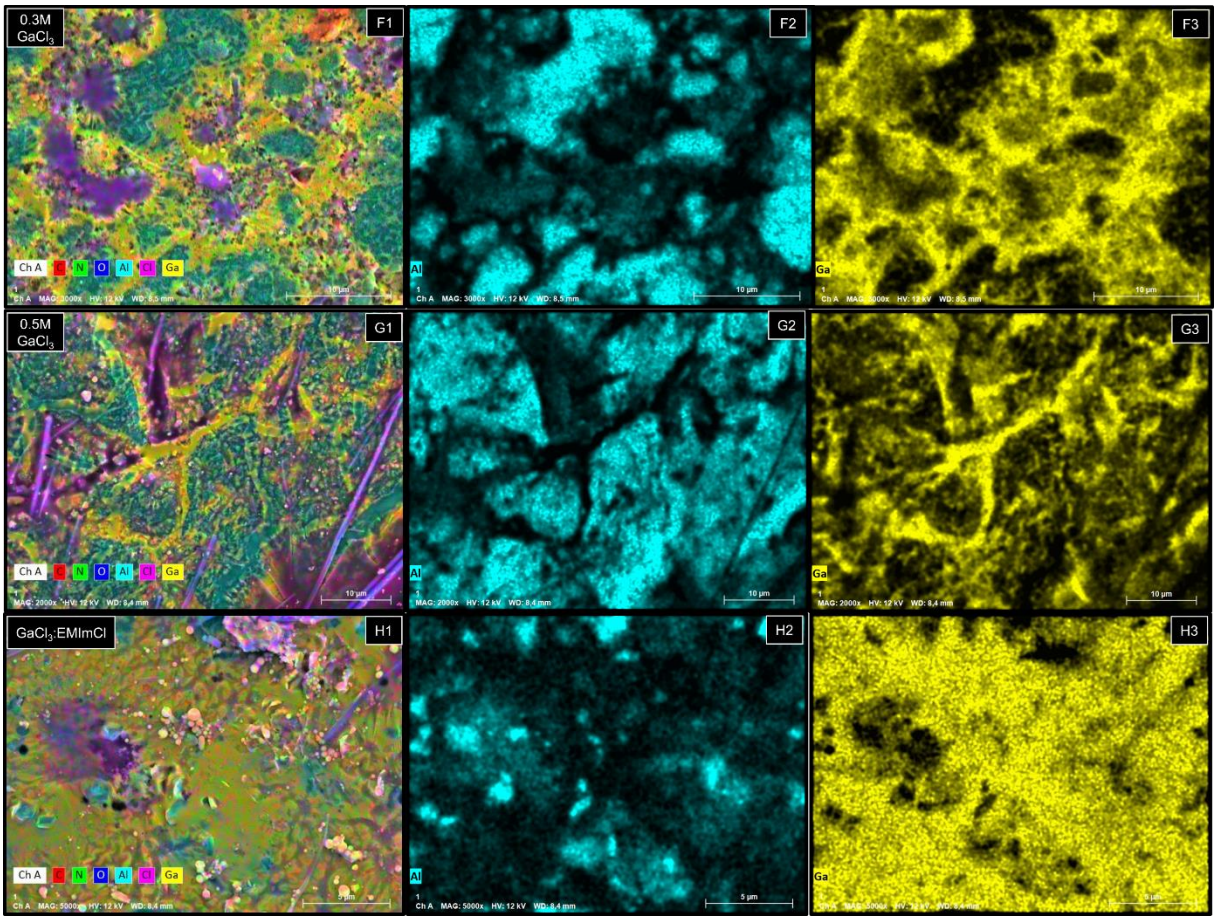

Figure 34 Energy-dispersive X-ray spectroscopy (EDS) images of Al (turquoise coloured) and Ga (gold coloured) after soaking and cycling of Al negative electrode with the corresponding ionic liquid electrolytes. **A1-A2** Pure Al; **B1-B2** Cycled with $AlCl_3$:EMImCl (1.5:1); **C1-C3** Soaked in $AlCl_3$:EMImCl:$GaCl_3$ 0.1 M; **D1-D3** Cycled in $AlCl_3$:EMImCl:$GaCl_3$ 0.1 M; **E1-E3** Cycled in $AlCl_3$:EMImCl:$GaCl_3$ 0.2 M; **F1-F3** Cycled in $AlCl_3$:EMImCl:$GaCl_3$ 0.3 M; **G1-G3** Cycled in $AlCl_3$:EMImCl:$GaCl_3$ 0.5 M and **H1-H3** cycled in $GaCl_3$:EMImCl (1.5:1) ionic liquid electrolyte.

A schematic illustration of the dependence of $GaCl_3/GaCl_4^-$ content in the $AlCl_3$:EMImCl (1.5:1) ionic liquid electrolyte for the formation of AlGa alloys to avoid the repassivation of the Al-foil and the insertion of Ga inside the grain boundaries of Al is shown in **Figure 35 A-D** and supports the obtained SEM (**Fig. 33 B1-G2**) and EDX (**Fig. 34 C1-H3**) results. Moreover, to dissolve the Al_2O_3 protective film and obtain an AlGa layer on the surface, several activation and formation cycles are required to initiate the reversible redox reactions at the negative electrode. Once these activation/formation cycles are complete, the oxidation and reduction peaks in the CVs (**Fig. 32 A1-E1**) become symmetric and fully reversible.

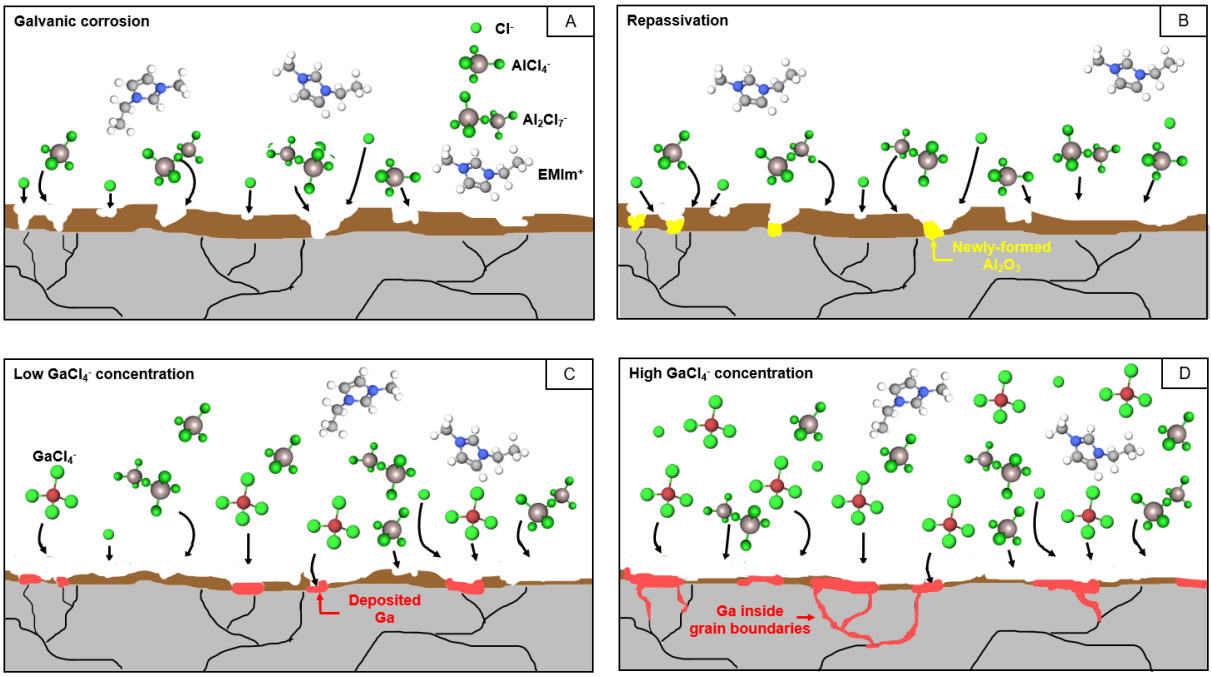

Figure 35 Schematic illustration of galvanic corrosion of the Al_2O_3 layer (A) and repassivation of the Al-foil (B) in pure $AlCl_3$:EMImCl (1.5:1) ionic liquid electrolyte. Deposition of low $GaCl_4^-$ (0.1 M, 0.2 M and 0.3 M) content on the surface for the formation of AlGa and blocking repassivation (C). Insertion of Ga into the grain boundaries of the Al negative electrode at high $GaCl_4^-$ (0.5 M) amount (D).

Furthermore, *ex-situ* extended X-ray absorption fine structure (EXAFS) was performed to track the change of the coordination environment of Ga to Al at different applied potentials, namely charge/electroplating at 2.2 V (**Fig. 36 B1-B3**) and discharge/electrostripping at 0.3 V (**Fig. 36 A1-A3**). The EXAFS signals were detected in fluorescence mode. The magnitude of the Fourier-transforms of the $k^2\chi(k)$ *vs.* distance (R) EXAFS spectra are shown in **Figure S6**.

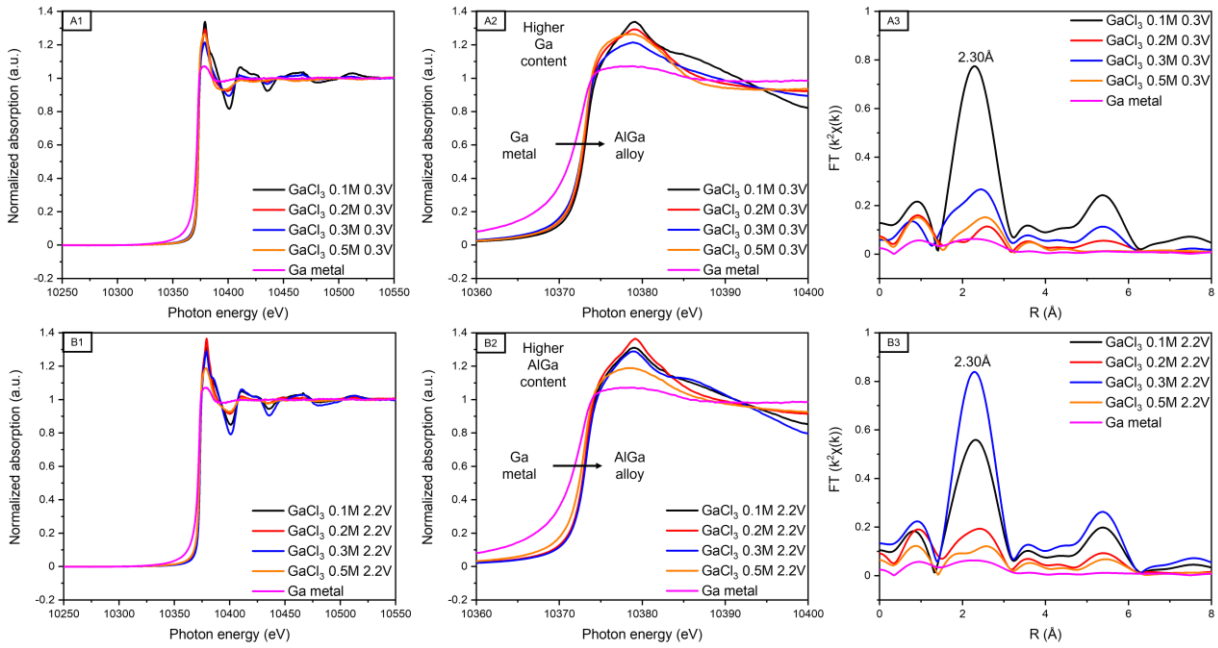

Figure 36 Extended X-ray absorption fine structure spectroscopy (EXAFS) region of Ga metal and negative electrodes cycled with 0.1 M, 0.2 M, 0.3 M, 0.5 M $GaCl_3$ containing electrolytes, stopped at 0.3 V (**A1**) and 2.2 V (**B1**), respectively. **A2** and **B2** show the zoom of the corresponding near-edge X-ray absorption fine structure (NEXAFS) regions. Fourier-transformed *R*-space data of Ga K-edge AlGa alloy electrodes and Ga metal are shown in **A3** and **B3**.

Analysis of the interatomic distances in the main Me-Me shell reveals unusual short values for x<50% (Al_xGa_{1-x}) and the expected value for higher x [214]. The formation of Al-Ga alloys with lower Ga content keeps the 1st magnitude amplitude with high intensity and large Me-Me distance. On the other hand, increased Ga amount in the AlGa alloy leads to decreased Me-Me distance and the amplitude of the magnitude, showing a more distorted structure. Spindlberger *et al.* [214] explain the change in the distance with concentration due to surface effects such as inhomogeneous stress and defects on the surface, like vacancies. This explanation is consistent with the observed initial surface-controlled nucleation of Al during the electroplating process (**Fig. 31 B1-F2**) and the high Ga content on the surface shown by EDS measurements (**Fig. 34 C1-H3**). During the electroplating (2.2 V), the negative electrodes show a higher AlGa content (**Fig. 36 B1-B2**) while the electrostripping (0.3 V) leads to the dealloying of AlGa which results in higher Ga content (**Fig. 36 A1-A2**) on the Al electrode surface. The results for the Me-Me shell, which corresponds to the single scattering with the distance 2.5-2.9 Å, are presented in **Table 4**.

Table 4 Structure parameter of AlGa negative electrodes with the coordination number (*N*), passive electron reduction factor (S_0^2), Debye-Waller factor (σ^2) and the zero-energy shift (ΔE_0), resulting in the first shell interatomic distance (*R*) in Angström (Å).

Molarities and Potential	***N***	S_0^2	σ^2	ΔE_0	ΔR (Å)	R_{eff} (Å)	***R* (Å)**
$GaCl_3$ 0.1M 0.3V	12	0.7	0.018	1.873	-0.068	2.863	2.794
$GaCl_3$ 0.1M 2.2V	12	0.7	0.024	2.457	-0.052	2.863	2.811
$GaCl_3$ 0.2M 0.3V	12	0.7	0.057	-0.919	-0.069	2.863	2.793
$GaCl_3$ 0.2M 2.2V	12	0.7	0.044	2.433	0.009	2.863	2.872
$GaCl_3$ 0.3M 0.3V	12	0.7	0.038	2.925	-0.019	2.863	2.844
$GaCl_3$ 0.3M 2.2V	12	0.7	0.017	2.871	-0.061	2.863	2.802
$GaCl_3$ 0.5M 0.3V	12	0.7	0.066	-5.722	-0.351	2.863	2.512
$GaCl_3$ 0.5M 2.2V	12	0.7	0.073	3.789	0.060	2.863	2.924

The Fourier-transformed *R*-space is illustrated during electroplating in **Figure 36 B3** and electrostripping in **Figure 36 A3**. According to the prototype structure, Al-Al distances, corresponding to the first coordination shell is R_{eff}=2.863 Å. Insertion of Ga in the structure of Al decreases interatomic distances. During the electroplating process at 2.2 V, the Al-rich alloy is obtained on the Al-foil surface. The opposite effect occurs during the electrostripping (0.3 V), which initiates the dealloying process and leads to the enrichment of metallic Ga on the negative electrode. Besides the impact of $GaCl_3$ additive in the $AlCl_3$:EMImCl (1.5:1) ionic liquid electrolyte on the negative electrode, *ex-situ* X-ray diffraction (XRD) was recorded from the hexagonally structured Graphite positive electrodes with the space group $P6_3/mmc$ (ICSD 18838). **Figure 37** (black reflection) shows the reflection peak of pristine Graphite, indexed as 002, which can be used for the calculation of interlayer distance (3.35 Å) [215]. It is notable that at voltages along the charging plateau, each of the 002 XRD reflections evolved by gradually vanishing its intensity and the appearance of two new peaks [74].

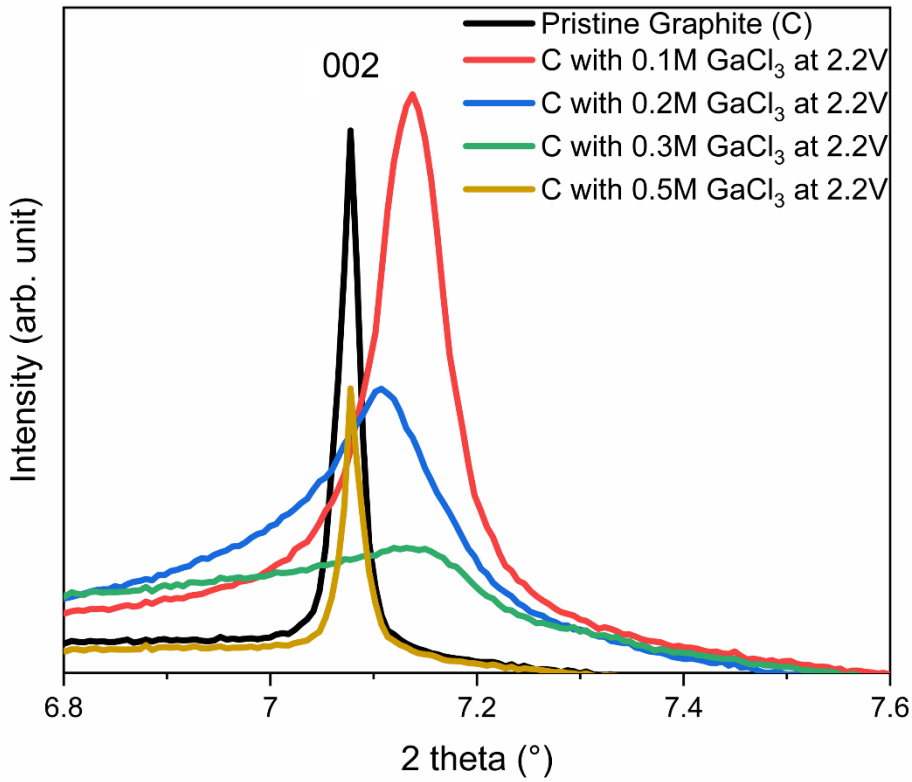

Figure 37 Synchrotron X-ray diffraction (XRD) pattern of 002 reflection peak of pristine Graphite (black) and charged Graphite positive electrodes with increasing $GaCl_3$ (0.1 M; red, 0.2 M; blue, 0.3 M; green and 0.5 M; light-brown, respectively) additive in the ionic $AlCl_3$:EMImCl (1.5:1) liquid electrolyte.

In the XRD pattern, one of the new peaks is covered by diffraction reflections of Kapton foil in the small angle region. The amorphization of the main 002 reflection can be evidence for the $AlCl_4^-/GaCl_4^-$ intercalation [74], whereby the peak intensity of the samples with increasing $GaCl_3$ content (0.1 M → 0.2 M → 0.3 M) is gradually decreasing. However, no 002 reflection peak shift (**Fig. 37**, light-brown) appears in the case of the highest amount of 0.5 M $GaCl_3$ additive. The reduced intensity of the 002 peak, compared to the pristine Graphite, indicates a decreased structural order of the Graphite during charging, likely due to the formation of a turbostatic structure [216]. Moreover, this phenomenon seems to be influenced mostly by surface-controlled processes that can improve the rate capability of the Ga-containing samples, as demonstrated in **Figure 32 B3-F3**. To sum up: The addition of small amounts (0.1 M, 0.2 M, 0.3 M and 0.5 M) of $GaCl_3$ into $AlCl_3$:EMImCl (1.5:1) ionic liquid electrolyte leads to the formation of AlGa, which can be seen as an activated negative electrode due to the removal of the insulating Al_2O_3 layer. It was possible to demonstrate that during the electroplating, the formation of AlGa

occurs, while the electrostripping leads to the dealloying whereby Al is released and Ga remains on the electrode surface. The new modified negative electrode runs during the electroplating through an initial surface-controlled nucleation process, which turns into a diffusion-controlled growth. SEM and EDX images confirm a more stable surface after cycling with $GaCl_3$-containing electrolytes compared to the pure $AlCl_3$-based ionic liquid. However, pure $GaCl_3$:EMImCl (1.5:1) ionic liquid electrolyte results in a dissolution of the Al-foil electrode, because Ga is more noble than Al. Last, but not least, a low $GaCl_3$ additive in the ionic liquid electrolyte results in higher specific capacities but lower cyclability over time. Nevertheless, higher stability at higher current densities was obtained without the formation of dendrites. The increased rate capability could be caused by the formation of turbostatic structure of the Graphite during charging, whereby the 002 reflection peak does not shift but loses intensity.

6.3 Conclusion

If the ionic liquid electrolyte contains Ga^{3+}-ions, it is possible to form *in-situ* an Al-Ga alloy with the Al negative electrode. According to the mechanism of Dual-Ion Batteries (DIBs), when the potential of Graphite reaches 2.2 V, the potential of Al goes down, corresponding to the electroplating process. It has been found that during electroplating, the formed alloy preferably consists of Al, while during electrostripping, most of Ga remains on the surface. It seems that Ga creates a film on the Al surface that has a greater impact on the surface-controlled mechanism. Moreover, the $GaCl_3$ additive causes a more stable electrochemical performance at higher current densities. However, since the newly formed AlGa negative electrodes are brittle, *ex-situ* or *post-mortem* analysis becomes more difficult, which hampers the ability of further investigations. In addition, $GaCl_3$-based ionic liquid electrolytes and formed metallic Ga can alloy with nearly all metals. By this, the choice of suitable cell body parts is limited to W, tantalum (Ta) or non-metallic components like glass or PFA. Additional precautions to protect devices must be considered to avoid damages in case of a cell leakage. Therefore, the formation of AlGa to obtain a more resistant negative electrode for RABs is just of academic interest.

6.4 Outlook and Future Work

For the first time, it has been shown that the formation of an *in-situ* AlGa aluminophilic alloy interphase/interface increases the stability of the negative electrode and results in raised rate capability in Graphite-based RABs. Compared to pure Al-foil in $AlCl_3$:EMImCl (1.5:1) ionic liquid electrolyte, fewer cracks and pits are formed on the surface during cycling. Maybe it would be even more beneficial to run the first several initial cycles with the $GaCl_3$-containing

electrolytes to obtain the formation of an AlGa alloy surface layer and afterwards exchange the electrolyte to the standard $AlCl_3$:EMImCl (1.5:1) IL electrolyte. Nevertheless, after the lifespan of the AlGa-Graphite cells has expired, the formed alloy can still be further used for the generation of H_2 coupled with Ga recycling. Both, Yu *et al.* [195] and Amberchan *et al.* [217] describe the recovery of Ga as follows: At ambient atmosphere, the AlGa alloy was added into water (H_2O), whereby the activated Al generate H_2, aluminum(III)-hydroxide ($Al(OH)_3$) and metallic Ga (**Eq. 37**).

$$2Al_{activated}Ga + 6H_2O \rightarrow 3H_2 + 2Al(OH)_3 + 2Ga \qquad (37)$$

After the reaction (**Eq. 37**) is complete, residual Al will float on the top of the water, while Ga, due to higher density, will precipitate. The flask containing water, Al and Ga, needs to be boiled to achieve aggregation of the liquid Ga beads. Afterwards, there are two options to obtain Ga: (I) The liquid metal can be removed by a syringe or (II) by cooling down the H_2O until Ga solidifies and can be filtrated. This process provides H_2, which can be used for further generation of energy [3] and to recover >95% [217] of Ga, which can be re-used and result in an economic and environmental advantage. An interesting new approach would be to investigate an Al-Galinstan (an alloy made of 66.5 w(%) Ga, 20.5 w(%) In (indium) and 13.0 w(%) Sn (tin)) [218] as a negative electrode in RABs. Similar to pure Ga, Galinstan is well known to dissolve insulating Al_2O_3 on the electrode's surface and, therefore, responsible for the activation of Al. As mentioned in the introduction part, additional inactive components inside the alloys can act as a stabilizing lattice matrix to avoid a structural collapse of the negative electrode. At this point, it would be necessary to prove the stability of the involved In and Sn components of the alloy in Lewis acidic ionic liquid electrolyte. Since Galinstan has a melting point of only 11-13°C [219] (depending on the exact ratio between Ga, In and Sn), the formed Al-Galinstan alloy on the surface of the negative electrode would stay in a liquid state. A liquid surface has the ability of self-healing to avoid cracks, pits, formation of dendrites and inactive Al. Jiao *et al.* [16] utilized pure liquid Ga as negative electrode, with carbon paper as the positive electrode in an $AlCl_3$:EMImCl (1.3:1) ionic liquid electrolyte. The liquid Ga is able to reversibly form an AlGa alloy with the $Al_2Cl_7^-$ complex of the electrolyte (**Eq. 38**).

$$xGa + 4Al_2Cl_7^- + 3e^- \rightleftharpoons AlGa_x + 7AlCl_4^- \qquad (38)$$

Due to the self-healing of the liquid metal, all above mentioned destructive processes of the negative electrode could be avoided [16]. Similar results could be achieved in the case of an *in-situ* formed Al-Galinstan alloy and in addition, it is possible to generate H_2 and recover and re-use Ga after cell collapse.

7. Scientific contributions

7.1 Publications as the first author

E. Zemlyanushin, A. Sarapulova, T. Tsuda, S. Dsoke, Impact of Gallium chloride Additive in Lewis acidic ionic liquid electrolytes for Rechargeable Aluminum-Batteries, Desired journal: *J. Alloys Compd.*, **2025**, manuscript under preparation.

E. Zemlyanushin, B. Schwarz, S. Dsoke, Dissolution of molybdenum current collector as Crucial and Undesired process in aluminum batteries, *J. Power Sources*, **2025**, *633*, 236458. **DOI:** 10.1016/j.jpowsour.2025.236458

E. Zemlyanushin, A.L. Müller, T. Tsuda, S. Dsoke, Side-Reactions of Polyvinylidene fluoride and Polyvinylidene chloride binders with Aluminum chloride-based ionic liquid electrolyte in Rechargeable Aluminum-Batteries, *J. Electrochem. Soc.*, **2024**, *171*, 110507. **DOI:** 10.1149/1945-7111/ad8a93

E. Zemlyanushin, S. Dsoke, ADIBs-current collector and anode corrosion issues, M. Rosa Palacin *et al.*, *J. Phys. Energy*, **2024**, *6 (3)*, 031501. **DOI:** 10.1088/2515-7655/ad34fc

E. Zemlyanushin, K. Pfeifer, A. Sarapulova, M. Etter, H. Ehrenberg, S. Dsoke, Probing the Effect of Titanium Substitution on the Sodium Storage in $Na_3Ni_2BiO_6$ Honeycomb-Type Structure, *Energies*, **2020**, *13 (24)*, 6498. **DOI:** 10.3390/en13246498

7.2 Publications as co-author

E. Fuentes-Mendoza, M. Talari, **E. Zemlyanushin**, R. Cordoba, N. Sabi, S. Dsoke, Navigating the Challenges of Rechargeable Aluminum Batteries: Material Instabilities, Technical Hurdles, and Future Directions, *ChemElectroChem*, **2025**, accepted.

M. Talari, A. Sarapulova, **E. Zemlyanushin**, N. Sabi, A. Hofmann, V. Trouillet, S. Dsoke, Exploring the possibility of aluminum plating/stripping from a non-corrosive $Al(OTF)_3$-based electrolyte, *Batter. Supercaps*, **2024**, e202400317. **DOI**: 10.1002/batt.202400317

B. Schwarz, J. Hansen, A.L. Hansen, **E. Zemlyanushin**, H. Ehrenberg, Structure and magnetic properties of hausmannite α-Mn_3O_4, metastable high-pressure marokite γ-Mn_3O_4, and defected α-Mn_3O_4, *Phys. Rev. B*, **2023**, *108 (1)*, 014417. **DOI:** 10.1103/PhysRevB.108.014417

F. Rahide, **E. Zemlyanushin**, G.M. Bosch, S. Dsoke, Open Challenges on Aluminum Triflate-Based Electrolytes for Aluminum Batteries, *J. Electrochem. Soc.*, **2023**, *170 (3)*, 030546. **DOI:** 10.1149/1945-7111/acc762

8. Conference contribution

E. Zemlyanushin, Interaction of Polyvinylidene fluoride and Polyvinylidene chloride with Aluminum chloride / 1-Ethyl-3-methylimidazolium chloride ionic liquid electrolyte in Rechargeable Aluminum-Batteries, *International Society of Electrochemistry (ISE), 75th Annual Meeting in Montreal (Canada)*, **2024**, 20 minutes Oral presentation.

E. Zemlyanushin, A.L. Müller, T. Tsuda, S. Dsoke, Impact of Polyvinylidene (PVdF) and Polyvinylidene chloride (PVdC) with Aluminum chloride ($AlCl_3$) / 1-Ethyl-3-methylimidazolium chloride (EMImCl) ionic liquid electrolyte in Rechargeable Aluminum-Batteries (RABs), *International Meeting on Lithium Batteries (IMLB 2024), Hong Kong (China)*, **2024**, Poster presentation.

M. Talari, A. Sarapulova, **E. Zemlyanushin**, N. Sabi, A. Hofmann, S. Dsoke, Exploring the Possibility of Aluminum Plating/Stripping from a Non-Corrosive $Al(OTF)_3$-Based Electrolyte, *The Electrochemical Society, 244th ECS Meeting in Gothenburg (Sweden)*, **2023**, Poster presentation.

E. Zemlyanushin, S. Dsoke, Impact of Polyvinylidene fluoride on the stability of Aluminum-Batteries and the use of Polyvinylidene chloride as an appropriate alternative, The 14th International Conference on Advanced Lithium Batteries for Automobile Applications (abaa14), *Ho Chi Minh City* (*Vietnam*), **2023**, Poster presentation.

E. Zemlyanushin, S. Dsoke, Impact of Polyvinylidene fluoride on the stability of Aluminum-Batteries and the use of Polyvinylidene chloride as an appropriate alternative, *1st European Symposium on Polymer Electrolytes for Battery Applications (ESPE2023), Karlsruhe (Germany)*, **2023**, Poster presentation.

E. Zemlyanushin, S. Dsoke, Impact of Polyvinylidene fluoride on the stability of Aluminum-Batteries and the use of Polyvinylidene chloride as an appropriate alternative, *International Society of Electrochemistry (ISE), 74th Annual Meeting in Lyon (France)*, **2023**, Poster presentation.

E. Zemlyanushin, F. Rahide, S. Dsoke, The Crucial and Underestimated Role of the Current Collector, *NordBatt 2022, Gothenburg (Sweden)*, **2022**, Poster presentation.

E. Zemlyanushin, F. Rahide, S. Dsoke, The Crucuial and Underestimated Role of the Current Collector, *European Materials Research Society (EMRS), Fall Meeting in Warsaw (Poland)*, **2022**, Poster presentation including One-minute oral poster presentation and Three minutes thesis competition with the title: Interphase and Interface in Aluminum-Batteries, Oral presentation.

E. Zemlyanushin, F. Rahide, S. Dsoke, The Crucial and Underestimated Role of the Current Collector, *International Society of Electrochemistry (ISE), Regional Meeting in Prague (Czech Republic)*, **2022**, Poster presentation and Three minutes oral poster presentation.

F. Rahide, **E. Zemlyanushin**, S. Dsoke, On the way towards non-corrosive electrolytes for aluminum batteries, *International Society of Electrochemistry (ISE), 72nd Annual Meeting in Jeju Island, Korea*, **2021**, Poster presentation.

9. Contributions of co-authors and other researchers

The results of **Chapter 4** are extracted from the scientific publications "Dissolution of molybdenum current collector as Crucial and Undesired process in aluminum batteries" [38] and "Roadmap on multivalent batteries; ADIBs – current collector and anode corrosion issues" [24].

The planning, organization and conception of the presented work of all included experiments were done by Eugen Zemlyanushin and supervised by Prof. Helmut Ehrenberg from the Karlsruhe Institute of Technology (KIT) and Prof. Sonia Dsoke from KIT and Albert-Ludwigs University, Freiburg, both in Germany. Furthermore, Eugen Zemlyanushin has written and revised the manuscripts. The synthesis of cubic Co_3O_4 positive electrode material was done by Eugen Zemlyanushin. Electrode preparation, cell assembly, electrochemical testing (CV, GCPL) and analysis of the obtained data were conducted by Eugen Zemlyanushin. ^{1}H- and ^{13}C-NMR measurements were done by Julian Brückel from the Institute for Organic Chemistry (IOC-KIT) and interpreted by Eugen Zemlyanushin. Magnetometry measurements and interpretation were done by Dr. Björn Schwarz (KIT). UV-VIS and XRD devices at the KIT were operated by Eugen Zemlyanushin, who did the evaluation too. The magnetron sputtering of TiN on SS and Cu-foil was performed by Dr. Michael Stüber and apl. Prof. Sven Ulrich, both from KIT. Yichen Fu has done XRD measurements of the TiN@Cu material from the Chiba University (CU) in Japan and recorded SEM images as well. Bettina Hunzinger (KIT) contributed with additional SEM images. ICP-OES analysis was done by Dr. Thomas Bergfeldt (KIT). XPS spectra were measured together with Dipl.-Ing. Vanessa Trouillet (KIT) and Dr. Christian Njel (KIT), both helped with the interpretation of the obtained data. All results were discussed with Prof. Sonia Dsoke and Dr. Björn Schwarz, whereby both helped to finalize the manuscripts.

Shown results of **Chapter 5** are extracted from the scientific publication "Side-Reactions of Polyvinylidene Fluoride and Polyvinylidene Chloride Binders with Aluminum Chloride-Based Ionic Liquid Electrolyte in Rechargeable Aluminum-Batteries" [34].

The planning, organization and conception of the presented work and all included experiments were done by Eugen Zemlyanushin and supervised by Prof. Helmut Ehrenberg, Prof. Sonia Dsoke and Prof. Tetsuya Tsuda from Chiba University (CU) in Japan. The manuscript has been prepared and revised by Eugen Zemlyanushin. Electrode preparation, cell assembly and electrochemical testing (CV, GCPL) were conducted by Eugen Zemlyanushin and supported by Annika Lykka Müller (KIT). Evaluation and interpretation of obtained data was done by Eugen Zemlyanushin. IR and UV-VIS measurements were performed and

analysed by Eugen Zemlyanushin. Felix Bauer (KIT) measured all Raman samples and Eugen Zemlyanushin did the analysis. ^{1}H-^{13}C- and ^{19}F-NMR spectra were recorded by Julian Brückel (IOC-KIT) and evaluated by Eugen Zemlyanushin. Top and cross-section SEM images were recorded by Dr. Valeriu Mereacre (KIT). All results were discussed with Prof. Tetsuya Tsuda and Prof. Sonia Dsoke, whereby both helped to finalize the manuscript.

In **Chapter 6** shows results that are currently under preparation for publication with the working title "Impact of Gallium chloride Additive in Lewis acidic ionic liquid electrolytes for Rechargeable Aluminum-Batteries" and in addition extracted from the review paper "Navigating the Challenges of Rechargeable Aluminum Battery Research: Material Instabilities, Technical Hurdles, and Future Directions" [21] and "Roadmap on multivalent batteries; ADIBs – current collector and anode corrosion issues" [24].

The planning, organization and conception of the presented work and all included experiments were done by Eugen Zemlyanushin and were supervised by Prof. Helmut Ehrenberg, Prof. Sonia and Prof. Tetsuya Tsuda. Currently, Eugen Zemlyanushin is finalizing the manuscript. Electrode preparation, cell assembly and electrochemical testing (OCV, CV, GCPL, rate capability tests) were conducted by Eugen Zemlyanushin and supported by Kevin Xia (KIT). SEM and EDX images were recorded by Yichen Fu (CU), Bettina Hunzinger (KIT) and Bijian Deng (KIT) and interpreted by Eugen Zemlyanushin. XRD was measured by Yichen Fu and evaluated by Eugen Zemlyanushin. Synchrotron XRD patterns were recorded by Dr. Angelina Sarapulova and Dr. Jiali Peng. The interpretation of the obtained synchrotron XRD data was done by Dr. Angelina Sarapulova and Eugen Zemlyanushin, in equal contribution. EXAFS measurements were done by Dr. Angelina Sarapulova, Dr. Jiali Peng, Dr. Sylvio Indris and Eugen Zemlyanushin. The simulation, fitting and interpretation of EXAFS data was done by Dr. Angelina Sarapulova. All results were discussed with Dr. Angelina Sarapulova, Prof. Sonia Dsoke and Prof. Tetsuya Tsuda, while all three co-authors are helping to finalize the manuscript.

10. References

1. Höök, M. & Tang, X. Depletion of fossil fuels and anthropogenic climate change-A review. *Energy Policy* **52**, 797–809 (2013).
2. Battaglia, V. *et al.* Empowering Energy Communities through Geothermal Systems. *Energies* **17**, 1–23 (2024).
3. Serag, S., Echchelh, A. & Morrone, B. Hydroelectric and Hydrogen Storage Systems for Electric Energy Produced from Renewable Energy Sources. *Energy Eng.* **0**, 1–10 (2024).
4. Kealy, T. The need for energy storage on renewable energy generator outputs to lessen the Geeth effect, i.e. short-term variations mainly associated with wind turbine active power output. *Energy Reports* **9**, 1018–1028 (2023).
5. Moheimani, N. R. & Parlevliet, D. Sustainable solar energy conversion to chemical and electrical energy. *Renew. Sustain. Energy Rev.* **27**, 494–504 (2013).
6. Leisegang, T. *et al.* The aluminum-ion battery: A sustainable and seminal concept? *Front. Chem.* **7**, 1–21 (2019).
7. Zhang, Y., Liu, S., Ji, Y., Ma, J. & Yu, H. Emerging Nonaqueous Aluminum-Ion Batteries: Challenges, Status, and Perspectives. *Adv. Mater.* **30**, 1706310 (2018).
8. Shahzad, K. & Cheema, I. I. Aluminum batteries: Unique potentials and addressing key challenges in energy storage. *J. Energy Storage* **90**, 111795 (2024).
9. Meng, J., Zhu, L., Haruna, A. B., Ozoemena, K. I. & Pang, Q. Charge storage mechanisms of cathode materials in rechargeable aluminum batteries. *Sci. China Chem.* **64**, 1888–1907 (2021).
10. Long, Y. *et al.* Suppressing Al dendrite growth towards a long-life Al-metal battery. *Energy Storage Mater.* **34**, 194–202 (2021).
11. Reed, L. D. & Menke, E. The Roles of V 2 O 5 and Stainless Steel in Rechargeable Al–Ion Batteries . *J. Electrochem. Soc.* **160**, A915–A917 (2013).
12. Wang, S. *et al.* Aluminum Chloride-Graphite Batteries with Flexible Current Collectors Prepared from Earth-Abundant Elements. *Adv. Sci.* **5**, 1–6 (2018).
13. Kravchyk, K. V. & Kovalenko, M. V. Aluminum electrolytes for Al dual-ion batteries. *Commun. Chem.* **3**, 1–9 (2020).
14. Smajic, J., Alazmi, A. & Costa, P. M. F. J. The Role of the Binder/Solvent Pair on the Electrochemical Performance of Aluminium Batteries. *MRS Adv.* **4**, 807–812 (2019).
15. Restriction of per- and polyfluoroalkyl substances (PFAS) by the European Chemical Agency (ECHA), Bundesanstalt für Arbeitsschutz und Arbeitsmedizin.
16. Jiao, H. *et al.* Liquid gallium as long cycle life and recyclable negative electrode for Al-ion batteries. *Chem. Eng. J.* **391**, 123594 (2020).
17. Li, J. *et al.* Electrodeposition of a dendrite-free 3D Al anode for improving cycling of an aluminum–graphite battery. *Carbon Energy* **4**, 155–169 (2022).
18. S. Geetha & Trivedi, D. C. Properties and applications of chloroaluminate as room temperature ionic liquid. *Bull. Electrochem.* **19**, 37–48 (2003).
19. Hua, Y., Zhang, T., Chen, X. & Li, T. Purification of Anhydrous Aluminum Chloride Based on the ‘Aluminum-Containing Resources Chlorination-Electrolysis’ Process. *SSRN* 1–22 (2025).
20. Poetz, S. *et al.* Evaluation of decomposition products of EMImCl·1.5AlCl3 during

aluminium electrodeposition with different analytical methods. *RSC Adv.* **4**, 6685–6690 (2014).

21. Fuentes-Mendoza, E. *et al.* Navigating the Challenges of Rechargeable Aluminum Battery Research: Material Instabilities, Technical Hurdles, and Future Directions. *ChemElectroChem.* (2025).

22. Razaz, G. *et al.* Impact of Surface Microstructure and Properties of Aluminum Electrodes on the Plating/Stripping Behavior of Aluminum-Based Batteries Using Imidazolium-Based Electrolyte. *ACS Appl. Mater. Interfaces* **16**, 65725-65736. (2024).

23. Wang, J. E., Gilbert, A., Harper, J. B. & Kim, D. J. Understanding the Failure Mechanism of Rechargeable Aluminum Batteries: Metal Anode Perspective Through X-Ray Tomography. *Adv. Energy Sustain. Res.* **3**, 1–8 (2022).

24. Palacin, M. R. *et al.* Roadmap on multivalent batteries. *JPhys Energy* **6**, 031501 (2024).

25. Wen, X. *et al.* Materials Compatibility in Rechargeable Aluminum Batteries: Chemical and Electrochemical Properties between Vanadium Pentoxide and Chloroaluminate Ionic Liquids. *Chem. Mater.* **31**, 7238–7247 (2019).

26. Wang, Q., Zheng, D., He, L. & Ren, X. Cooperative Effect in a Graphite Intercalation Compound: Enhanced Mobility of AlCl4 in the Graphite Cathode of Aluminum-Ion Batteries. *Phys. Rev. Appl.* **12**, 044060 (2019).

27. Wu, F., Yang, H., Bai, Y. & Wu, C. Paving the Path toward Reliable Cathode Materials for Aluminum-Ion Batteries. *Adv. Mater.* **31**, 1–18 (2019).

28. Gao, Y., Zhu, C., Chen, Z. Z. & Lu, G. Understanding Ultrafast Rechargeable Aluminum-Ion Battery from First-Principles. *J. Phys. Chem. C* **121**, 7131–7138 (2017).

29. Zou, F. & Manthiram, A. A Review of the Design of Advanced Binders for High-Performance Batteries. *Adv. Energy Mater.* **10**, 1–28 (2020).

30. Wang, H. *et al.* Binder-free V2O5 cathode for greener rechargeable aluminum battery. *ACS Appl. Mater. Interfaces* **7**, 80–84 (2015).

31. Yu, J. *et al.* Pencil-Drawing Graphite Nanosheets: A Simple and Effective Cathode for High-Capacity Aluminum Batteries. *Small Methods* **6**, 1–7 (2022).

32. Yang, Z. *et al.* Aqueous Binders Compatible with Ionic Liquid Electrolyte for High-Performance Aluminum-Ion Batteries. *Chem. - A Eur. J.* **29**, e202203546 (2023).

33. Yu, Z., Xie, Y., Wang, W., Hong, J. & Ge, J. Selection principles of polymeric frameworks for solid-state electrolytes of non-aqueous aluminum-ion batteries. *Front. Chem.* **11**, 1–9 (2023).

34. Zemlyanushin, E., Müller, A. L., Tsuda, T. & Dsoke, S. Interaction of Polyvinylidene fluoride (PVdF) and Polyvinylidene chloride (PVdC) with Aluminum chloride / 1-Ethyl-3-methylimidazole chloride (EMImCl) ionic liquid electrolyte in Rechargeable Aluminum-Batteries (RABs). *J. Electrochem. Soc.* **171**, 110507 (2024).

35. Chen, L. L. *et al.* Nonmetal Current Collectors: The Key Component for High-Energy-Density Aluminum Batteries. *Adv. Mater.* **32**, 1–8 (2020).

36. Zhu, P. *et al.* A review of current collectors for lithium-ion batteries. *J. Power Sources* **485**, 229321 (2021).

37. Ghani, F., An, K. & Lee, D. A Review on Design Parameters for the Full-Cell Lithium-Ion Batteries. *Batteries* **10**, 340 (2024).

38. Zemlyanushin, E., Schwarz, B. & Dsoke, S. Dissolution of molybdenum current collector as Crucial and Undesired process in aluminum batteries. *J. Power Sources* **633**,

2–11 (2025).

39. Arora, P. & Zhang, Z. Battery separators. *Chem. Rev.* **104**, 4419–4462 (2004).

40. Entwistle, J., Ge, R., Pardikar, K., Smith, R. & Cumming, D. Carbon binder domain networks and electrical conductivity in lithium-ion battery electrodes: A critical review. *Renew. Sustain. Energy Rev.* **166**, 112624 (2022).

41. Spahr, M. E., Goers, D., Leone, A., Stallone, S. & Grivei, E. Development of carbon conductive additives for advanced lithium ion batteries. *J. Power Sources* **196**, 3404–3413 (2011).

42. AJ Torriero, A. Understanding the Differences between a Quasi-Reference Electrode and a Reference Electrode. *Med. Anal. Chem. Int. J.* **3**, 2–4 (2019).

43. Snook, G. A., Best, A. S., Pandolfo, A. G. & Hollenkamp, A. F. Evaluation of a Ag{divides}Ag+ reference electrode for use in room temperature ionic liquids. *Electrochem. commun.* **8**, 1405–1411 (2006).

44. Sarbapalli, D., Mishra, A. & Rodríguez-López, J. Pt/Polypyrrole Quasi-References Revisited: Robustness and Application in Electrochemical Energy Storage Research. *Anal. Chem.* **93**, 14048–14052 (2021).

45. Maniam, K. K. & Paul, S. A review on the electrodeposition of aluminum and aluminum alloys in ionic liquids. *Coatings* **11**, 1–36 (2021).

46. Talari, M. *et al.* Exploring the possibility of aluminum plating/stripping from a non-corrosive Al(OTf)3-based electrolyte. *Batter. Supercaps* **8**, e202400317 (2024).

47. Jiao, H., Wang, J., Tu, J., Lei, H. & Jiao, S. Aluminum-Ion Asymmetric Supercapacitor Incorporating Carbon Nanotubes and an Ionic Liquid Electrolyte: Al/AlCl3-[EMIm]Cl/CNTs. *Energy Technol.* **4**, 1112–1118 (2016).

48. Leung, O. M., Schoetz, T., Prodromakis, T. & Ponce de Leon, C. Review—Progress in Electrolytes for Rechargeable Aluminium Batteries. *J. Electrochem. Soc.* **168**, 056509 (2021).

49. Schoetz, T., de Leon, C. P., Ueda, M. & Bund, A. Perspective—State of the Art of Rechargeable Aluminum Batteries in Non-Aqueous Systems. *J. Electrochem. Soc.* **164**, A3499–A3502 (2017).

50. Han, X. *et al.* Electrolytes for rechargeable aluminum batteries. *Prog. Mater. Sci.* **128**, 100960 (2022).

51. Yang, H. *et al.* The Rechargeable Aluminum Battery: Opportunities and Challenges. *Angew. Chemie - Int. Ed.* **58**, 11978–11996 (2019).

52. Elia, G. A. *et al.* An Overview and Future Perspectives of Aluminum Batteries. *Adv. Mater.* **28**, 7564–7579 (2016).

53. Marsh, K. N., Boxall, J. A. & Lichtenthaler, R. Room temperature ionic liquids and their mixtures - A review. *Fluid Phase Equilib.* **219**, 93–98 (2004).

54. Hapiot, P. & Lagrost, C. Electrochemical reactivity in room-temperature ionic liquids. *Chem. Rev.* **108**, 2238–2264 (2008).

55. Welton, T. Room-Temperature Ionic Liquids. Solvents for Synthesis and Catalysis. *Chem. Rev.* **99**, 2071–2082 (1999).

56. Hallett, J. P. & Welton, T. Room-temperature ionic liquids: Solvents for synthesis and catalysis. 2. *Chem. Rev.* **111**, 3508–3576 (2011).

57. Galiński, M., Lewandowski, A. & Stepniak, I. Ionic liquids as electrolytes. *Electrochim. Acta* **51**, 5567–5580 (2006).

58. Faegh, E., Ng, B., Hayman, D. & Mustain, W. E. Practical assessment of the performance of aluminium battery technologies. *Nat. Energy* **6**, 21–29 (2021).

59. Ferrara, C., Dall'Asta, V., Berbenni, V., Quartarone, E. & Mustarelli, P. Physicochemical Characterization of AlCl3-1-Ethyl-3-methylimidazolium Chloride Ionic Liquid Electrolytes for Aluminum Rechargeable Batteries. *J. Phys. Chem. C* **121**, 26607–26614 (2017).

60. Tsuda, T., Stafford, G. R. & Hussey, C. L. Review—Electrochemical Surface Finishing and Energy Storage Technology with Room-Temperature Haloaluminate Ionic Liquids and Mixtures. *J. Electrochem. Soc.* **164**, H5007–H5017 (2017).

61. Shi, M., Jiang, J. & Zhao, H. Electrodeposition of Aluminum in the 1-Ethyl-3-Methylimidazolium Tetrachloroaluminate Ionic Liquid. *Electrochem* **2**, 185–196 (2021).

62. Böttcher, R., Ispas, A. & Bund, A. Anodic dissolution of aluminum and anodic passivation in [EMIm]Cl-based ionic liquids. *Electrochem. commun.* **115**, 106720 (2020).

63. Hussey, C. L. Room temperature haloaluminate ionic liquids. Novel solvents for transition metal solution chemistry. *Pure Appl. Chem.* **60**, 1763–1772 (1988).

64. Beyersdorff, T. *et al. Ionic Liquids in Synthesis*. (Wiley-VCH, Weinheim, 2007).

65. Kosar, M., Taimoory, S. M., Diesenhaus, O. & Trant, J. F. Improvement of electrolytes for aluminum ion batteries: A molecular dynamics study. *J. Chem. Phys.* **159**, 144503 (2023).

66. Zhang, L., Ma, Q., Wang, G. & Liu, Z. A low cost electrolyte of AlCl3/AcAm ionic liquid analogs for high-performance aluminum ion batteries. *J. Electroanal. Chem.* **888**, 115176 (2021).

67. Wu, J. *et al.* Deep Eutectic Solvents for Boosting Electrochemical Energy Storage and Conversion: A Review and Perspective. *Adv. Funct. Mater.* **31**, 1–25 (2021).

68. Smith, E. L., Abbott, A. P. & Ryder, K. S. Deep Eutectic Solvents (DESs) and Their Applications. *Chem. Rev.* **114**, 11060–11082 (2014).

69. Malik, M., Ng, K. L. & Azimi, G. Physicochemical characterization of AlCl3-urea ionic liquid analogs: Speciation, conductivity, and electrochemical stability. *Electrochim. Acta* **354**, 136708 (2020).

70. Angell, M. *et al.* High Coulombic efficiency aluminum-ion battery using an AlCl3-urea ionic liquid analog electrolyte. *Proc. Natl. Acad. Sci. U. S. A.* **114**, 834–839 (2017).

71. Elia, G. A., Hoeppner, K. & Hahn, R. Comparison of Chloroaluminate Melts for Aluminum Graphite Dual-Ion Battery Application. *Batter. Supercaps* **4**, 368–373 (2021).

72. Holleck, G. L., Giner, J., Soc, J. E., Ag, K. & Bovet, A. L. The Aluminum Electrode in AlCl 3 - Alkali - Halide Melts. *Electrochem. Soc.* **119**, 1161–1166 (1972).

73. Song, Y. *et al.* A long-life rechargeable Al ion battery based on molten salts. *J. Mater. Chem. A* **5**, 1282–1291 (2017).

74. Tu, J. *et al.* The Effects of Anions Behaviors on Electrochemical Properties of Al/Graphite Rechargeable Aluminum-Ion Battery via Molten AlCl 3 -NaCl Liquid Electrolyte . *J. Electrochem. Soc.* **164**, A3292–A3302 (2017).

75. Chen, C. Y., Tsuda, T., Kuwabata, S. & Hussey, C. L. Rechargeable aluminum batteries utilizing a chloroaluminate inorganic ionic liquid electrolyte. *Chem. Commun.* **54**, 4164–4167 (2018).

76. Xu, J. H., Turney, D. E., Jadhav, A. L. & Messinger, R. J. Effects of Graphite Structure

and Ion Transport on the Electrochemical Properties of Rechargeable Aluminum-Graphite Batteries. *ACS Appl. Energy Mater.* **2**, 7799–7810 (2019).

77. Eftekhari, A. & Corrochano, P. Electrochemical energy storage by aluminum as a lightweight and cheap anode/charge carrier. *Sustain. Energy Fuels* **1**, 1246–1264 (2017).

78. Lin, M. C. *et al.* An ultrafast rechargeable aluminium-ion battery. *Nature* **520**, 325–328 (2015).

79. Chen, H. *et al.* A Defect-Free Principle for Advanced Graphene Cathode of Aluminum-Ion Battery. *Adv. Mater.* **29**, 1605958 (2017).

80. Kim, J., Raj, M. R. & Lee, G. High-Defect-Density Graphite for Superior-Performance Aluminum-Ion Batteries with Ultra-Fast Charging and Stable Long Life. *Nano-Micro Lett.* **13**, 171 (2021).

81. Lu, H. *et al.* Two-Dimensional Covalent Organic Frameworks with Enhanced Aluminum Storage Properties. *ChemSusChem* **13**, 3447–3454 (2020).

82. Agiorgousis, M. L., Sun, Y. Y. & Zhang, S. The Role of Ionic Liquid Electrolyte in an Aluminum-Graphite Electrochemical Cell. *ACS Energy Lett.* **2**, 689–693 (2017).

83. Wang, S. *et al.* High Specific Capacitance Based on N-Doped Microporous Carbon in [EMIm]Al x Cl y Ionic Liquid Electrolyte . *J. Electrochem. Soc.* **164**, A3319–A3325 (2017).

84. Zhang, C. *et al.* Amorphous Carbon-Derived Nanosheet-Bricked Porous Graphite as High-Performance Cathode for Aluminum-Ion Batteries. *ACS Appl. Mater. Interfaces* **10**, 26510–26516 (2018).

85. Xu, J. *et al.* A multiscale study on the effect of compression on lithium-ion battery separators. *J. Energy Storage* **54**, 105255 (2022).

86. Yu, X., Wang, B., Gong, D., Xu, Z. & Lu, B. Graphene Nanoribbons on Highly Porous 3D Graphene for High-Capacity and Ultrastable Al-Ion Batteries. *Adv. Mater.* **29**, 1604118 (2017).

87. Zhang, L., Chen, L., Luo, H., Zhou, X. & Liu, Z. Large-Sized Few-Layer Graphene Enables an Ultrafast and Long-Life Aluminum-Ion Battery. *Adv. Energy Mater.* **7**, 1–7 (2017).

88. Ravel, B. & Newville, M. ATHENA, ARTEMIS, HEPHAESTUS: Data analysis for X-ray absorption spectroscopy using IFEFFIT. *J. Synchrotron Radiat.* **12**, 537–541 (2005).

89. Zabinsky, S. I., Rehr, J. J., Ankudinov, A., Albers, R. C. & Eller, M. J. Multiple-scattering calculations of x-ray-absorption spectra. *Phys. Rev. B* **52**, 2995–3009 (1995).

90. Rodríguez-Carvajal, J. Recent advances in magnetic structure determination by neutron powder diffraction. *Phys. B Phys. Condens. Matter* **192**, 55–69 (1993).

91. Zhu, N., Zhang, K., Wu, F., Bai, Y. & Wu, C. Review Article Ionic Liquid-Based Electrolytes for Aluminum / Magnesium / Sodium-Ion Batteries. *Energy Mater. Adv.* **2021**, 1–29 (2021).

92. Tu, J. *et al.* Nonaqueous Rechargeable Aluminum Batteries: Progresses, Challenges, and Perspectives. *Chem. Rev.* **121**, 4903–4961 (2021).

93. Castaño, D. M.-T. Development and Optimization of Rechargeable Batteries based on Aluminium. (2020).

94. Cohn, G., Ma, L. & Archer, L. A. A novel non-aqueous aluminum sulfur battery. *J. Power Sources* **283**, 416–422 (2015).

95. Jiao, H., Wang, J., Tu, J., Lei, H. & Jiao, S. Aluminum-Ion Asymmetric Supercapacitor

Incorporating Carbon Nanotubes and an Ionic Liquid Electrolyte: Al/AlCl3-[EMIm]Cl/CNTs. *Energy Technol.* **4**, 1112–1118 (2016).

96. Jayaprakash, N., Das, S. K. & Archer, L. A. The rechargeable aluminum-ion battery. *Chem. Commun.* **47**, 12610–12612 (2011).

97. Li, Z. *et al.* Mountain-like nanostructured 3D Ni3S2 on Ni foam for rechargeable aluminum battery and its theoretical analysis on charge/discharge mechanism. *J. Alloys Compd.* **798**, 500–506 (2019).

98. Zhang, X. *et al.* Rechargeable ultrahigh-capacity tellurium-aluminum batteries. *Energy Environ. Sci.* **12**, 1918–1927 (2019).

99. He, S. *et al.* Rechargeable Al-Chalcogen Batteries: Status, Challenges, and Perspectives. *Adv. Energy Mater.* **11**, 1–14 (2021).

100. Lyu, Y. *et al.* An Overview on the Advances of LiCoO2 Cathodes for Lithium-Ion Batteries. *Adv. Energy Mater.* **11**, 1–29 (2021).

101. Jiao, H., Tian, D., Li, S., Fu, C. & Jiao, S. A Rechargeable Al-Te Battery. *ACS Appl. Energy Mater.* **1**, 4924–4930 (2018).

102. Gu, S. *et al.* Confirming reversible Al3+ storage mechanism through intercalation of Al3+ into V2O5 nanowires in a rechargeable aluminum battery. *Energy Storage Mater.* **6**, 9–17 (2017).

103. Oh, Y., Lee, G. & Tak, Y. Stability of Metallic Current Collectors in Acidic Ionic Liquid for Rechargeable Aluminum-Ion Batteries. *ChemElectroChem* **5**, 3348–3352 (2018).

104. Yu, Z., Tu, J., Wang, C. & Jiao, S. A Rechargeable Al/Graphite Battery Based on AlCl 3 /1-butyl-3-methylimidazolium Chloride Ionic Liquid Electrolyte. *ChemistrySelect* **4**, 3018–3024 (2019).

105. Liu, J., Li, Z., Huo, X. & Li, J. Nanosphere-rod-like Co3O4 as high performance cathode material for aluminium ion batteries. *J. Power Sources* **422**, 49–56 (2019).

106. Yasaka, Y., Wakai, C., Matubayasi, N. & Nakahara, M. Water as an in situ NMR indicator for impurity acids in ionic liquids. *Anal. Chem.* **81**, 400–407 (2009).

107. Farnum, D. G. Charge Density-NMR Chemical Shift Correlations in Organic Ions. *Adv. Phys. Org. Chem.* **11**, 123–175 (1975).

108. Tan, S. *et al.* Complexation of heavy metal cations with imidazolium ionic liquids lowers their reduction energy: implications for electrochemical separations. *Green Chem.* **26**, 1566–1576 (2023).

109. Schwarz, B. & Fu, Q. Magnetic Single-Ion Anisotropy and Curie-Weiss Behaviour of Mg3V4(PO4)6. *Eur. J. Inorg. Chem.* **27**, e202400162 (2024).

110. Misirlioğlu, Z. & Aksüt, A. Corrosion of molybdenum in aqueous media. *Corrosion* **58**, 899–903 (2002).

111. Fritscher, J., Hrobárik, P. & Kaupp, M. Computational studies of electron paramagnetic resonance parameters for paramagnetic molybdenum complexes. 1. Method validation on small and medium-sized systems. *J. Phys. Chem. B* **111**, 4616–4629 (2007).

112. Estager, J., Holbrey, J. D. & Swadźba-Kwaśny, M. Halometallate ionic liquids-revisited. *Chem. Soc. Rev.* **43**, 847–886 (2014).

113. Lang, H., Zhang, J., Kang, Y., Chen, S. & Zhang, S. Effects of lithium bis(oxalato)borate on electrochemical stability of [Emim][Al2Cl7] ionic liquid for aluminum electrolysis. *Ionics (Kiel).* **23**, 959–966 (2017).

114. Hartmann, H. & Schmidt, H. J. Über Absorptionsspektren komplexer Verbindungen des

dreiwertigen Molybdäns. *Zeitschrift fur Phys. Chemie* **11**, 234–250 (1957).

115. Scheffler, T. B., Hussey, C. L., Seddon, K. R., Kear, C. M. & Armitage, P. D. Molybdenum Chloro Complexes in Room-Temperature Chloroaluminate Ionic Liquids: Stabilization of [MoCl6]2- and [MoCl6]3-. *Inorg. Chem.* **22**, 2099–2100 (1983).

116. Sun, H. *et al.* A new aluminium-ion battery with high voltage, high safety and low cost. *Chem. Commun.* **51**, 11892–11895 (2015).

117. Shi, J., Zhang, J. & Guo, J. Avoiding Pitfalls in Rechargeable Aluminum Batteries Research. *ACS Energy Lett.* **4**, 2124–2129 (2019).

118. Diem, A. M., Fenk, B., Bill, J. & Burghard, Z. Binder-free v2o5 cathode for high energy density rechargeable aluminum-ion batteries. *Nanomaterials* **10**, 1–15 (2020).

119. Reed, L. UNIVERSITY OF CALIFORNIA, MERCED Aluminum ion batteries: Electrolytes and Cathodes. (2015).

120. Choi, J. G. & Thompson, L. T. XPS study of as-prepared and reduced molybdenum oxides. *Appl. Surf. Sci.* **93**, 143–149 (1996).

121. Couch, D. E. & Brenner, A. Preparation of trichloride and tetrachloride of molybdenum. *J. Res. Natl. Bur. Stand. Sect. A Phys. Chem.* **63A**, 185 (1959).

122. Ulrich, S. *et al.* Correlation between constitution, properties and machining performance of TiN/ZrN multilayers. *Surf. Coatings Technol.* **188**–**189**, 331–337 (2004).

123. Cupak, C. *et al.* Sputter yields of rough surfaces: Importance of the mean surface inclination angle from nano- to microscopic rough regimes. *Appl. Surf. Sci.* **570**, 151204 (2021).

124. Wang, Z., Che, J. & Ye, C. Application of ferric chloride both as oxidant and complexant to enhance the dissolution of metallic copper. *Hydrometallurgy* **105**, 69–74 (2010).

125. Wu, Q., Han, M. H., Xin, H. L., Dong, B. Q. & Jin, Y. Studies on IR spectroscopy and quantum chemical calculation of chloroaluminate ionic liquids acidity. *Guang Pu Xue Yu Guang Pu Fen Xi/Spectroscopy Spectr. Anal.* **28**, 282–284 (2008).

126. Reidy, L., Wang, C. & Hussey, C. L. Anodic Dissolution of Copper in the Acidic and Basic Aluminum Chloride 1-Ethyl-3-methylimidazolium Chloride Ionic Liquid. *J. Electrochem. Soc.* **168**, 046503 (2021).

127. Wang, Y. C., Lee, T. C., Lin, J. Y., Chang, J. K. & Tseng, C. M. Corrosion properties of metals in dicyanamide-based ionic liquids. *Corros. Sci.* **78**, 81–88 (2014).

128. Argimbaev, K., Ligotsky, D. & Loginov, E. Current state of production and consumption of rhenium abroad. *E3S Web Conf.* **258**, 12012 (2021).

129. Wu, B., Dekanovsky, L., Vlastimil, M., Wei, S. & Sofer, Z. Electrochemical Behavior of Rechargeable Al-Ni Battery Systems in Concentrated [EMIm]Cl-AlCl3Electrolyte. *ACS Appl. Energy Mater.* **5**, 6797–6804 (2022).

130. Zhang, X. *et al.* Green water-based binders for LiFePO4/C cathodes in Li-ion batteries: A comparative study. *New J. Chem.* **45**, 9846–9855 (2021).

131. Saxena, P. & Shukla, P. A comprehensive review on fundamental properties and applications of poly(vinylidene fluoride) (PVDF). *Adv. Compos. Hybrid Mater.* **4**, 8–26 (2021).

132. Kosar, W. P. & Morris, S. A functional fluoropolymer powder coating for chemical process applications. *J. Coatings Technol. Res.* **4**, 51–58 (2007).

133. Zhou, W. *et al.* Enhancement of piezoelectricity in polymer PVDF based on molecular chain structure. *J. Mater. Sci. Mater. Electron.* **32**, 28708–28717 (2021).

134. Uemura, Y. *et al.* Graphene Nanoplatelet Composite Cathode for a Chloroaluminate Ionic Liquid-Based Aluminum Secondary Battery. *ACS Appl. Energy Mater.* **1**, 2269–2274 (2018).

135. Chen, L. L. *et al.* Stable wide-temperature and low volume expansion Al batteries: Integrating few-layer graphene with multifunctional cobalt boride nanocluster as positive electrode. *Nano Res.* **13**, 419–429 (2020).

136. Ma, D. *et al.* Current Progress and Future Perspectives of Electrolytes for Rechargeable Aluminum-Ion Batteries. *Energy Environ. Mater.* **6**, 1–18 (2023).

137. Correia, D. M. *et al.* Ionic Liquid Cation Size-Dependent Electromechanical Response of Ionic Liquid/Poly(vinylidene fluoride)-Based Soft Actuators. *J. Phys. Chem. C* **123**, 12744–12752 (2019).

138. Correia, D. M. *et al.* Crystallization Monitoring of Semicrystalline Poly(vinylidene fluoride)/1-Ethyl-3-methylimidazolium Hexafluorophosphate [Emim][PF6] Ionic Liquid Blends. *Cryst. Growth Des.* **21**, 4406–4416 (2021).

139. Wasserscheid, P. & Keim, W. Ionic Liquids - New 'Solutions' for Transition Metal Catalysis. *Angew. Chem. Int. Ed* **39**, 3772–3789 (2000).

140. Jiao, H., Wang, C., Tu, J., Tian, D. & Jiao, S. A rechargeable Al-ion battery: Al/molten AlCl3-urea/graphite. *Chem. Commun.* **53**, 2331–2334 (2017).

141. Abood, H. M. A., Abbott, A. P., Ballantyne, A. D. & Ryder, K. S. Do all ionic liquids need organic cations? Characterisation of [AlCl2·nAmide]+ AlCl4- and comparison with imidazolium based systems. *Chem. Commun.* **47**, 3523–3525 (2011).

142. Bormashenko, Y., Pogreb, R., Stanevsky, O. & Bormashenko, E. Vibrational spectrum of PVDF and its interpretation. *Polym. Test.* **23**, 791–796 (2004).

143. Kasbi, S. F., Jafari, S. H., Khonakdar, H. A., Goodarzi, V. & Torabi, A. β-Polymorph enhancement in poly(vinylidene fluoride) by blending with polyamide 6 and barium titanate nanoparticles. *J. Appl. Polym. Sci.* **137**, 1–9 (2020).

144. Pendleton, P., Vincent, B. & Hair, M. L. Dehydrochlorination of monodisperse poly(vinylidene chloride) latex. *J. Colloid Interface Sci.* **80**, 512–527 (1981).

145. Streletskiy, O. A. *et al.* The Field-Effect Transistor Based on a Polyyne–Polyene Structure Obtained via PVDC Dehydrochlorination. *J. Compos. Sci.* **7**, 264 (2023).

146. Singh Samra, K., Thakur, S. & Singh, L. Photoluminescent and thermal behavior of 120 MeV silicon and 84 MeV oxygen ion irradiated PVDC. *J. Lumin.* **131**, 686–694 (2011).

147. Peltzer, M. A. & Simoneau, C. *Report of an Inter-Laboratory Comparison from the European Reference Laboratory for Food Contact Materials : ILC 002 2013 : Identification of Polymeric Materials*. (2013).

148. Xiao, X., Zeng, Z. & Xiao, S. Behavior and products of mechano-chemical dechlorination of polyvinyl chloride and poly (vinylidene chloride). *J. Hazard. Mater.* **151**, 118–124 (2008).

149. Daems, N. *et al.* High-performance membranes with full pH-stability. *RSC Adv.* **8**, 8813–8827 (2018).

150. Sharma, J., Totee, C., Kulshrestha, V. & Ameduri, B. Spectroscopic evidence and mechanistic insights on dehydrofluorination of PVDF in alkaline medium. *Eur. Polym. J.* **201**, 112580 (2023).

151. Thulasiraman, S. *et al.* Effects of Ionic Liquid, 1-Ethyl-3-methylimidazolium Chloride ([EMIM]Cl), on the Material and Electrical Characteristics of Asphaltene Thin Films. *Materials (Basel).* **15**, 2818 (2022).

152. Liu, F., Zhong, X., Xu, J., Wang, Z. & Shi, Z. Facile synthesis and characterization of 1-ethyl-3-methylimidazolium fluoride ionic liquid. *J. Phys. Conf. Ser.* **1347**, 012109 (2019).

153. Ahmed, M. M. *et al.* Revisiting the polyvinylidene fluoride heterogeneous alkaline reaction mechanism in propan-2-ol: An additional hydrogenation step. *Eur. Polym. J.* **156**, 110605 (2021).

154. Alenazi, B., Alsalme, A., Alshammari, S. G., Khan, R. A. & Siddiqui, M. R. H. Ionothermal Synthesis of Metal Oxide-Based Nanocatalysts and Their Application towards the Oxidative Desulfurization of Dibenzothiophene. *J. Chem.* **2020**, 1–11 (2020).

155. Yoshioka, T., Kameda, T., Imai, S., Noritsune, M. & Okuwaki, A. Dechlorination of poly(vinylidene chloride) in NaOH/ethylene glycol as a function of NaOH concentration, temperature, and solvent. *Polym. Degrad. Stab.* **93**, 1979–1984 (2008).

156. Korshak, V. V. *et al.* Formation of β-carbyne by dehydrohalogenation. *Die Makromol. Chemie, Rapid Commun.* **9**, 135–140 (1988).

157. Zhu, W. *et al.* The role of water on dehydrofluorination in PVDF/K2CO3 percolative composites. *Mater. Today Commun.* **32**, 103884 (2022).

158. Streletskiy, O. A. *et al.* Low-Threshold Field Emission Cathode Based on Heat-Treated Dehydrofluorinated Polyvinylidene Fluoride. *J. Exp. Theor. Phys.* **135**, 844–852 (2022).

159. Zhivulin, V. E. *et al.* Synthesis and properties of polyvinylidene fluoride high-temperature treatment products. *Phys. Solid State* **59**, 408–412 (2017).

160. Casari, C. S. *et al.* Chemical and thermal stability of carbyne-like structures in cluster-assembled carbon films. *Phys. Rev. B - Condens. Matter Mater. Phys.* **69**, 1–7 (2004).

161. Streletskiy, O. A. *et al.* Resistive Gas Sensors Based on Porous Sp-Containing Films Obtained by Dehydrohalogenation of PVDC and PVDC-PVC Copolymer. *C-Journal Carbon Res.* **9**, 82 (2023).

162. Kryazhev, Y. G. *et al.* Evolution of the structures and sorption properties of dehydrochlorinated chloropolymers during their thermal conversions. *Prot. Met. Phys. Chem. Surfaces* **45**, 398–402 (2009).

163. Niino, H. & Yabe, A. Formation of conjugated polyene and polyyne structure by KrF excimer laser-induced dehydrochlorination on polyvinylidenechloride film. *J. Polym. Sci. Part A Polym. Chem.* **36**, 2483–2487 (1998).

164. Bodor, A., Tóth, I., Bányai, I., Szabó, Z. & Hefter, G. T. 19F NMR study of the equilibria and dynamics of the Al3+/F- system. *Inorg. Chem.* **39**, 2530–2537 (2000).

165. Ji, Q., Zhou, L. & Nasr-El-Din, H. Acidizing Sandstone Reservoirs With Aluminum-Based Retarded Mud Acid. *SPE J.* **21**, 1050–1060 (2016).

166. Cadiau, A. *et al.* Evolution of guanazolium fluoroaluminates within the composition-space diagram and with the temperature. *Cryst. Growth Des.* **10**, 5159–5168 (2010).

167. Yang, H. *et al.* An Aluminum–Sulfur Battery with a Fast Kinetic Response. *Angew. Chemie* **130**, 1916–1920 (2018).

168. Liu, S. *et al.* An advanced high energy-efficiency rechargeable aluminum-selenium battery. *Nano Energy* **66**, 104159 (2019).

169. Lyu, X., Wang, W., Sun, Y., Zhao, Q. & Qiu, T. Ionic Liquids Catalyzed Friedel–Crafts Alkylation of Substituted Benzenes with CCl 4 Toward Trichloromethylarenes. *Catal. Letters* **149**, 665–671 (2019).

170. Khokarale, S. G. *et al.* Poly (Vinylidene Difluoride) Polymer in 1-Ethyl-3-methylimidazolium Acetate and Acetic Acid Containing Solvents: Tunable and Recoverable Solvent Media to Induce Crystalline Phase Transition and Porosity. *Sustain. Chem.* **3**, 455–474 (2022).

171. Elia, G. A. *et al.* Insights into the reversibility of aluminum graphite batteries. *J. Mater. Chem. A* **5**, 9682–9690 (2017).

172. Mukundan, C., Eckert, M. & Drillet, J. F. Impact of Aluminium Electrode Potential during Charging on Aluminium-Ion Battery Performance with TEA-AlCl3 Electrolyte. *Batter. Supercaps* **6**, e202300042 (2023).

173. Huang, M. C. *et al.* Influence of High Loading on the Performance of Natural Graphite-Based Al Secondary Batteries. *Energies* **11**, 12–16 (2018).

174. Appiah, W. A., Stockham, M. P. & Garcia Lastra, J. M. Towards Understanding the Variation of Electrode Design Parameters on the Electrochemical Performance of Aluminum Graphite Batteries: An Experimental and Simulation Study. *Batter. Supercaps* **6**, e202300258 (2023).

175. Wei, J., Chen, W., Chen, D. & Yang, K. An amorphous carbon-graphite composite cathode for long cycle life rechargeable aluminum ion batteries. *J. Mater. Sci. Technol.* **34**, 983–989 (2018).

176. Matsumoto, K., Takagi, K. & Hagiwara, R. Electrochemical Synthesis of Graphite-Tetrafluoroaluminate Intercalation Compounds. *J. Electrochem. Soc.* **159**, H876–H880 (2012).

177. Matsumoto, K., Minori, D., Takagi, K. & Hagiwara, R. Expansion of tetrachloroaluminate-graphite intercalation compound by reaction with anhydrous hydrogen fluoride. *Carbon N. Y.* **67**, 434–439 (2014).

178. Wang, G., Yu, M. & Feng, X. Carbon materials for ion-intercalation involved rechargeable battery technologies. *Chem. Soc. Rev.* **50**, 2388–2443 (2021).

179. Krahl, T. & Kemnitz, E. The very strong solid Lewis acids aluminium chlorofluoride (ACF) and bromofluoride (ABF)-Synthesis, structure, and Lewis acidity. *J. Fluor. Chem.* **127**, 663–678 (2006).

180. Zhou, J., Yu, X., Zhou, J. & Lu, B. Polyimide/metal-organic framework hybrid for high performance Al - Organic battery. *Energy Storage Mater.* **31**, 58–63 (2020).

181. Textor, M. & Amstutz, M. Surface analysis of thin films and interfaces in commercial aluminium products. *Anal. Chim. Acta* **297**, 15–26 (1994).

182. Jiang, M. *et al.* Challenges and Strategies of Low-Cost Aluminum Anodes for High-Performance Al-Based Batteries. *Adv. Mater.* **34**, 1–27 (2022).

183. Choi, S., Go, H., Lee, G. & Tak, Y. Electrochemical properties of an aluminum anode in an ionic liquid electrolyte for rechargeable aluminum-ion batteries. *Phys. Chem. Chem. Phys.* **19**, 8653–8656 (2017).

184. Senel, E. & Nisancioglu, K. Role of dealloying on the electrochemical behaviour of aluminium alloyed with trace amounts of gallium. *Corros. Sci.* **85**, 436–444 (2014).

185. Das, S. K., Mahapatra, S. & Lahan, H. Aluminium-ion batteries: developments and challenges. *J. Mater. Chem. A* **5**, 6347–6367 (2017).

186. Chen, H. *et al.* Oxide Film Efficiently Suppresses Dendrite Growth in Aluminum-Ion Battery. *ACS Appl. Mater. Interfaces* **9**, 22628–22634 (2017).

187. Yang, H., Wu, F., Bai, Y. & Wu, C. Toward better electrode/electrolyte interfaces in the ionic-liquid-based rechargeable aluminum batteries. *J. Energy Chem.* **45**, 98–102 (2020).

188. Pyagai, I. N., Pasechnik, L. A., Yatsenko, A. S., Skachkov, V. M. & Yatsenko, S. P. Recovery of sludge from alumina production. *Russ. J. Appl. Chem.* **85**, 1649–1653 (2012).

189. Wang, H., Leung, D. Y. C. & Leung, M. K. H. Energy analysis of hydrogen and electricity production from aluminum-based processes. *Appl. Energy* **90**, 100–105 (2012).

190. Wang, J. *et al.* Stable Interface between a NaCl-AlCl3 Melt and a Liquid Ga Negative Electrode for a Long-Life Stationary Al-Ion Energy Storage Battery. *ACS Appl. Mater. Interfaces* **12**, 15063–15070 (2020).

191. Li, Q., Jensen, J. O. & Bjerrum, N. J. *CHEMISTRY, ELECTROCHEMISTRY, AND ELECTROCHEMICAL APPLICATIONS: Aluminum*. *Encyclopedia of Electrochemical Power Sources* (Elsevier, 2009).

192. Neburchilov, V. & Zhang, J. *Metal-Air and Metal-Sulfur Batteries: Fundamentals and Applications*. (CRC Press, 2016).

193. Murray, J. L. The Al-Ga (Aluminum-Gallium) System. *Bull. Alloy Phase Diagr.* **4**, 183–190 (1983).

194. Langford, N. J. & Ferner, R. . Toxicity of mercury. *J. Hum. Hypertens.* **13**, 651–656 (1999).

195. Yu, Y., Wang, S., Wang, X., Wang, Q. & Liu, J. Semisolid Al-Ga composites fabricated at room temperature for hydrogen generation. *RSC Adv.* **10**, 10076–10081 (2020).

196. Breslin, C. B. & Carroll, W. M. The electrochemical behabiour of aluminium activated by gallium in aqueous electrolytes. *Corros. Sci.* **33**, 1735–1746 (1992).

197. Reboul, M. C., Gimenez, P. & Ramaeu, J. J. PROPOSED ACTIVATION MECHANISM FOR Al ANODES. *Corrosion* **40**, 366–371 (1984).

198. Fan, Y. *et al.* A Self-Healing Amalgam Interface in Metal Batteries. *Adv. Mater.* **32**, 1–7 (2020).

199. Conder, J. & Villevieille, C. How reliable is the Na metal as a counter electrode in Na-ion half cells? *Chem. Commun.* **55**, 1275–1278 (2019).

200. Zhang, X., Wang, A., Liu, X. & Luo, J. Dendrites in Lithium Metal Anodes: Suppression, Regulation, and Elimination. *Acc. Chem. Res.* **52**, 3223–3232 (2019).

201. Carpenter, M. K. & Verbrugge, M. W. Electrochemical Codeposition of Gallium and Arsenic from a Room Temperature Chlorogallate Melt. *J. Electrochem. Soc.* **137**, 123–129 (1990).

202. Bakkar, A. & Neubert, V. Electrodeposition of photovoltaic thin films from ionic liquids in ambient atmosphere: Gallium from a chloroaluminate ionic liquid. *J. Electroanal. Chem.* **856**, 113656 (2020).

203. Peng, Y., Shinde, P. S. & Reddy, R. G. Diffusion coefficient and nucleation density studies on electrochemical deposition of aluminum from chloroaluminate ionic liquid electrolytes. *J. Electroanal. Chem.* **895**, 115363 (2021).

204. Schubert, T. *Electrodeposition from Ionic Liquids*. (Wiley-VCH, Weinheim, 2017).

205. Wu, Q. *et al.* Study on electrodeposition of gallium-selenium binary alloy films from Deep Eutectic Solvent. *J. Electroanal. Chem.* **967**, 118472 (2024).

206. Lee, D., Kim, C. L. & Sohn, Y. Formation and growth of intermetallic compounds during reactions between liquid gallium and solid nickel. *Materials (Basel).* **14**, 1–11 (2021).

207. De Long, H. C. Electrodeposition of Aluminum-Manganese Alloys from Room-

Temperature Chloroaluminate Molten Salts. *ECS Proc. Vol.* **1998**–**11**, 40–54 (1998).

208. Razaz, G. *et al.* Aluminum Alloy Anode with Various Iron Content Influencing the Performance of Aluminum-Ion Batteries. *Materials (Basel).* **16**, 933 (2023).

209. Li, M. *et al.* Electrodeposition of aluminum from AlCl3/acetamide eutectic solvent. *Electrochim. Acta* **180**, 811–814 (2015).

210. Xu, J. H., Turney, D. E., Jadhav, A. L. & Messinger, R. J. Effects of Graphite Structure and Ion Transport on the Electrochemical Properties of Rechargeable Aluminum-Graphite Batteries. *ACS Appl. Energy Mater.* 7799–7810 (2019).

211. Yan, C. *et al.* Architecting a Stable High-Energy Aqueous Al-Ion Battery. *J. Am. Chem. Soc.* **142**, 15295–15304 (2020).

212. Buckingham, R., Asset, T. & Atanassov, P. Aluminum-air batteries : A review of alloys , electrolytes and design. *J. Power Sources* **498**, 229762 (2021).

213. Kobayashi, M. *et al.* Preferential penetration path of gallium into grain boundary in practical aluminium alloy. *Philos. Mag.* **86**, 4351–4366 (2006).

214. Spindlberger, A., Ciatto, G., Adhikari, R., Yadav, A. K. & Bonanni, A. Local structure and ordering of Al atoms in AlxGa1−xN epilayers. *Appl. Phys. Lett.* **123**, 232101 (2023).

215. Li, C. *et al.* Self-Discharge Behavior of Graphitic Cathodes for Rechargeable Aluminum Batteries. *Adv. Funct. Mater.* **33**, 1–11 (2023).

216. Zhao, J. *et al.* Reversible Insertion of [AlCl4]− Superhalides in Graphite. *ChemSusChem* **17**, 1–7 (2024).

217. Amberchan, G. *et al.* Aluminum Nanoparticles from a Ga-Al Composite for Water Splitting and Hydrogen Generation. *ACS Appl. Nano Mater.* **5**, 2636–2643 (2022).

218. Zoellner, B. *et al.* Activating the Growth of High Surface Area Alumina Using a Liquid Galinstan Alloy. *ACS Omega* **3**, 16409–16415 (2018).

219. Shentu, J. *et al.* Characteristics for Gallium-Based Liquid Alloys of Low Melting Temperature. *Metals (Basel).* **13**, 615 (2023).

11. Appendix

The cell lattice parameters and the phase purity of synthesized Co_3O_4 were investigated by X-ray diffraction (XRD). The XRD patterns of Co_3O_4 are shown in **Figure S1**. All diffraction peaks can be indexed to a pure cubic phase Co_3O_4 without any impurities. The corresponding space group is Fd-3m with the lattice parameters a=b=c=8.086 Å and an angle of α=β=γ=90° (ICSD no = 36256).

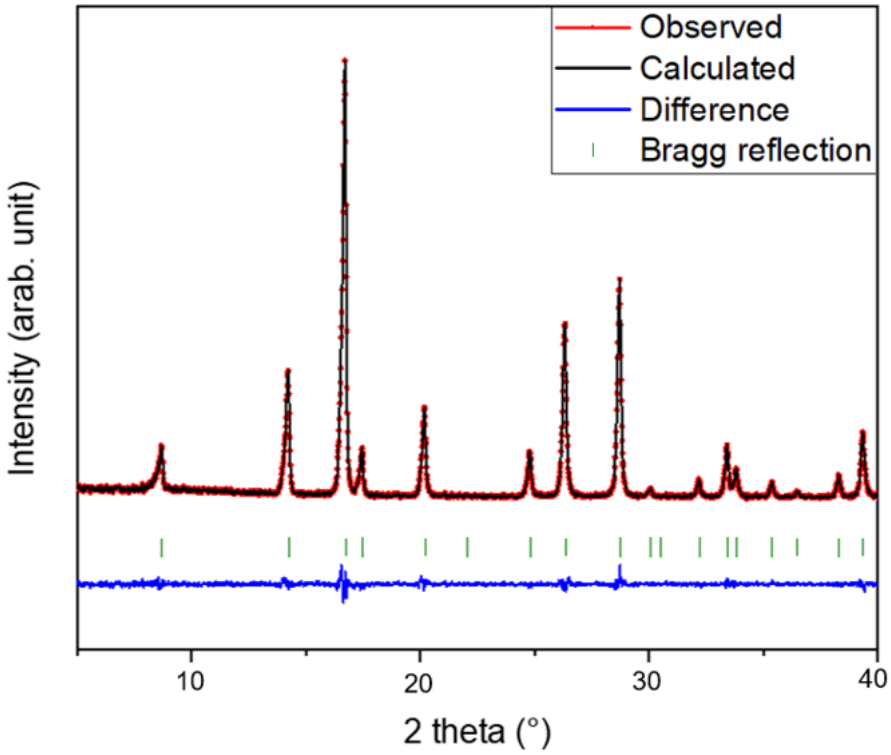

Figure S1 X-ray diffraction (XRD) pattern of synthesized cubic Co_3O_4.

Table S1 Volume (Å^3), Bragg R-factor and Rf-factor of the Rietveld refinement of cubic Co_3O_4.

Sample	V [Å^3]	Bragg R-factor	Rf-factor
Co_3O_4	528.665(2)	2.12	1.65

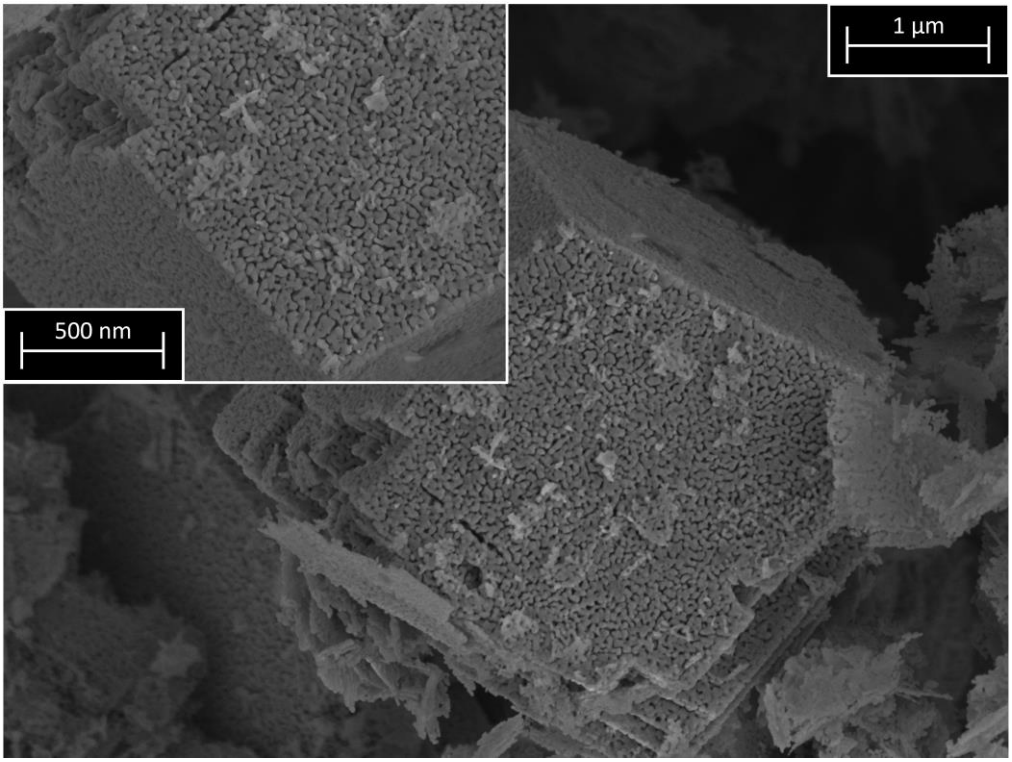

Figure S2 Scanning electron microscope (SEM) image of synthesized cubic Co_3O_4 at a zoom of 1 µm and 500 nm.

Table S2 Fourier-transform infrared (FT-IR) bands of pristine PVdF and PVdC.

PVdF: Band (cm^{-1})	Group and vibrational mode	PVdC: Band (cm^{-1})	Group and vibrational mode
487	-CF_2; wagging	428	C-Cl_2; stretching
532	-CF_2; bending	530	-C-C-; skeletal deformation mode
612	-CF_2; bending and skeletal bending	612	-CCl_2; stretching
760	-CF_2; bending and skeletal bending	962	-C-C-; skeletal stretching causing in plane CH_2 rocking
795	-CH_2; rocking	1066	-C-C-; skeletal stretching mode resulting from influence of Cl atoms
840	-CH_2; rocking	1211	-C-C-; skeletal stretching mode
870	-CH; wagging	1240	-C-C-; skeletal stretching mode
973	-CH; out-of-plane deformation	1326	-CH_2; wagging
1065	-C-C-; symmetric stretching, -CF_2; wagging, -CH_2; wagging	1350	-CH_2; wagging
1148	-CF_2; symmetric stretching	1423	-CH_2; bending
1179	-CF_2; symmetric stretching, -CH_2; twisting	1741 (impurity)	-C=O; stretching

1205	-CF_2; asymmetric stretching, -CH_2; wagging	1777 (impurity)	-C=O; stretching
1278	-CF_2; out-of-plane deformation, - C- C-; symmetric stretching, -C-C-C-; scissoring	2818	-CH; stretching
1383	-CH; deformation	2851	-CH; stretching
1400	-CH_2; wagging, -C-C-; symmetric stretching	2917	-CH_2; antisymmetric stretching mode
2925	-CH_2; symmetric stretching	2971	-CH_2; symmetric stretching mode
2985	-CH_2; asymmetric stretching	-	-
3026	-CH_2; asymmetric stretching	-	-

Table S3 Overlapping bands of EMImCl in comparison to PVdF and PVdC.

Band (cm^{-1}) of EMImCl	Group and vibrational mode
General: 3700-2700	-CH_2; asymmetric and symmetric stretching
3400	broad formation of quaternary amine salt with chloride
3155-3100	-CH; asymmetric and symmetric stretching of EMImCl ring
2985	-CH; aliphatic asymmetric stretching of alkyl groups
General: 1800-1400	-C=C-; polymer backbone
1639	-C=C-; asymmetric ring stretching
1569	-C=C-; asymmetric ring stretching
1457	-C=C-; asymmetric aliphatic ring bending
1400	-C=C-; aliphatic bending
1383	-C=C-; symmetric aliphatic ring bending, aliphatic wagging
1205	-CH; aromatic twisting
1179	-CN; twisting
1148	-CH; aromatic twisting
760	-CH; aliphatic twisting

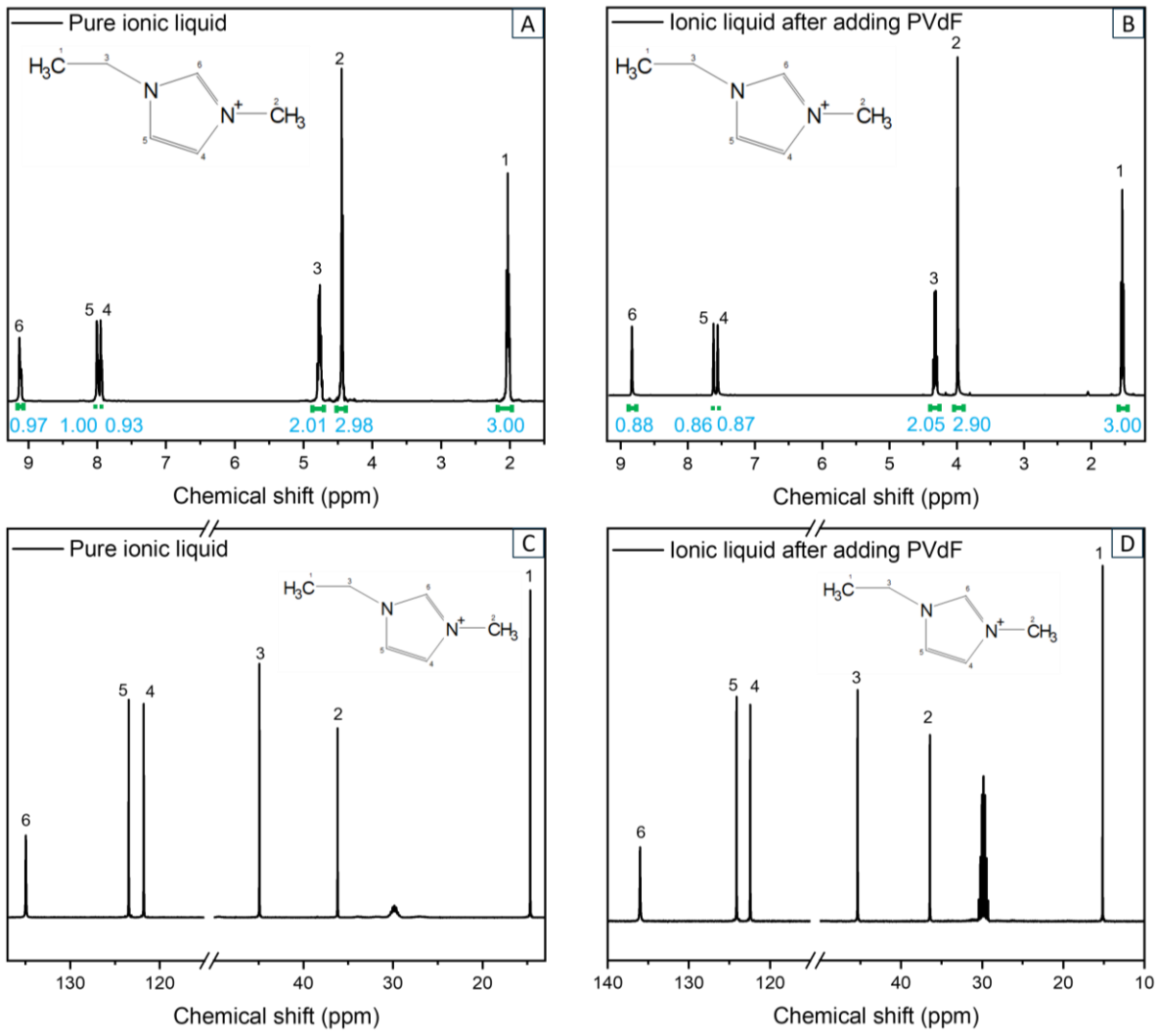

Figure S3 ^{1}H-NMR (A) and ^{13}C-NMR (C) of pristine $AlCl_3$:EMImCl ionic liquid electrolyte and ^{1}H-NMR (B) and ^{13}C-NMR (D) of soaked "black" electrolyte, respectively.

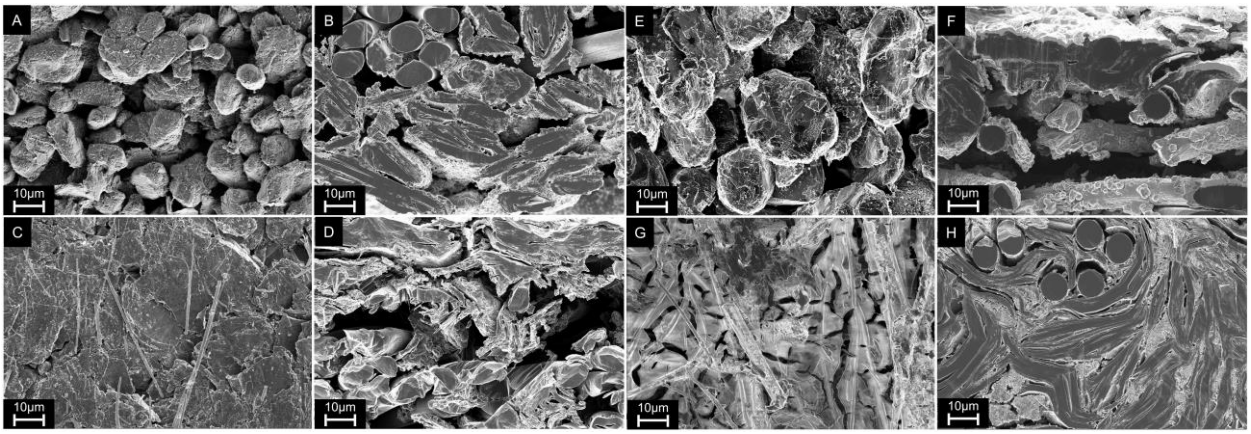

Figure S4 Scanning electron microscope (SEM) images of p-PVdF (A, top view; B, cross-section) and cycled PVdF (C, top view; D, cross-section); p-PVdC (E, top view; F, cross-section) and cycled PVdC (G, top view; H, cross-section).

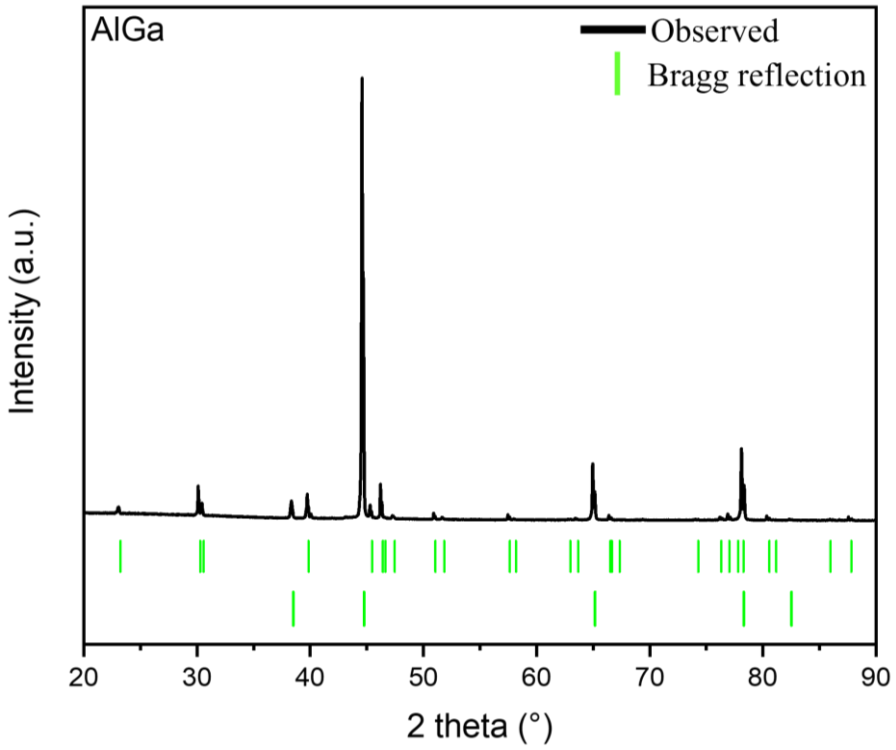

Figure S5 X-ray diffraction (XRD) pattern of AlGa alloy formed by mere contact of Al-foil with $GaCl_3$ (0.1 M) containing $AlCl_3$:EMImCl ionic liquid electrolytes after 24 hours. The measurement has been done at Chiba University (Japan), using a Cu Kα 1.5406 Å X-ray source. The upper Bragg reflections can be assigned to α-Ga (JCPDS No. 00-006-0503) and the lower Bragg reflections belong to cubic Al (JCPDS No. 89-2837).

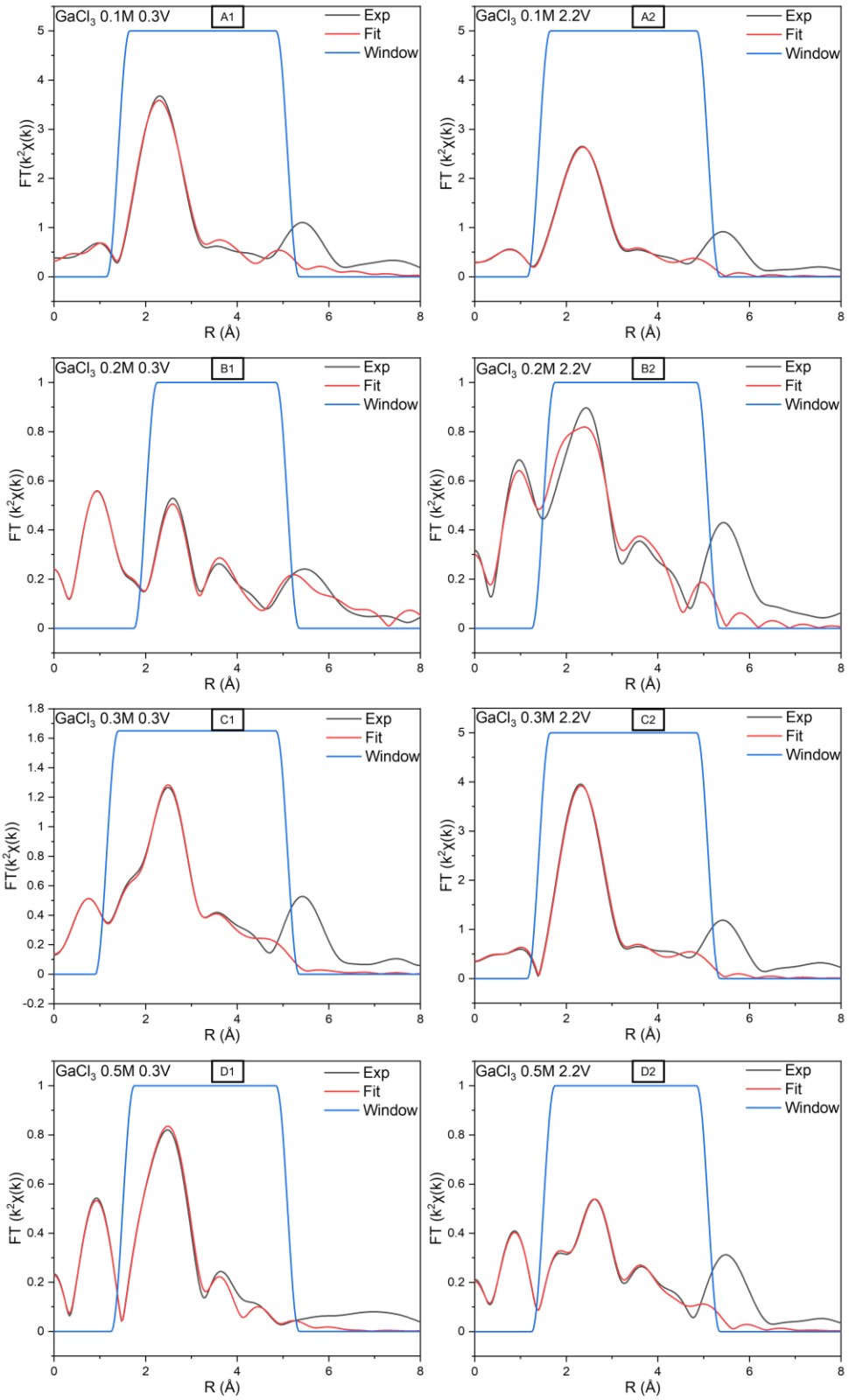

Figure S6 Magnitude of the Fourier-transforms of the $k^2\chi(k)$ *vs.* distance (*R*) EXAFS spectra with experimental data (black) and fitted curve (red) of AlGa negative electrodes cycled in (**A1-A2**) 0.1 M; (**B1-B2**) 0.2 M; (**C1-C2**) 0.3 M and (**D1-D2**) 0.5 M $GaCl_3$-containing ionic liquid electrolytes.